Alma Mater Studiorum · University of Bologna

School of Science
Department of Physics and Astronomy
Master Degree in Physics

Bell inequalities with top quark pairs with the ATLAS Detector at the LHC

Supervisor
Prof. Maximiliano Sioli

Co–supervisor
Prof. Fabio Maltoni

Submitted by
Claudio Severi

Academic Year 2020/2021

Abstract

This work is a feasibility study for the detection of a violation of Bell inequalities using top spin correlations at the LHC. Bell inequalities are a model-independent test of non-classical behavior; in a theory where observables are local and have definite values ahead of measurement, one can put an upper bound on how correlated two systems can be. A violation of such limits (i.e. of Bell inequalities) has been observed in many quantum systems, such as pairs of entangled photons. We are able to cast Bell inequalities in a form that is usable for $t\bar{t}$ pairs produced in hadron colliders, in what would be the first test at the TeV scale. In particular, top quark pairs emitted perpendicular to the proton beam at $v \sim c$ have their spin maximally entangled as a consequence of conservation of angular momentum. In this regime our proposed experimental setup is identical (in spirit) to the one used in quantum optics. We simulate the measurement starting from event generation at parton level, fully showering hard partons, simulating the response of the ATLAS detector, reconstructing the event kinematics, and unfolding the distributions obtained. We show that a violation of Bell inequalities is expected. The statistical significance for a violation is small if considering the upcoming LHC Run 3 luminosity, but should grow after the next High-Luminosity run, reaching, conservatively, $\sim 90\%$ CL.

Contents

Introduction

If a pair of particles is created and then separated, the two–particle wavefunction retains a non–separable character. A measurement on the first particle, whose outcome is undetermined prior to experiment, in some cases predicts with complete certainty the outcome of a measurement on the second particle, even if the two experiments happen at spacelike separation.

This (apparent) tension between quantum mechanics and special relativity was famously pointed out in 1935 by Einstein, Podolsky and Rosen in what is known as the EPR Paradox [1]. It was suggested that there may exist additional classical degrees of freedom, known as *hidden variables*, that would keep reality classical and local.

Whether or not the bizzarre predictions of quantum mechanics are an accurate description of reality is not a philosophical question but a matter of experiment. In 1964, Bell proved [2] classical theories obey limits about correlations between outcomes of experiments perfomed at a distance, that quantum mechanics can sometimes violate.

Several experiments have been performed over the last half–century, mostly involving the polarization of photons produced in atomic transitions. All results obtained so far appear to violate Bell Inequalities, and are interpreted as a confirmation of quantum mechanics against alternate competing theories.

Recently, the field has seen a period of rapid growth after the prospect of using hadron colliders to test Bell Inequalities has emerged. In 2020 and 2021, several papers by Afik et al [3], Fabbrichesi et al [4], and Takubo et al [5] argued the detection of entanglement and of a violation of Bell Inequalities using spin and flavor correlations is in principle possible at the LHC.

This thesis is a feasibility study for the experimental observation of entanglement and of a violation of Bell Inequalities using spin correlations in $t\bar{t}$ pairs, prompted by the upcoming start of Run 3 of the LHC. Such an experiment would be the first TeV scale test of the puzzling non–local correlations that are a core feature of quantum mechanics, and could also be reinterpreted as a novel probe for beyond-the-Standard-Model effects.

This work is organized as follows. This first Chapter is a general introduction to the EPR Paradox, entanglement in quantum mechanics, and Bell Inequalities, together with an outlook on recent EPR experiments in high energy physics. The second Chapter concerns top quark pairs produced in hadron colliders such as the LHC, studies their

kinematic properties, and establishes an experimental road to measure spin correlations using a dilepton final state. The third Chapter contains our main theoretical result, a set of observables in $pp \to t\bar{t} \to \ell^+\ell^-$ events sensitive to the presence of entanglement and to the violation of Bell Inequalities in two different regions of phase space. The fourth and fifth Chapters describe our analysis at parton level, using events generated within the Standard Model at Leading Order. In the last three Chapters we describe our complete analysis, using events generated, showered, and reconstructed inside a simulated ATLAS Detector.

Chapter 1

Entanglement and EPR

Consider two systems A and B, whose quantum states belong to Hilbert spaces $\mathcal{H}_A$ and $\mathcal{H}_B$. The space of states for the joint system $A+B$ is the tensor product $\mathcal{H}_A \otimes \mathcal{H}_B$. A state of $A+B$ is *separable* if it can be written as:

$$|\psi\rangle = |\psi_A\rangle \otimes |\psi_B\rangle \equiv |\psi_A\, \psi_B\rangle\,, \tag{1.1}$$

with $\psi_A \in \mathcal{H}_A$ and $\psi_B \in \mathcal{H}_B$. In mathematics these states are called *decomposable tensors*. If the whole system is in the separable state $|\psi_A\psi_B\rangle$, subsystem A is in state $|\psi_A\rangle$ and subsystem B is in state $|\psi_B\rangle$, with the two parts being independent.

Since not all tensors are decomposable, there are states of the whole system that can not be interpreted as having the constituents in well defined states by themselves. Consider a pair of spin 1/2 particles in a spin singlet state:

$$|\psi\rangle = \frac{|\uparrow\downarrow\rangle - |\downarrow\uparrow\rangle}{\sqrt{2}}. \tag{1.2}$$

Not much can be said of each individual particle, except that upon measurement we will find $|\uparrow\rangle$ or $|\downarrow\rangle$ randomly with 50% probability. However, comparing experimental outcomes on the first and second particle, we find perfect (negative) correlation. States like the one in (1.2) that can not be decomposed are called *entangled*.

Entanglement can not be reproduced in any way at the classical level and is a primary feature of quantum mechanics.

Entanglement in mixed states

A quantum state is *pure* if its density matrix can be written as:

$$\rho_{\text{pure}} = |\psi\rangle\langle\psi|\,, \tag{1.3}$$

for some ψ. A state is *mixed* if it is not pure. In this case, the best we can do is to decompose its density matrix as:

$$\rho_{\text{mixed}} = \sum p_k\, |\psi_k\rangle\langle\psi_k|\,, \tag{1.4}$$

where the coefficients p_k are positive and add to one. The interpretation is that ρ_{mixed} describes a state belonging to a statistical ensemble, with probability p_k of being ψ_k.

The distinction between separable and entangled states can be generalized. The state of a system composed of two subsystems A and B is separable if its density matrix ρ can be written as:

$$\rho = \sum p_k \, \rho_1^k \otimes \rho_2^k, \tag{1.5}$$

where ρ_A^k and ρ_B^k are density matrices for A and B, and the coefficients are positive and add to one. The state is *entangled* when it is not separable.

Several different definition of entanglement are present in the literature, with somewhat different conventions being used in different fields. We go for the simplest, in which *entanglement* is synonym for *non–separability*.

One can find necessary and sufficient conditions that have to be satisfied in order for a mixed state to be entangled. One test is the Peres–Horodecki criterion [6], which is equivalent to entanglement if $\dim \mathcal{H}_A \leq 2$ and $\dim \mathcal{H}_B \leq 3$. Consider the partial transpose:

$$\rho^{T_B} = (\mathbb{1} \otimes T)\, \rho, \tag{1.6}$$

obtained by acting with the identity on A and transposing B. The criterion is: *if ρ^{T_B} has a negative eigenvalue, ρ is entangled.*

The EPR "paradox"

Einstein, Podolsky, and Rosen, proposed in 1935 [1] an argument against the quantum mechanical description of reality that can be summarized as follows:

Consider a pair of spin 1/2 particles produced in a singlet state like (1.2) that propagate into remote regions of space. Choose axis $\hat{a}, \hat{b}$ and measure the particles' spin projections along them. We find correlations:

$$p(\text{same spin}) = \sin^2\left(\theta/2\right), \tag{1.7}$$

$$p(\text{opposite spin}) = \cos^2\left(\theta/2\right) \tag{1.8}$$

with θ being the angle between $\hat{a}$ and $\hat{b}$. How can these correlations occur? Quantum mechanics predicts the experimental outcome is random and unpredictable. However, the apparatus can be set up so the two measurements are spacelike separated, so no communication at all is possible. EPR argue the two particles must have agreed on the outcomes beforehand, storing the result into additional *hidden* degrees of freedom not accounted for by quantum mechanics.

Figure 1.1: Schematic representation of an EPR experiment.

Indeed, to quote [7], *"No tribunal or detective would believe that, in any circumstance, perfect correlations could be observed in remote places without being the consequence of some common characteristics shared by both objects."*

There are two notions, that EPR took as self–evident, that have to be addressed:

1. *Locality*: there is no action at a distance, all communications occur at $v \leq c$.
2. *Realism*: given enough knowledge all observables can be predicted ahead of experiment.

These two assumptions together go by the name of *local realism*, also known as *Einstein locality*. The EPR paper actually proved:

Theorem. *Quantum mechanics is incompatible with local realism.*

Quantum mechanics seems to be valid, with correlations between events that remain well defined even at spacelike separations. *An entangled system is to be considered as a unique indivisible entity.* Since the wavefunction lives and evolves in an abstract Hilbert space which is not spacetime, there is little point in implementing locality arguments in spacetime.

This point of view seems in contradiction with special relativity, and yet it isn't: *there is no way to transmit information, or cause effects of any kind, faster than the speed of light*, no matter all the quantum behavior. Correlations, that indeed are non–local, do not carry any information *through space* and can not cause any effect.

The connection between entanglement and spacetime is very deep, and ultimately comes to the long standing problem of finding a quantum theory of gravity.

Recent developments include the ER = EPR conjecture formulated in 2013 by Madalcena and Susskind [8]. The name quotes two 1935 papers, one about wormholes by Einstein and Rosen (ER) [9], and the one about entanglement by Einstein, Podolsky, and Rosen (EPR) [1]. It is known that general relativity has solutions in which two distant black holes are connected by a wormhole. The conjecture reinterprets these solutions as connections between entangled black holes, and suggests similar bridges could also form for entangled states in general.

Another noteworthy recent contribution is the 2016 work by Cao, Carroll, and Michalakis [10], where they exhamine how a manifold and its geometry emerge just from the entanglement structure in the Hilbert space. They also argue entanglement perturbations translate into perturbations on the manifold that obey some analog of Einstein's field equations, and recover a version of the ER = EPR conjecture relating entanglement to spatial proximity.

1.1 Bell inequalities

EPR's arguments and subsequent discussions are not philosophical. Whether nature behaves quantum–mechanically and all local realistic theories are in error is a question to be decided by experiment.

If local realism holds, numerical results can be derived about correlations between measurements carried on separated systems: if two systems can only exchange information classically, we expect an upper bound on how correlated they can be. Tests are

usually cast in the form:

$$\mathcal{C}_{A,B} \leq \text{constant}, \tag{1.9}$$

where $\mathcal{C}$ measures correlation between the supposedly non-interacting subsystems A and B. These tests will be particularly interesting in regions of parameter space where they disagree with quantum mechanics.

A test of the form (1.9) was first proposed by Bell in 1964 [2], and many more have been suggested in the literature since, see also the review [7]. All such inequalities are referred to as *Bell inequalities*, and experimental tests as *EPR tests*.

Remark. Bell inequalities are completely model–independent: it does not matter if the underlying theory is classical mechanics, a modified version of quantum mechanics, such as QM with the addition of hidden variables, or some exotic counterpart. As long as local realism holds, the inequalities hold.

There is an hierarchy:

$$\begin{matrix}\text{Violation of} \\ \text{Bell inequalities}\end{matrix} \implies \text{Entanglement} \implies \text{Correlations}, \tag{1.10}$$

where the contrary implication is not true in general, not all correlations come from entanglement and not all entangled states violate a Bell inequality.

CHSH inequality

Clauser, Horne, Shimony, and Holt in 1969 [11] proposed an inequality, now known as the *CHSH inequality*, that is particularly convenient and versatile for experiments. Their argument is as follows:

We measure two quantities a, b of system A and B respectively, whose possible values are ± 1. Under local realism, the outcome of a is a function of the experimental setup and of internal variables λ_A of the first system; similarly the outcome of b will depend on the experimental setup and on some λ_B proper of the second system. Consider the expectation value:

$$\langle ab \rangle = \int a(\lambda_A)\, b(\lambda_B)\, \rho(\lambda_A, \lambda_B) d\lambda_A\, d\lambda_B, \tag{1.11}$$

where ρ is the probability distribution for the internal variables. Now also consider two different measured quantities a' and b' of A and B, giving four expectation values $\langle ab \rangle$, $\langle a'b \rangle$, $\langle ab' \rangle$, and $\langle a'b' \rangle$. Consider:

$$|\langle ab \rangle - \langle ab' \rangle| = \left| \int (ab - ab')\, \rho\, d\lambda \right| \tag{1.12}$$

$$= \left| \int ab(1 \pm a'b')\, \rho\, d\lambda - \int ab'(1 \pm a'b)\, \rho\, d\lambda \right| \tag{1.13}$$

$$\leq \int |ab|\, |1 \pm a'b'|\, \rho\, d\lambda + \int |ab'|\, |1 \pm a'b|\, \rho\, d\lambda, \tag{1.14}$$

where we used the fact that $|\int(f+g)| \leq |\int f| + |\int g|$ and $|\int f| \leq \int |f|$. Since $|ab|$ and $|ab'|$ are at most 1, we can further write:

$$|\langle ab\rangle - \langle ab'\rangle| \leq \int |1 \pm a'b'|\,\rho\,d\lambda + \int |1 \pm a'b|\,\rho\,d\lambda \tag{1.15}$$

$$\leq \int (1 \pm a'b')\,\rho\,d\lambda + \int (1 \pm a'b)\,\rho\,d\lambda \tag{1.16}$$

$$\leq 2 \pm (\langle a'b'\rangle + \langle a'b\rangle), \tag{1.17}$$

where the absolute value was dropped since the terms in brackets are not negative. By choosing the suitable sign in the $\pm$ so as to make $\pm(\langle a'b'\rangle + \langle a'b\rangle) = -\big|\langle a'b\rangle + \langle a'b'\rangle\big|$, we reach the famous *CHSH inequality*:

$$\big|\langle ab\rangle - \langle ab'\rangle\big| + \big|\langle a'b\rangle + \langle a'b'\rangle\big| \leq 2. \tag{1.18}$$

Quantum mechanics is incompatible with this constraint, with a maximum possible violation of:

$$\big|\langle ab\rangle - \langle ab'\rangle\big| + \big|\langle a'b\rangle + \langle a'b'\rangle\big| = 2\sqrt{2} > 2. \tag{1.19}$$

Note the maximum value is $2\sqrt{2}$ and not the naive expectation of 4, see [12] for a full proof.

Consider the prototype experiment of Chapter 1, where a pair of spin 1/2 particles in the singlet state is measured along different axis. Quantum mechanics predicts the expectation value of the two spins along axis $\vec{a}$ and $\vec{b}$ is given by:

$$\langle ab\rangle = \langle \frac{\uparrow\downarrow - \downarrow\uparrow}{\sqrt{2}} | (\vec{\sigma}\cdot\vec{a}) \otimes (\vec{\sigma}\cdot\vec{b}) | \frac{\uparrow\downarrow - \downarrow\uparrow}{\sqrt{2}} \rangle\,, \tag{1.20}$$

where $\vec{\sigma} = (\sigma_1, \sigma_2, \sigma_3)$ is a vector of Pauli matrices. A short calculation gives:

$$\langle ab\rangle = -\vec{a}\cdot\vec{b}. \tag{1.21}$$

In the simplest case where all axis lie in the same plane, the experimental setup is described by three angles as in Figure 1.2. One finds:

$$\langle ab\rangle = -\cos\alpha, \tag{1.22}$$

$$\langle ab'\rangle = -\cos\gamma, \tag{1.23}$$

$$\langle a'b\rangle = -\cos(\beta-\alpha), \tag{1.24}$$

$$\langle a'b'\rangle = -\cos(\gamma-\beta). \tag{1.25}$$

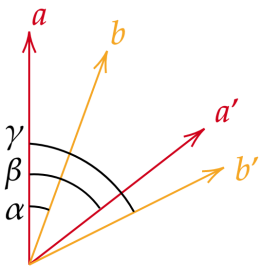

Figure 1.2: Polarizer alignment for the prototype EPR experiment.

So that the CHSH inequality (1.18) becomes:

$$\big|-\cos\alpha + \cos\gamma\big| + \big|\cos(\beta-\alpha) + \cos(\gamma-\beta)\big| \leq 2. \tag{1.26}$$

This relation is violated in large parts of parameter space, with the maximum value of $2\sqrt{2}$ reached at:

$$\alpha = \frac{\pi}{4}, \quad \beta = \frac{\pi}{2}, \quad \gamma = \frac{3\pi}{4}, \tag{1.27}$$

see also Figure 1.3 and Figure 1.4.

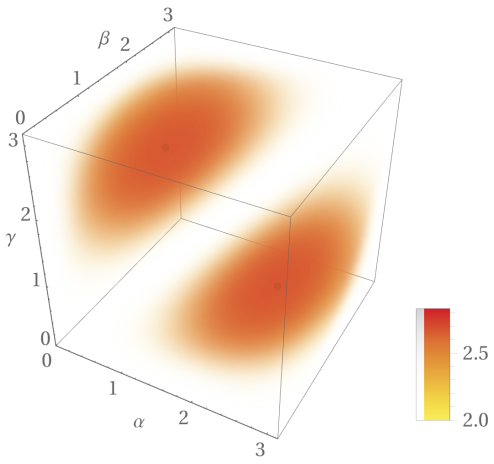

Figure 1.3: Regions of α, β, γ parameter space where the CHSH inequality (1.26) is violated. The maximally violating points $(\frac{\pi}{4}, \frac{\pi}{2}, \frac{3\pi}{4})$ and $(\frac{3\pi}{4}, \frac{\pi}{2}, \frac{\pi}{4})$ are highlighted in black.

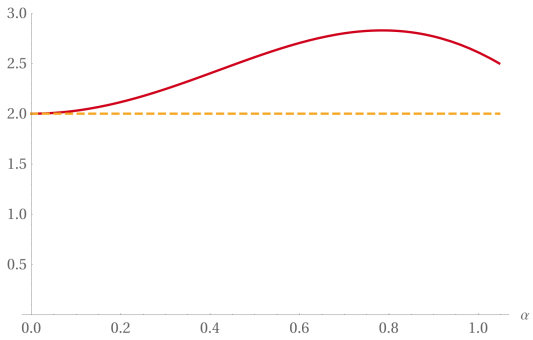

Figure 1.4: Values of the test statistic (1.26) with the symmetric choice $\alpha = \frac{\beta}{2} = \frac{\gamma}{3}$ as a function of α. The classical limit of 2 is highlighted.

Hardy's impossibilities

There are many schemes conceptually similar to Bell inequalities. One was introduced by Hardy [13], and aims to test local realism in a different way: one looks for events forbidden under local realism but allowed by quantum mechanics.

To see how this can be possible, consider a system of two particles which undergo different measurements a or a' on the first and b or b' on the second. Assume each measurement can only return values ± 1, and the following set of rules hold:

1. $a' = +1$ and $b' = +1$ can be obtained;
2. $a' = +1$ and $b = +1$ is forbidden;
3. $a = +1$ and $b' = +1$ is forbidden;
4. $a = -1$ and $b = -1$ is forbidden.

If particles "decide" in advance how to behave under measurement, these rules are contradictory. In fact, assume the particles decided as in rule 1, so under measurement of a' and b' they will return $+1$ and $+1$. By rule 2, a measurement of b will return -1. By rule 3, a measurement of a will return -1. But then, a measurement of a and b must

return -1 and -1, which is in contradiction with rule 4. Therefore, no system obeying local realism can behave like this.

However, quantum mechanics does it! Again using the example of two spin 1/2 particles, denote $|\uparrow\rangle$ and $|\downarrow\rangle$ the eigenstates of a and b, and $|\uparrow'\rangle = \cos\theta\,|\uparrow\rangle + \sin\theta\,|\downarrow\rangle$, $|\downarrow'\rangle = -\sin\theta\,|\uparrow\rangle + \cos\theta\,|\downarrow\rangle$ the eigenstates of a' and b'. Consider the state:

$$\psi = -\cos\theta\,|\uparrow\downarrow\rangle - \cos\theta\,|\downarrow\uparrow\rangle + \sin\theta\,|\uparrow\uparrow\rangle\,. \tag{1.28}$$

Rule 1 is satisfied, since $\langle\psi|\uparrow'\uparrow'\rangle = \cos^2\theta\sin\theta$ is different from zero. Rules 2, 3, and 4 are satisfied, since $|\uparrow'\uparrow\rangle$, $|\uparrow\uparrow'\rangle$, and $|\downarrow\downarrow\rangle$ are all orthogonal to ψ. No contradiction emerges. Experimental observation of a system obeying these four rules confirms its non-classical nature.

1.2 Experimental tests

Tests of Bell inequalities are theoretically straightforward. However, the kind of non-classical correlations one is looking for occur in very rare situations, and are hard to notice experimentally. In fact, there are only two places where they have been observed: experiments designed for this goal, and quantum computers, that rely precisely on these effects.

The first violation of a Bell inequality was seen in 1972 by Freedman and Clauser [14] using photons emitted by the $J = 0 \to 1 \to 0$ transition of Calcium. The experimental apparatus was conceptually similar to the one in our thought experiment in Chapter 1: a pair of entangled photons is produced by the Calcium atom, the two photons fly apart and are measured by polarizers that can be rotated at will. The coincidence rate as a function of the relative angle can be readily interpreted as a measure of non-classical behavior.

Numerous experimental tests on a variety of physical systems have been performed since, all showing consistency with quantum mechanics rather than local realism.

We mention two recent experiments. The first one in 2015 [15] used two electrons produced in a entangled spin state and then physically separated by 1.3 km. The measurement is carried in the usual way with rotating Stern-Gerlach devices. Over around 200 trials a value of 2.42 ± 0.20 was found for the CHSH inequality, violating the classical limit of 2 by about two standard deviations. Cases involving massive particles are of particular interest, since generally a massive particle displays more classical properties.

The second experiment [16], also in 2015, used entangled photons rather than electrons. Photons, being massless, are easier to handle. A violation of a Bell inequality was observed to a significance of about five standard deviations.

Loopholes

Deciding whether or not a given setup truly shows a contradiction with local realism is a controversial topic. Possible "loopholes" in experimental design might allow classical

effects to conspire in such a way that a violation to local realism is seen, even though none is actually present. Loopholes include:

- *Fair sampling*: detector efficiency in experiments is rarely close to 100%. One has to assume missed events are similar to recorded ones, and should every event be included, the result would not change by much. This loophole can be closed with better detectors, however in many cases high efficiency is physically or practically impossible, and we just have to assume there is no bias.
- *Locality*: our current understanding of particle physics suggests the entangled pairs do not exchange information after they are separated, but communication can not be ruled out definitely unless measurements are spacelike separated. To close the loophole, one has to make sure this is the case. It is also interesting to check whether the correlation changes as one moves from timelike to spacelike separated measurements.
- *Free choice*: doing experiments requires making choices. For example, one has to choose at which angle polarizers are oriented. All choices should be *free*, in the sense that they should be independent on the system that is being measured. If free choice is not ensured, one can introduce hidden classical variables that conspire with the apparatus and produce the observed correlations. For example, in our thought experiment of Chapter 1 we might have polarizer orientations set using random number generators while the particles are in flight.[1]

Since one can imagine more and more involved hidden effects, some argue [17] that a truly loophole–free experiment is philosophically impossible. However, it is tempting to say hidden variables become less and less likely the more convoluted they should be to match observations. In the end, few people actually take this seriously.

The two recent experiments with photons and electrons that were quoted above [15] and [16] claim to have closed all reasonable loopholes.

1.3 EPR at high energy

Most EPR experiments involve energies in the eV range, typically visible light photons or magnetic interactions in solids at millikelvin temperature. High energy physics is a completely different environment. Data from colliders such as the LHC can be used to look for entanglement and perform EPR–like experiments at the TeV scale.

Collider experiments present loopholes. Whether or not these loopholes can be closed in a satisfactory way is a matter of debate, see [18] and [19] for constrasting viewpoints. In any case, high energy tests are meant to provide a novel way to investigate new physics, besides producing a strict test of quantum mechanics.

[1] Then one could claim random number generators are also part of the conspiracy...

Flavor correlation

One way to perform EPR experiments in particle physics is with flavor correlations, usually strangeness or bottomness.

In $p\bar{p}$ collisions $K^0\bar{K}^0$ entangled pairs are produced, where strangeness is analogous to helicity in the two photon system. Kaon pairs are produced in a $J^{PC} = 1^{--}$ state, with wavefunction:

$$|\psi\rangle = \frac{|K^0\bar{K}^0\rangle - |\bar{K}^0K^0\rangle}{\sqrt{2}} \tag{1.29}$$

$$= \frac{|K_SK_L\rangle - |K_LK_S\rangle}{\sqrt{2}}, \tag{1.30}$$

where $K^0 = d\bar{s}$, $\bar{K}^0 = s\bar{d}$, $K_S = \frac{K^0-\bar{K}^0}{\sqrt{2}}$ and $K_L = \frac{K^0+\bar{K}^0}{\sqrt{2}}$. Long (L) and Short (S) kaon states are convenient to use since their time evolution is simple:

$$|K_S(t)\rangle = |K_S\rangle\, e^{-im_St}, \tag{1.31}$$

$$|K_L(t)\rangle = |K_L\rangle\, e^{-im_Lt}, \tag{1.32}$$

where the masses m_S and m_L differ by Δm of order $10^{-6}\,\text{eV}$. The complete time evolution for ψ is thus:

$$|\psi(t_a,t_b)\rangle = \frac{1}{\sqrt{2}}\Big(|K_SK_L\rangle\, e^{-i(m_St_a+m_Lt_b)} - |K_LK_S\rangle\, e^{-i(m_Lt_a+m_St_b)}\Big), \tag{1.33}$$

where t_a and t_b are the two kaon proper times.

The probability to find a like–strangeness state K^0K^0 or $\bar{K}^0\bar{K}^0$ at proper times t_a and t_b is given by:

$$P_{\text{same}}(t_a,t_b) = |\,\langle K^0K^0|\psi(t_a,t_b)\rangle\,|^2 + |\,\langle\bar{K}^0\bar{K}^0|\psi(t_a,t_b)\rangle\,|^2 \tag{1.34}$$

$$= \frac{1-\cos\big(\Delta m(t_a-t_b)\big)}{2}. \tag{1.35}$$

A similar calculation gives the probability to find an unlike–strangeness state, $K^0\bar{K}^0$ or $\bar{K}^0K^0$:

$$P_{\text{diff}}(t_a,t_b) = |\,\langle K^0\bar{K}^0|\psi(t_a,t_b)\rangle\,|^2 + |\,\langle\bar{K}^0K^0|\psi(t_a,t_b)\rangle\,|^2 \tag{1.36}$$

$$= \frac{1+\cos\big(\Delta m(t_a-t_b)\big)}{2}. \tag{1.37}$$

Had we included the finite kaon lifetime into our model, equations (1.35) and (1.37) would generalize to equations (3) and (4) of [20], plotted numerically in Figure 1.5.

We see the probability oscillates as a function of $t_a - t_b$ due to the cosine term, with a timescale set by Δm. There is, so to speak, a "rotating polarizer" driven by time evolution during free propagation, that stops when the kaons interact or decay. These

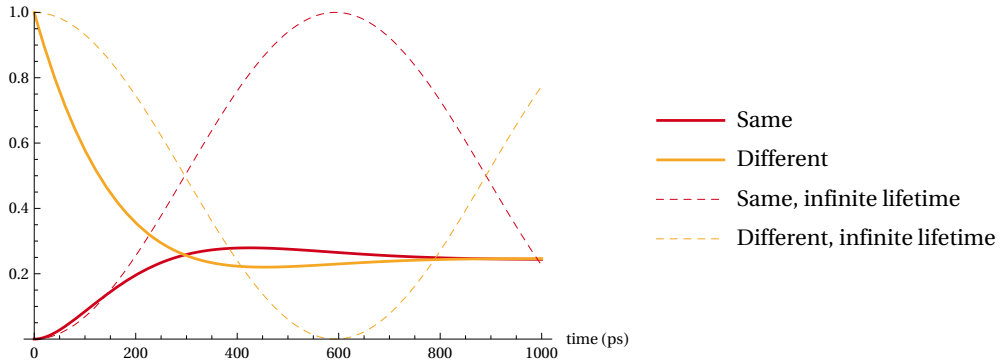

Figure 1.5: Probability to find same and different strangeness state in a $K^0\bar{K}^0$ pair as a function of t_b, with $t_a = 0$. Dashed: infinite kaon lifetime, equations (1.35) and (1.37), continuous: actual kaon lifetime, equations (3) and (4) of [20].

are EPR-type correlations, that can be measured in order to prove particles remain entangled despite their spatial separation.

The CPCLEAR Collaboration at CERN in 1998 [20] was able to perform an experiment using kaons from collisions between 200 MeV antiprotons and a fixed hydrogen target. Two different measurements are needed for an EPR test. In the first configuration, kaons were made to interact in an absorber material after a nearly equal flight time. In the second one, kaons would have a flight path difference of about 5 cm, corresponding to ~ 1.2 times their oscillation length. Results were inconsistent with a separable (that is, not entangled) wavefunction and consistent with usual quantum mechanics.

Further analysis [21] revealed many striking analogies between the kaon experiment and a simple EPR test with entangled photons of opposite helicities. For instance, strangeness mixing is seen to be equivalent to optical birefringence, and the finite kaon lifetime is formally analogous to polarization–dependent losses.

Another experimental test came in 2003 from the Belle Collaboration at KEK [22]. This test directly evaluated the CHSH inequality using $B^0\bar{B}^0$ pairs from the decay of a $\Upsilon(4S)$ meson produced in e^+e^- collisions at 10 GeV. Since entangled $B^0\,\bar{B}^0$ pairs undergo flavor oscillation similarly to $K^0\bar{K}^0$ pairs, measuring flavor at different decay times has the same effect as rotating the polarizer angle in photon experiments. Flavor tagging was performed over about 80 million pairs, with decay time difference Δt from 0 to 2.6 ps, equivalent to ~ 1.7 oscillation periods. A clear violation of the CHSH inequality was observed, with values up to $2.72 \pm 0.17_{\text{stat}} \pm 0.09_{\text{sys}}$, the classical limit being 2.

Further measurements [23] from the same Collaboration with a dataset twice as large allowed evaluation of asymmetry parameters of $B^0\,\bar{B}^0$ pairs for Δt up to 20 ps, again consistent with quantum mechanics and inconsistent with various spontaneous disentanglement models.

A feasibility study on the detection of the same effect at the LHC has been published very recently [5].

Spin correlation

A different approach is to study spin correlations. By choosing a reaction in which the final state decays electroweakly, we are automatically granted most mechanisms needed for a EPR experiment:

- It is a general feature of weak decays that spin correlation of the parents produce angular correlations in the daughters. Information about the original spin state can be extracted by measuring the final state momenta.
- The experimenters can choose which axis to use to measure angles. This freedom, it is argued [19], is equivalent to the freedom to choose the polarizer direction, and thus closes the free choice loophole.
- To rule out communication between the two particles and close the locality loophole, one can test if correlations change for spacelike vs timelike separation between the two decay events.

The idea that weak decays could be used for EPR experiments has been entertained for some time, [24, 25]. More recent analysis, such as [19] and [26], concluded observing violation of a Bell inequality using spin correlations is experimentally doable using the weak decays $\eta_c \to \Lambda\overline{\Lambda}$, $\chi_c \to \Lambda\overline{\Lambda}$, and $J/\psi \to \Lambda\overline{\Lambda}$.

It is critical to choose a channel in which a violation can be seen clearly. In fact, some processes such as $J/\psi \to \Lambda\bar{\Lambda}$ do produce an entangled pair, but due to the specific form of the matrix element are not expected to produce a visible violation. Other particles, for example the χ_c and η_c mesons, should give a better signal [19].

The fact that spin correlations are transferred to the momenta of decay products is not exclusive of electroweak decays, QCD is also sensitive to spin. Entanglement is expected [27] to be found in strong processes such as $\eta_c \to \phi\phi \to KK\bar{K}\bar{K}$ and $B \to \phi K^\star \to KK\bar{K}\pi$. In fact, the only interaction which has not (yet) been employed to generate and detect entanglement is gravity.

To conclude this Chapter, we notice that several searches for new physics have covered angular correlations, although not directly relating them to entanglement. The BELLE and LHCb Collaborations recently reported [28, 29, 30] angular analysis of various $B \to K\ell\ell$ decays where a tension between the Standard Model and observations is reported at a statistical significance of over 3σ. The tension persisted [31] when new data from Run 2 of LHC was added to the analysis in 2020, and seems to be consistently seen over different channels [32].

Chapter 2

Physics of $t\bar{t}$ pairs

The top quark is the heaviest known fundamental particle, and is a natural candidate for high energy EPR-like tests. This is due to the neat separation in timescales relevant to top physics. The top production time m_t^{-1} is smaller by two orders of magnitude than its lifetime Γ_t^{-1}. In turn this is over ten times smaller than the typical QCD hadronization timescale, $\Lambda_{\mathrm{QCD}}^{-1}$, so the top decays before it has a chance to hadronize and behaves like a free particle. Further, depolarizing effects of QCD would act to decorrelate spin on a timescale of $m_t\,\Lambda_{\mathrm{QCD}}^{-2}$, so any spin correlation present in $t\bar{t}$ pairs is passed on the decay products unobscured.

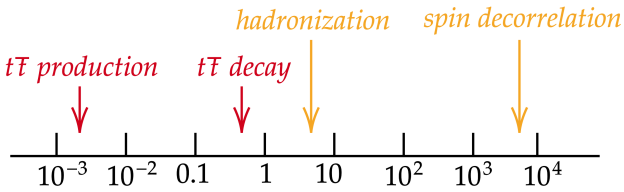

Figure 2.1: Relevant timescales for top physics, in GeV^{-1}.

In this Chapter and in following ones, we will consider events generated using MadGraph5_aMC [33] with the NN23LO1 parton density function [34]. Calculations were performed at leading order unless differently stated.

2.1 Kinematics

The kinematics of a $t\bar{t}$ pair is determined by the invariant mass $m_{t\bar{t}}$ and the production angle θ in the center of mass frame, see Figure 2.2. The parameters $m_{t\bar{t}}$ and θ can be calculated from the quark momenta p_t and $p_{\bar{t}}$,

$$m_{t\bar{t}}^2 = (p_t + p_{\bar{t}})^\mu (p_t + p_{\bar{t}})_\mu, \tag{2.1}$$

$$\cos\theta = \frac{p_{t\,z}}{|\vec{p}_t|}, \tag{2.2}$$

where the beam axis is taken to be $\hat{z}$. In most cases it is safe to identify θ and $\pi - \theta$. The transverse momentum p_T of the top quark is given in terms of $m_{t\bar{t}}$ and θ by:

$$p_T = \sin\theta \sqrt{\left(\frac{m_{t\bar{t}}}{2}\right)^2 - m_t^2}. \tag{2.3}$$

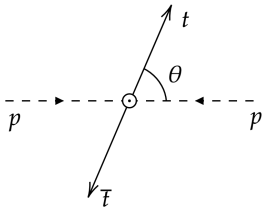

Figure 2.2: Schematic of a pp collision resulting in a $t\bar{t}$ pair, in the CM frame.

The antitop also has transverse momentum p_T. Note this quantity is invariant under the $\hat{z}$ boost from the laboratory to the center of mass frame. Constant p_T lines in $m_{t\bar{t}} - \theta$ space are plotted in Figure 2.3.

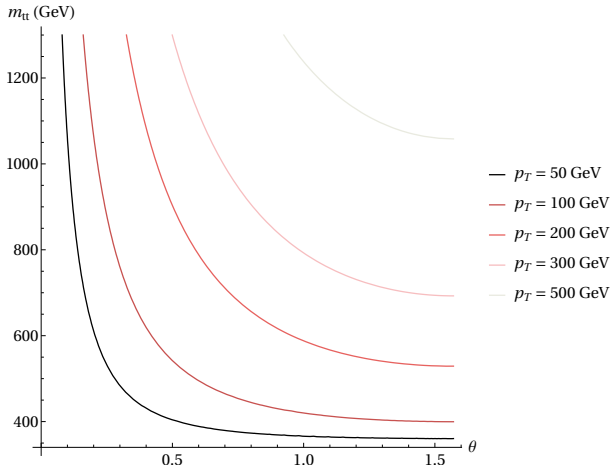

Figure 2.3: Top tranverse momentum as a function of $m_{t\bar{t}}$ and θ.

Another commonly used quantity is the top velocity v (or β) in the center of mass frame, related to $m_{t\bar{t}}$ by:

$$v = \sqrt{1 - \frac{(2m_t)^2}{m_{t\bar{t}}^2}}. \tag{2.4}$$

The established technique to measure spin correlations between weakly decaying particles is via the final momenta of decay products. In order to do this, it is best to use the so–called *helicity basis* in the center of mass frame, given by:

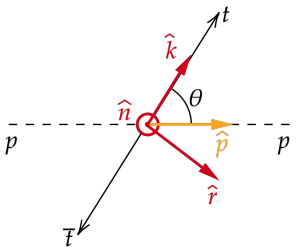

Figure 2.4: Helicity basis $\{\hat{k}, \hat{r}, \hat{n}\}$, $\hat{n}$ is into the page.

$$\hat{k} = \text{top direction}, \quad \hat{r} = \frac{\hat{p} - \hat{k}\cos\theta}{\sin\theta}, \quad \hat{n} = \hat{k} \times \hat{r}, \tag{2.5}$$

where $\hat{p}$ is the beam axis, and θ the production angle. A schematic representation is in Figure 2.4.

2.2 Spin state

We can group all $pp \to t\bar{t}$ processes with a gg initial state in the category of *gluon fusion*, and all processes with a $q\bar{q}$ initial state in the category of $q\bar{q}$ *annihilation*. The relative strength of these two channels is determined by the proton parton density function, and is a function of the collision energy.

The matrix element squared for a $t\bar{t}$ pair production and decay can be written as:

$$|\mathcal{M}_{(c)}|^2 = \overline{\sum} \left| \mathcal{M}(c \to t\bar{t} \to f\bar{f}f\bar{f}b\bar{b}) \right|^2, \quad c = gg \text{ or } q\bar{q}, \tag{2.6}$$

where f and $\bar{f}$ denote light fermions (ℓ, ν, q), and $\overline{\sum}$ stands for average over initial state color and spin, and sum over $t\bar{t}$ color. Neglecting interference between production and decay, which is reasonable given the top quark is relatively long lived with respect to its mass, we can factorize:

$$|\mathcal{M}|^2 = \rho_{k\ell\bar{m}\bar{n}}\, \Gamma_{k\ell}\, \bar{\Gamma}_{\bar{m}\bar{n}}. \tag{2.7}$$

Indices run over the top/antitop quark spin, with barred indices referring to the antiparticle. Top and antitop decay is decoupled from the pair production, and is described by the *decay spin density matrix* defined as:

$$\Gamma_{k\ell} = \mathcal{M}(t_k \to f\bar{f}\, b)\, \mathcal{M}(t_\ell \to f\bar{f}\, b)^\star, \tag{2.8}$$

and similarly for the $\bar{t}$ part. On the other hand, $t\bar{t}$ production is described by the *production spin density matrix*:

$$\rho_{k\ell\bar{m}\bar{n}} = \overline{\sum} \mathcal{M}(c \to t_k \bar{t}_{\bar{m}})\, \mathcal{M}(c \to t_\ell \bar{t}_{\bar{n}})^\star. \tag{2.9}$$

This is the density matrix for the $t\bar{t}$ spin system, up to a normalization constant proportional to the total cross section. It implicitly depends on the production channel $c = gg$ or $q\bar{q}$.

The most general form for a density matrix in $\mathbb{C}^2 \otimes \mathbb{C}^2$ space is:

$$\rho = \frac{1}{4} \left(\mathbb{1} \otimes \mathbb{1} + B_i\, \sigma_i \otimes \mathbb{1} + \bar{B}_j\, \mathbb{1} \otimes \sigma_j + C_{ij}\, \sigma_i \otimes \sigma_j \right), \tag{2.10}$$

where σ are the Pauli matrices and $i, j = 1, 2, 3$ label an orthogonal reference frame. The first factor in the tensor product is the top spin space and the second factor is the antitop spin space. Using this form for (2.9), expectation values for the top and antitop spin projections m_i and $\bar{m}_j$ are given by:

$$\langle m_i \rangle = \mathrm{Tr}\left[\rho\, \sigma_i \otimes \mathbb{1}\right] = B_i, \tag{2.11}$$

$$\langle \bar{m}_j \rangle = \mathrm{Tr}\left[\rho\, \mathbb{1} \otimes \sigma_j\right] = \bar{B}_j, \tag{2.12}$$

$$\langle m_i \bar{m}_j \rangle = \mathrm{Tr}\left[\rho\, \sigma_i \otimes \sigma_j\right] = C_{ij}, \tag{2.13}$$

where to avoid factors of two appearing in our formulae we have taken the two values of m and $\bar{m}$ to be ± 1 and not $\pm\frac{1}{2}$.

Using equations (2.11)–(2.13) we can give physical meaning to the parameters in ρ: B and $\bar{B}$ are the individual top/antitop spin, and C characterizes correlations. These parameters are not all independent. In the Standard Model,

$$C = C^T, \tag{2.14}$$

up to small C, P, and CP violating terms, and $B = \bar{B}$, with:

$$B = \bar{B} = 0, \tag{2.15}$$

up to small P violating terms.

Extensive calculations for B, $\bar{B}$, and C can be found in [35, 36, 37, 38]. Each of the fifteen values in (2.10) can be probed by different observables. As explained in the following, differential cross sections are sensitive to B and $\bar{B}$ (differential with respect to the angle of emission of decay products), doubly differential cross sections are sensitive to C. In a dilepton final state an interesting observable is the angle between the two leptons, sensitive to $\mathrm{Tr}[C]$.

Evidence for $t\bar{t}$ spin correlations was first observed by the ATLAS experiment at the LHC in 2012 [39]. The ATLAS and CMS experiments have reported many measurements of $t\bar{t}$ spin correlations, using various observables in decay channels containing two charged leptons or one lepton and one jet, [40, 41, 42, 43, 44, 45]. All measurements so far agree with Standard Model predictions.

2.3 Observables

As already noted, it is a general feature of weak decays that the angular distribution of decay products is correlated with the parent particle's spin. In the Standard Model, a weakly decaying fermion has differential width [36]:

$$\frac{1}{\Gamma}\frac{d\Gamma}{d\cos\theta_a} = \frac{1 + B_a \alpha \cos\theta_a}{2}, \tag{2.16}$$

where θ_a is the angle between the momentum of a chosen decay product and the a axis, and $-1 \leq B_a \leq 1$ is the expectation value of the original spin along a. All momenta are evaluated in the parent rest frame.

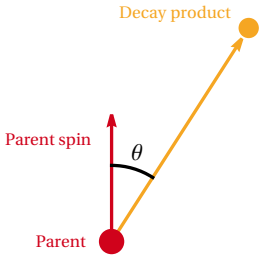

Figure 2.5: Schematic representation of the decay of a fermion.

The parameter α in (2.16) is known as the *spin analyzing power* and measures how well a given daughter probes the spin of its parent. Standard Model values of α for different particles are in Table 2.1, and a plot is in Figure 2.6. The most favorable final state is the one containing a charged lepton, for which $|\alpha| = 1$, its maximum possible value.

Particle	α
e^+, μ^+, τ^+	1.00
$\bar{d}$, $\bar{s}$	0.94
u, c	−0.30
b	−0.39

Table 2.1: Standard model values of the spin analyzing power for the $t \to X$ decay, [46] [47]. Values for antiparticles differ by a sign.

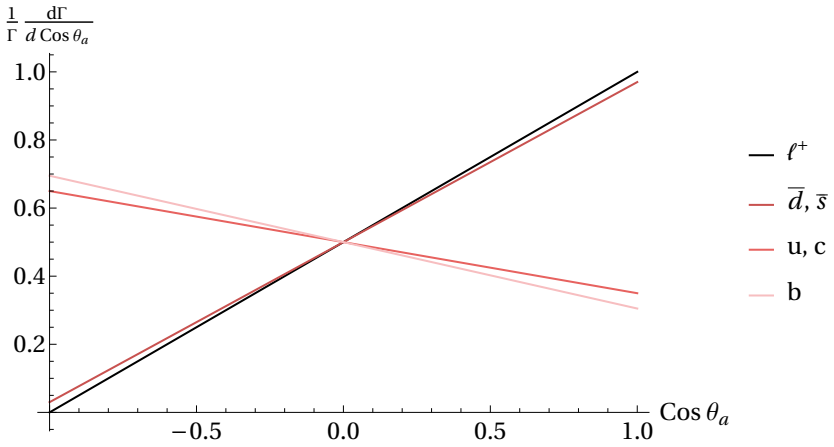

Figure 2.6: Differential width for different decay products, see equation (2.16), for a fully polarized ensamble of top quarks, $B_a = 1$.

The decay of polarized $t\bar{t}$ pairs into a dilepton final state follows a generalization of (2.16), and allows reconstruction of the parents' spin by analyzing angular correlation in the lepton momenta. The differential cross section for $t\bar{t} \to \ell^+\ell^-$ in the absence of kinematic cuts is given by [38]:

$$\frac{1}{\sigma}\frac{d^4\sigma}{d\Omega\, d\bar{\Omega}} = \frac{1}{16\pi^2}\left(1 + B\cdot\hat{\ell}^+ - \bar{B}\cdot\hat{\ell}^- - \hat{\ell}^+\cdot C\cdot\hat{\ell}^-\right), \tag{2.17}$$

where Ω and $\bar{\Omega}$ are the solid angles of the leptons in their parent top rest frame. Since the spin measurement involves one lepton and one antilepton, factors of $\alpha_{\ell^+}\alpha_{\ell^-} = -1$ appear in the formula. Integration of the azimuthal angles gives:

$$\frac{1}{\sigma}\frac{d^2\sigma}{d\cos\theta_a\, d\cos\bar{\theta}_b} = \frac{1}{4}\left(1 + B_a\cos\theta_a - \bar{B}_b\cos\bar{\theta}_b - C_{ab}\cos\theta_a\cos\bar{\theta}_b\right), \tag{2.18}$$

where θ_a is the angle between the antilepton momentum and the a-th axis in its parent top rest frame, and $\bar{\theta}_b$ is the angle between the lepton momentum and the b-th axis in its parent antitop rest frame. Relevant reference frames should be reached in a two step

process, first boosting to the $t\bar{t}$ center of mass frame, then to each top with a rotation free boost.

By changing variables and integrating, the differential cross section with respect to $\cos\theta_a \cos\bar{\theta}_b$ is given by:

$$\frac{1}{\sigma}\frac{d\sigma}{d(\cos\theta_a \cos\bar{\theta}_b)} = \frac{1}{2}\left(C_{ab}\cos\theta_a \cos\bar{\theta}_b - 1\right)\log\left|\cos\theta_a \cos\bar{\theta}_b\right|. \tag{2.19}$$

A plot of (2.19) for different values of C_{ab} is in Figure 2.7.

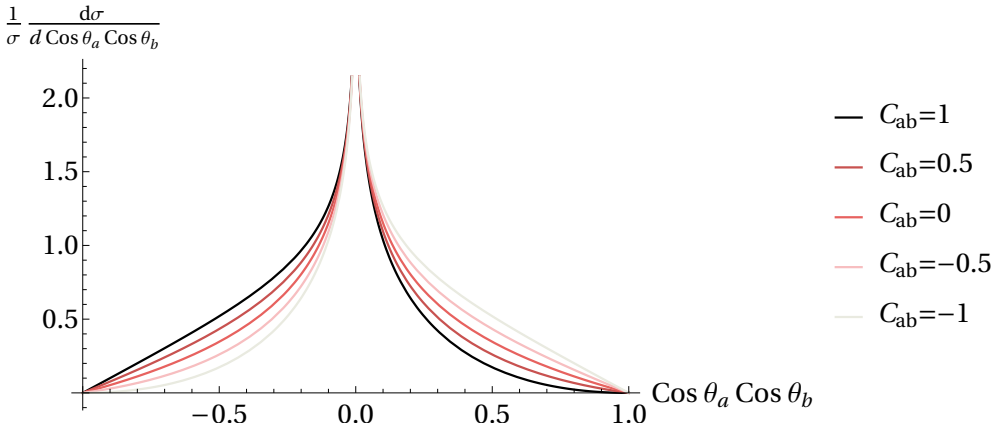

Figure 2.7: Differential cross section for $t\bar{t} \to \ell^+\ell^-$ with respect to the variable $\cos\theta_a \cos\bar{\theta}_b$, as in equation (2.19).

Restoring spin analyzing powers, the expectation value is given by:

$$\boxed{\langle\cos\theta_a \cos\bar{\theta}_b\rangle = \frac{\alpha\bar{\alpha}}{9}C_{ab} = \frac{\alpha\bar{\alpha}}{9}\langle m_a \bar{m}_b\rangle,} \tag{2.20}$$

where $\alpha\bar{\alpha} = -1$ for a dilepton final state.

Remark. All results are derived in the narrow width approximation for top quarks. Near production threshold and in particular when $|m_{t\bar{t}} - 2m_t| \sim \Gamma_t$, interference effects between the initial and final state can become important, in principle distorting the distributions (2.16) and (2.17). In our analysis we generate events using the full $2 \to 6$ matrix element that does not assume $\Gamma_t = 0$. Results are found to be in agreement with the theoretical expectations derived using the narrow width approximation.

Chapter 3

Entanglement and Bell inequalities in $t\bar{t}$ pairs

3.1 Entanglement

A notable difference between entanglement tests for $t\bar{t}$ pairs and low energy experiments like those quoted in Section 1.2 is that the $t\bar{t}$ quantum state produced in colliders is mixed, as the initial state is determined by the parton density function, without external control.

An entanglement test for $t\bar{t}$ pairs has been proposed [3] in 2020 using the Peres–Horodecki criterion, see Chapter 1. The partial transpose of the density matrix (2.10) is given by:

$$(1\otimes T)\rho = \frac{1}{4}\begin{pmatrix} 1+B_3+\bar{B}_3+C_{33} & \bar{B}_1+C_{31}+i(\bar{B}_2+C_{32}) & B_1+C_{13}-i(B_2+C_{23}) & C_{11}+C_{22}+i(C_{12}-C_{21}) \\ \bar{B}_1+C_{31}-i(\bar{B}_2+C_{32}) & 1+B_3-\bar{B}_3-C_{33} & C_{11}-C_{22}-i(C_{12}+C_{21}) & B_1-C_{13}-i(B_2-C_{23}) \\ B_1+C_{13}+i(B_2+C_{23}) & C_{11}-C_{22}+i(C_{21}+C_{12}) & 1-B_3+\bar{B}_3-C_{33} & \bar{B}_1-C_{31}+i(\bar{B}_2-C_{32}) \\ C_{11}+C_{22}+i(C_{21}-C_{12}) & B_1-C_{13}+i(B_2-C_{23}) & \bar{B}_1-C_{31}-i(\bar{B}_2-C_{32}) & 1-B_3-\bar{B}_3+C_{33} \end{pmatrix}. \tag{3.1}$$

There is no need to lose generality by fixing a specific basis, so we label entries of B, $\bar{B}$, and C using generic $1,2,3$ indices.

By the Peres–Horodecki criterion, this matrix has a negative eigenvalue if and only if the corresponding spin state is entangled.

Consider the matrix constructed with the first and fourth components of 3.1,

$$\frac{1}{4}\begin{pmatrix} 1+B_3+\bar{B}_3+C_{33} & C_{11}+C_{22}+i(C_{12}-C_{21}) \\ C_{11}+C_{22}+i(C_{21}-C_{12}) & 1-B_3-\bar{B}_3+C_{33} \end{pmatrix}. \tag{3.2}$$

If this matrix has one negative eigenvalue, then (3.1) has one as well. A *sufficient*

condition for entanglement is thus:

$$\det \begin{pmatrix} 1+B_3+\bar{B}_3+C_{33} & C_{11}+C_{22}+i(C_{12}-C_{21}) \\ C_{11}+C_{22}+i(C_{21}-C_{12}) & 1-B_3-\bar{B}_3+C_{33} \end{pmatrix} < 0. \tag{3.3}$$

Explicitly,

$$-(B_3+\bar{B}_3)^2-(C_{11}+C_{22})^2-(C_{21}-C_{12})^2+(1+C_{33})^2<0. \tag{3.4}$$

Since $-1 \leq C_{33} \leq 1$, a sufficient condition is:

$$-C_{33}+|C_{11}+C_{22}|>1, \tag{3.5}$$

or equivalently:

$$-C_{11}-C_{22}-C_{33}>1 \tag{3.6}$$
$$C_{11}+C_{22}-C_{33}>1 \tag{3.7}$$

are both sufficient conditions for entanglement. We stress the only condition *equivalent* to entanglement is the one based on negative eigenvalues of (3.1), all other conditions are only *sufficient*.

3.2 Bell inequalities

In Section 3.1 we argued that $t\bar{t}$ pairs produced in certain regions of phase space have their spins entangled, and reviewed a way to experimentally confirm this prediction. A stronger test is to set up a Bell inequality and look for violations. Such violation would give a concrete, theory independent confirmation of non-classical behavior.

The CHSH inequality (1.18) can be written as:

$$|\langle m_a \bar{m}_b\rangle - \langle m_a \bar{m}_{b'}\rangle| + |\langle m_{a'} \bar{m}_b\rangle + \langle m_{a'} \bar{m}_{b'}\rangle| \leq 2, \tag{3.8}$$

where m and $\bar{m}$ are t and $\bar{t}$ spin along the unit vectors a, a' and b, b'. We take the two possible values of m and $\bar{m}$ to be ± 1.

An equivalent form of the CHSH inequality is:

$$\left|\langle m_a \bar{m}_b\rangle - \langle m_a \bar{m}_{b'}\rangle + \langle m_{a'} \bar{m}_b\rangle + \langle m_{a'} \bar{m}_{b'}\rangle\right| \leq 2. \tag{3.9}$$

This form seems weaker than (3.8), but is actually equivalent to it. This is seen by noting one is free to redefine the axis by introducing an extra minus sign that is absorbed inside absolute values. Contrary to (3.8), inequality (3.9) is readily testable when the density matrix ρ for the system is available. In the case of two spin $\frac{1}{2}$ particles the CHSH inequality reduces to:

$$|\langle \mathcal{C}\rangle| = \left|\,\mathrm{Tr}[\mathcal{C}\,\rho]\,\right| \leq 2, \tag{3.10}$$

where $\mathcal{C}$ is the CHSH operator,

$$\mathcal{C} = (a_i b_j - a_i b'_j + a'_i b_j + a'_i b'_j)\, \sigma_i \otimes \sigma_j. \tag{3.11}$$

We denote a, b, a', b' the unit vectors describing orientations along which we measure spin. Recall that the most general density matrix is the one in equation (2.10). We have the following:

Theorem. *The CHSH inequality* (3.9) *evaluated for a system described by the density matrix* (2.10) *reaches a maximum value of:*

$$\max_{a\,a'\,b\,b'} \left| \langle m_a \bar{m}_b \rangle - \langle m_a \bar{m}_{b'} \rangle + \langle m_{a'} \bar{m}_b \rangle + \langle m_{a'} \bar{m}_{b'} \rangle \right| = 2\sqrt{\lambda + \lambda'}, \tag{3.12}$$

where λ and λ' are the two largest eigenvalues of $C^T C$. The maximal value is obtained for the following choice of directions:

$$a = Cd, \quad a' = Cd', \tag{3.13}$$

$$b = d\cos\varphi + d'\sin\varphi, \quad b' = -d\cos\varphi + d'\sin\varphi, \tag{3.14}$$

where d and d' are eigenvectors of $C^T C$ of eigenvalues λ, λ', and $\tan\varphi = \sqrt{\frac{\lambda'}{\lambda}}$.

Proof. (This proof is partially based on arguments in [48], a different proof using Lagrange multipliers is in [26].) We want to evaluate:

$$|\langle \mathcal{C} \rangle| = \left| \mathrm{Tr}[\mathcal{C}\,\rho] \right| = \left| (a_i b_j - a_i b'_j + a'_i b_j + a'_i b'_j) C_{ij} \right|. \tag{3.15}$$

Consider the pair of orthogonal and unit norm vectors:

$$d = \frac{b - b'}{2\cos\varphi}, \quad d' = \frac{b + b'}{2\sin\varphi}, \tag{3.16}$$

where $\cos^2\varphi = \frac{1}{2}(1 - b \cdot b')$. We can rewrite:

$$|\langle \mathcal{C} \rangle| = |2\, a^T C d \cos\varphi + 2\, a'^T C d' \sin\varphi|. \tag{3.17}$$

We now maximize this expression with respect to all the variables. First for φ:

$$\max_{\varphi} |\langle \mathcal{C} \rangle| = 2\sqrt{(a^T C d)^2 + (a'^T C d')^2}. \tag{3.18}$$

Note $a^T C d = |a||Cd| \cos\theta$ where θ is the angle between a and Cd, so to maximize one takes a in direction Cd, and similarly a' in direction Cd':

$$\max_{\varphi, a, a'} |\langle \mathcal{C} \rangle| = 2\sqrt{|Cd|^2 + |Cd'|^2}. \tag{3.19}$$

Finally, notice $|Cd|^2 = d^T C^T C d$. Since the matrix $C^T C$ is real and symmetric, it has orthogonal eigenvectors and positive eigenvalues. We take d and d' equal to the two eigenvectors corresponding to the largest eigenvalues:

$$\max_{\varphi, a, a', d, d'} |\langle \mathcal{C} \rangle| = 2\sqrt{\lambda + \lambda'}. \tag{3.20}$$

Note this also implies $\tan\varphi = \sqrt{\frac{\lambda'}{\lambda}}$. This completes the proof.

3.3 Violation of Bell inequalities implies entanglement

We stress a point about the chain of logical implications highlighted in (1.10):

$$\begin{matrix}\text{Violation of}\\ \text{Bell inequalities}\end{matrix} \implies \text{Entanglement} \implies \text{Correlations.} \tag{3.21}$$

The second logical implication is trivial; as a consistency check, we show the first logical implication holds in a simple case.

Translating into the language of top spin correlations, both the presence of entanglement and a violation of Bell inequalities are probed with conditions on the C_{ij} matrix. Assuming the top and antitop polarizations B and $\bar{B}$ are numerically small compared to entries of the correlation matrix C, the spin density matrix for the $t\bar{t}$ system can be written as:

$$\rho = \frac{1}{4}\left(\mathbb{1}\otimes\mathbb{1} + C_{ij}\,\sigma_i\otimes\sigma_j\right). \tag{3.22}$$

Further assuming $C = C^T$, as is approximately the case in the Standard Model, the C matrix can be diagonalized with a rotation and can be taken of the form $C = \text{diag}\,\{C_1, C_2, C_3\}$. Since the density matrix of a system is positive definite, the following relations about eigenvalues of ρ hold true in general:

$$\begin{cases} C_1 + C_2 + C_3 < 1, \\ -C_1 - C_2 + C_3 < 1, \\ -C_1 + C_2 - C_3 < 1, \\ C_1 - C_2 - C_3 < 1. \end{cases} \tag{3.23}$$

A calculation shows the Peres–Horodecki criterion yields:

$$\min\left\{C_1 - C_2 - C_3,\, -C_1 + C_2 - C_3,\, -C_1 - C_2 + C_3,\, C_1 + C_2 + C_3\right\} < 1, \tag{3.24}$$

as a necessary and sufficient condition for entanglement. A violation of the CHSH inequality occurs when the two largest eigenvalues of C^TC, that is C_1^2, C_2^2, and C_3^2, sum to a value greater than 1:

$$C_1^2 + C_2^2 + C_3^2 - \min\left\{C_1^2,\, C_2^2,\, C_3^2\right\} > 1. \tag{3.25}$$

Figure 3.1 plots the outcome of the entanglement test (3.24) together with regions where the CHSH inequality (3.25) is violated. The geometrical structure that emerges is the first iteration of the famous Sierpinski fractal in three dimensions. By examining the plot, we are reassured that the logical implication (1.10) holds for the $t\bar{t}$ system as well.

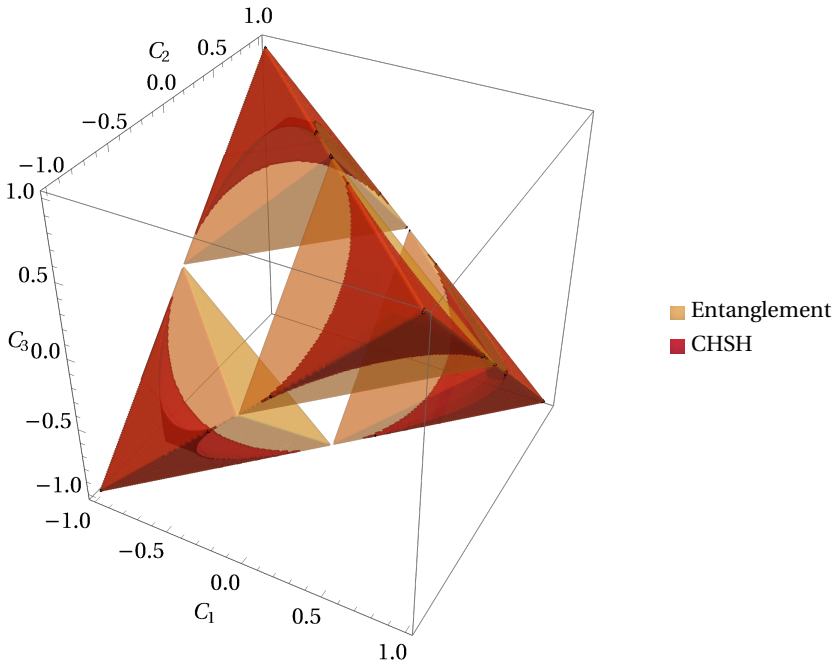

Figure 3.1: Plot of the entanglement test (3.24) and of regions where the CHSH inequality (3.25) is violated, assuming $B = \bar{B} = 0$ and $C = \text{diag}\{C_1, C_2, C_3\}$. Regions where the corresponding density matrix would not be positive definite are excluded from the plot.

3.4 Bias in eigenvalue estimation.

The result proved in Section 3.2 suggests an indirect experimental test for violations of Bell inequalities. First, compute the C_{ab} matrix by fitting the observed distribution of $\cos\theta_a \cos\bar{\theta}_b$, then evaluate the two largest eigenvalues λ, λ' of $C^T C$. If one finds:

$$\lambda + \lambda' > 1, \tag{3.26}$$

the CHSH inequality is guaranteed to be violated for some choice of measurement axis, with a maximal violation of $2\sqrt{\lambda + \lambda'}$.

The $\lambda + \lambda'$ test statistic is challenging to evaluate from data. Random fluctuations are more likely to drive the eigenvalues of $C^T C$ towards $+\infty$ rather than towards $-\infty$, since eigenvalues of a symmetric real matrix can not be pushed negative. Furthermore, when selecting the two largest eigenvalues λ and λ' one is more likely to pick the ones that fluctuated up rather than the ones that fluctuated down.

The two effects highlighted above produce a considerable bias in the estimated value of $\lambda + \lambda'$. To see the biasing effect at play, we generate random 3×3 matrices of the form $C = \mathbb{1} + \Delta$ where each Δ_{ij} is a gaussian random variable with mean 0 and standard deviation σ. The eigenvalues of $C^T C$ are then computed and plotted in Figure 3.2. A

bias towards the right is clearly seen. The sum of the two largest eigenvalues is then plotted in Figure 3.3, we see that the bias towards the right is further increased.

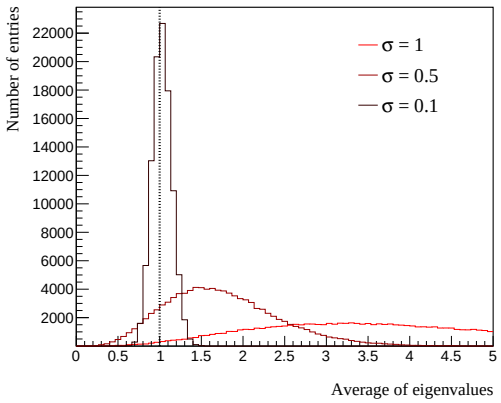

Figure 3.2: Average of the three eigenvalues of $C^T C$ for 10^5 randomly generated C matrices, see text. The true value $\lambda_{\text{avg}} = 1$ found for $\sigma = 0$ is indicated by the dotted line.

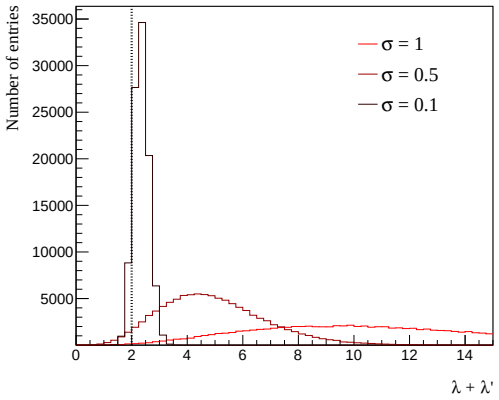

Figure 3.3: Sum of the two largest eigenvalues of $C^T C$ for 10^5 randomly generated C matrices, see text. The true value $\lambda + \lambda' = 2$ found for $\sigma = 0$ is indicated by the dotted line.

The bias effect present in the evaluation of $\lambda + \lambda'$ can hint at a violation of the CHSH inequality even when none is actually present in the data, or can artificially enhance the statistical significance of a violation observed. Since this systematic effect is hard to evaluate in practice, we opt for a different approach. Nevertheless, the numerical value of $2\sqrt{\lambda + \lambda'}$ remains an useful guide during the analysis, especially when evaluated using a large statistical sample for which the bias is not particularly significant.

3.5 Loopholes

When performing an EPR–like experiment several loopholes have to be addressed, such as the ones highlighted in Section 1.2. As already noted, high energy particle physics tests are far from being able to close all loopholes.

- The most prominent loophole is that the $pp \to t\bar{t} \to \cdots$ event happens deep inside a hadron collider, while the setup for an EPR experiment requires outside intervention during the correlation measurement, to choose *freely* (that is, unknown to the system that is being measured) what to measure. There is no ready fix for this loophole for high energy physics experiments.

- Only a small fraction of events in collider experiments is actually recorded and usable for physics. To close the fair sampling loophole, we have to assume the

events that are recorded are a fair representation of the bulk, and had we used a perfect detector the result would not have changed. Although there is no way to test experimentally if a given detector is sampling fairly, since lost events are by definition unknown, it is certainly believable this is the case for actual experiments such as particle detectors at the LHC. This assumption goes under the name of *fair sampling hypothesis*

- Another loophole that has to be addressed is the so–called locality loophole. It could be the case that the $t\bar{t}$ system exchanges classical information at $v \leq c$ through hidden particles, and the spin correlations we see are not the outcome of a quantum effect. To address this problem in a satisfactory manner, one should only consider events in which the t and $\bar{t}$ decays are spacelike separated. There is no feasible experimental way to make this distinction on a event-by-event basis, only a statistical argument can be made.

  In the center of mass frame, top quarks are emitted back to back with velocity β given by (2.4) as a function of $m_{t\bar{t}}$. After a brief ($\sim \Gamma_t^{-1}$) flight, both particles decay and eventually stable daughters are emitted carrying information about the original spin state. The condition for spacelike separation of the t and $\bar{t}$ decays can be cast in the form:

$$\left|\frac{t_1 - t_2}{t_1 + t_2}\right| < v, \tag{3.27}$$

  where v is the velocity of both particles. We denote t_1 and t_2 the top and antitop lifetimes, that follow the exponential distribution:

$$f(t;\, \gamma) = \gamma\Gamma\, e^{-\gamma\Gamma t}, \tag{3.28}$$

  where $\Gamma \equiv \Gamma_t = 1.2\,\text{GeV}$ is the top width and $\gamma = 1/\sqrt{1 - v^2}$ is the Lorentz factor for the two tops.

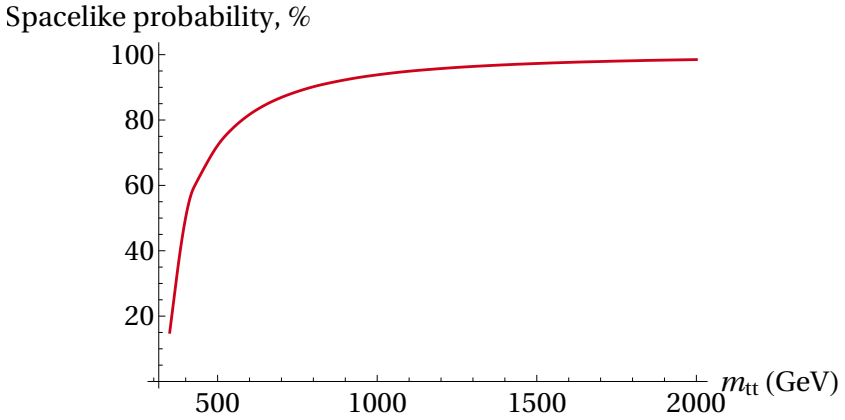

Figure 3.4: Fraction of t and $\bar{t}$ decays that are spacelike separated, for $t\bar{t}$ pairs with a given $m_{t\bar{t}}$.

In Figure 3.4 we plot a Monte Carlo evaluation of the probability of spacelike separated decays as a function of $m_{t\bar{t}}$. More than half of $t\bar{t}$ pairs decay spacelike–separated for $m_{t\bar{t}} > 400\,\text{GeV}$, the fraction rises to 90% for $m_{t\bar{t}} > 800\,\text{GeV}$ and to 98% for $m_{t\bar{t}} > 1700\,\text{GeV}$.

To close the locality loophole in a satisfactory manner, an EPR experiment should only focus on the high–$m_{t\bar{t}}$ region. Luckily, as we will see, violations of Bell inequalities are expected for $m_{t\bar{t}}$ of order TeV.

Chapter 4

Parton–level analysis

In order to investigate $t\bar{t}$ spin correlations we consider the process in which a $t\bar{t}$ pair is produced in s channel and subsequently decays in a dilepton final state:

$$p\,p \to t\bar{t} \to b\,\bar{b}\,\ell^+\,\ell^-\,\nu\,\bar{\nu}, \tag{4.1}$$

At the TeV scale the cross section for the $2 \to 6$ process $p\,p \to b\,\bar{b}\,\ell^+\,\ell^-\,\nu\,\bar{\nu}$ is dominated by the five diagrams of Figure 4.1. Although diagrams (c) and (d) are numerically subleading, they are known to produce interference terms and should not be neglected [49, 50].

Figure 4.2 plots the cross section for $p\,p \to b\,\bar{b}\,\ell^+\,\ell^-\,\nu\,\bar{\nu}$ as a function of center of mass energy. A large fraction of events feature the production of a $t\bar{t}$ pair in s channel. The dominant production channel is $q\bar{q}$ annihilation for $\sqrt{s} \lesssim 2\,\text{TeV}$ and gluon fusion for higher energy.

4.1 Event generation

We generate processes of the form $2 \to 6$:

$$pp \to \ell^-\,\ell^+\,\nu\,\bar{\nu}\,b\,\bar{b}, \tag{4.2}$$

where $\ell = e, \mu$, taken to be both in same and different flavor combinations: e^+e^-, $e^+\mu^-$, μ^+e^-, and $\mu^+\mu^-$.

Events are generated using MadGraph5_aMC [33]. MadGraph5_aMC@NLO is a self–contained package providing all the elements necessary for Standard Model (and BSM) phenomenology, including the automated computation of Leading and Next-to-Leading Order matrix elements and their matching to parton shower simulations.

We generate events at Leading Order in all coupling constants, where the general strategy is to integrate a cross section produced from tree–level diagrams and obtain a set of unweighted events from it. The computation consists of two steps, *generation* and *running*. In the generation phase, MadGraph constructs the cross section relevant to the process given as input. In our case, the relevant command is:

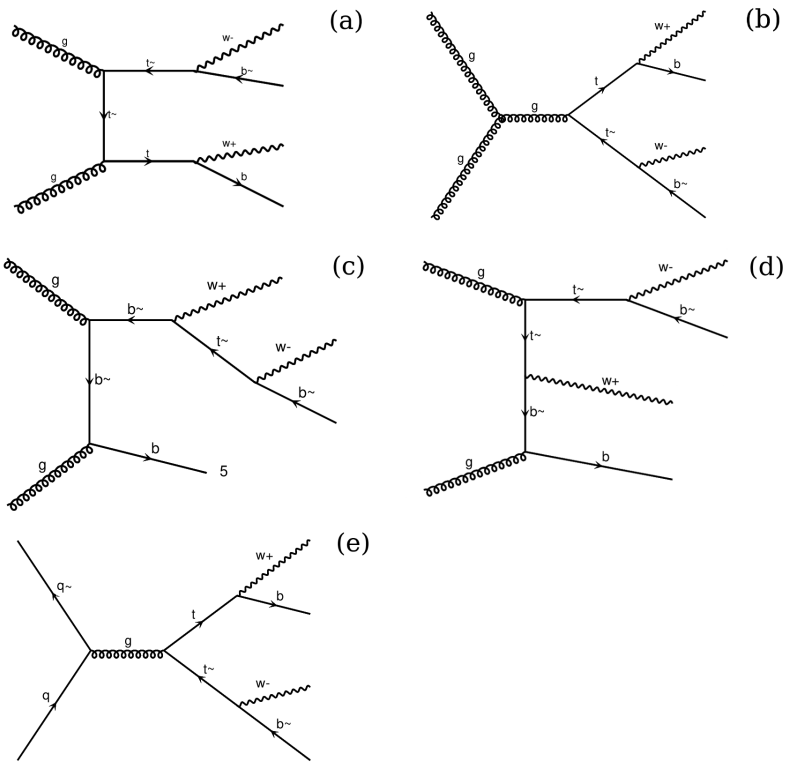

Figure 4.1: Dominant diagrams for $b\bar{b}\,\ell^+\,\ell^-\,\nu\,\bar{\nu}$ production in pp collisions. Diagrams related by mirroring or taking the charge conjugate are identified and only one is drawn.

generate p p > l− l+ vl vl∼ b b∼

This computes the amplitude for the process in 4.2 within the Standard Model. The leading–order matrix element consists of over 3000 diagrams, the numerically leading ones being those in Figure 4.1. Top quarks and W bosons appearing as intermediate states are not put on shell during event generation, so interference effects are fully taken into consideration. We use the following numerical values for input parameters related to top physics:

$$m_t = 173\,\text{GeV}, \quad \Gamma_t = 1.49\,\text{GeV}, \quad m_Z = 91.2\,\text{GeV}, \quad G_F = 1.166 \cdot 10^{-5}\,\text{GeV}^{-2}. \tag{4.3}$$

All particles are assumed to be massless and stable except for t and b quarks, electroweak and Higgs bosons, and the τ lepton. No kinematic cuts are imposed during event generation, except for a lower limit on the invariant mass of same flavor $\ell^+\ell^-$ pairs:

$$m_{\ell^+\ell^-} > 5\,\text{GeV}, \tag{4.4}$$

needed to keep the process $\gamma \to \ell^+\ell^-$ infrared safe (leptons are taken to be massless).

During the running stage, MadGraph integrates the cross section generated previously and produces a given number of unweighted events. The proton–proton initial

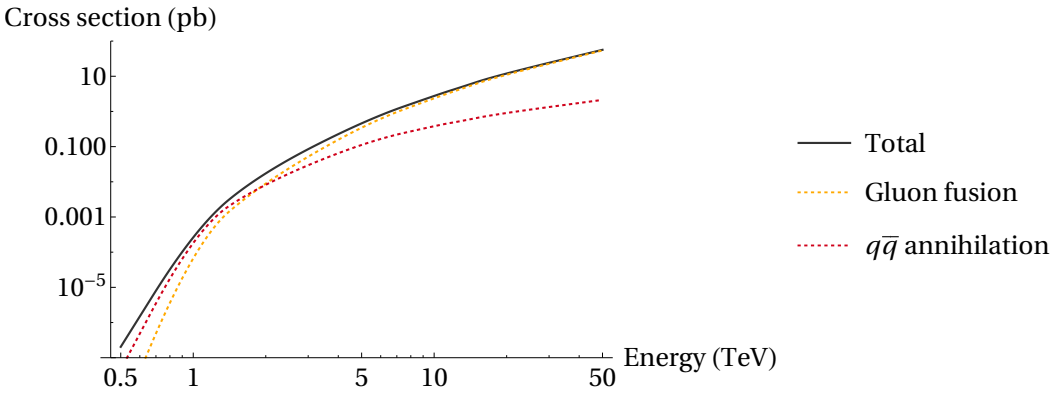

Figure 4.2: Total leading order cross section for $p\,p \to \ell^+\,\ell^-\,\nu\,\bar{\nu}$ as a function of pp center of mass energy, together with relative contributions from diagrams with a gg and $q\bar{q}$ initial state. Values refer to a given flavor final state, e.g. $\ell^+ = e^+$, $\ell^- = \mu^-$.

state includes gluons, and u, d, c, s quarks and antiquarks. Partons are weighted according to a given parton density function. We use the NN23LO1 [34] parton density function at leading order.

We generate events in runs consisting of 10^5 events each. Each run requires a few hours of CPU time on a typical machine, and produces about 70 MB of output in the form of a ROOT TTree. Our final dataset consists of 600 runs, 300 with one electron and one muon, 150 with two electrons, and 150 with two muons. Computations were carried on the CERN batch system.

4.2 Cross section and number of events

The total cross section for $pp \to t\bar{t}$ has been evaluated at NNLO for $\sqrt{s} = 7$ and 14 TeV [51]. The cross section has a strong dependence on the center of mass energy. During Run 2 of the LHC protons were collided with $\sqrt{s} = 13\,\text{TeV}$, for which [50]:

$$\sigma = 832\,^{+20}_{-29} \pm 35\,\text{pb}, \tag{4.5}$$

where the fist error is theoretical and the second is for the PDF and α_s. These results assume $m_t = 172.5\,\text{GeV}$, accounting for the current experimental uncertainty in m_t introduces an additional uncertainty in σ of order $\pm 20\,\text{pb}$. Recent measurements [52] are in agreement with the theoretical prediction,

$$\sigma_{\text{exp}} = 826 \pm 4\,(\text{stat}) \pm 12\,(\text{syst}) \pm 16\,(\text{lumi}) \pm 2\,(\text{beam})\,\text{pb}. \tag{4.6}$$

The differential cross section as a function of the pair kinematic variables $m_{t\bar{t}}$ and θ is plotted in Figure 4.3.

The ratio between gluon fusion and $q\bar{q}$ annihilation is shown in the two plots of Figure 4.4, differential in $m_{t\bar{t}} - \theta$ and in $m_{t\bar{t}}$ and the center of mass rapidity y_{cm}.

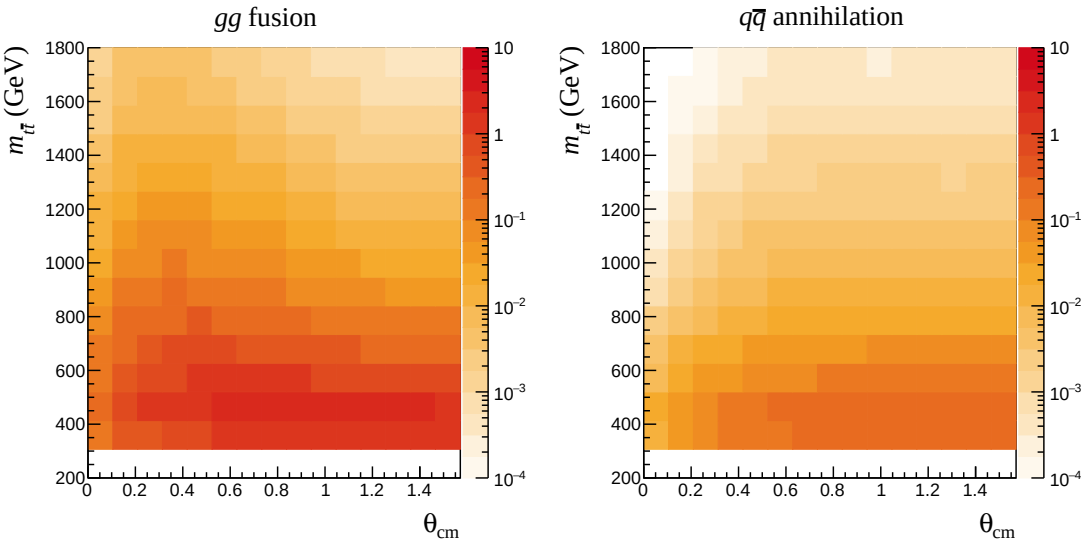

Figure 4.3: Differential cross section $\frac{d\sigma}{dm_{t\bar{t}}\,d\theta}$ in $\frac{\text{pb}}{\text{GeV rad}}$ for $pp \to t\bar{t}$ at $\sqrt{s} = 13\,\text{TeV}$ at Leading Order. Right: $gg \to t\bar{t}$. Left: $q\bar{q} \to t\bar{t}$ for $q = u, d, c, s$. Plots use data from $1300\,\text{fb}^{-1}$ of simulated luminosity.

The $t \to b\,\ell\,\nu$ branching ratio is 11.1% for $\ell = e, \mu$ [53]. This implies a cross section of:

$$\sigma_{t\bar{t}\to 2\ell} = \sigma\,(2 \cdot 11.1\,\%)^2 = 41\,\text{pb} \tag{4.7}$$

for a dilepton final state.

We only consider physical background, consisting of events with a $\ell^-\,\ell^+\,\nu\,\bar{\nu}\,b\,\bar{b}$ final state without an intermediate $t\bar{t}$ pair[1], or with an intermediate $t\bar{t}$ pair that does not decay emitting two prompt light leptons. Further sources of background in the different flavor channel include $t\bar{t}\,V$ events, diboson events, and misidentification of leptons. These backgrounds are known to amount to a few percent of the total [50] and are neglected in this analysis. The same flavor channel is also contaminated from Z + jets events, whose number, after cuts, is at the percent level, comparable with other backgrounds already quoted [45].

The ratio between the signal cross section $\sigma_{t\bar{t}\to 2\ell}$ and the total cross section for (4.2) is evaluated using MadGraph at Leading Order, and is found to be $\sigma_{t\bar{t}\to 2\ell}/\sigma_{pp\to 2\ell} = 0.895$. Assuming this ratio is stable when including higher order corrections, the NNLO total cross section for (4.2) is approximately:

$$\sigma_{pp\to 2\ell} = \frac{\sigma_{t\bar{t}\to 2\ell}}{0.895} = 46\,\text{pb}. \tag{4.8}$$

[1] An event is tagged by MadGraph as containing an s channel top quark if the invariant mass of a $b\,\ell\,\nu$ system is within $15\,\Gamma_t$ of m_t.

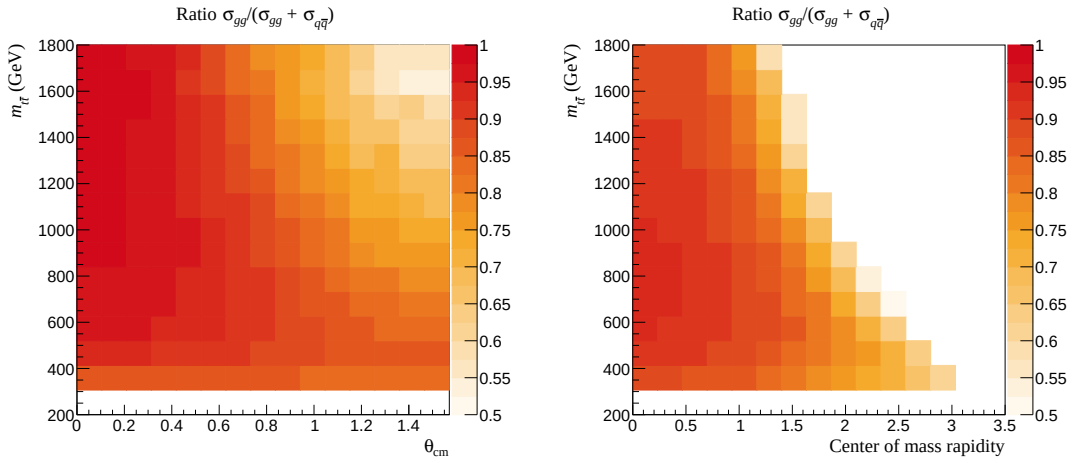

Figure 4.4: Ratio between gluon fusion and total cross section for $pp \to t\bar{t}$ at $\sqrt{s} = 13\,\text{TeV}$ at Leading Order. Right: as a function of $m_{t\bar{t}}$ and θ, Left: as a function of $m_{t\bar{t}}$ and the absolute value of the center of mass rapidity. Plots use data from $1300\,\text{fb}^{-1}$ of simulated luminosity.

Our general strategy is to generate events at Leading Order, reweighting the number of events accounting for the NNLO value for the cross section.

We generate 60 million events of the form $pp \to \ell^- \ell^+ \nu \bar{\nu} b \bar{b}$ at Leading Order. Considering the NNLO cross section, this is equivalent to an integrated luminosity of $\sim 1300\,\text{fb}^{-1}$.

For comparison, after Run 2 (2015 - 2018) of the LHC the total luminosity recorded by the ATLAS Detector is [54]:

$$\mathcal{L}_{\text{Run 2}} = 139 \pm 2\,\text{fb}^{-1}. \tag{4.9}$$

After the second Long Shutdown (2019 - 2021), the upcoming Run 3 (2022 - 2024) of the LHC should deliver $300\,\text{fb}^{-1}$ of integrated luminosity, for a Run 2 + Run 3 total of $450\,\text{fb}^{-1}$. After 2027, the High Luminosity LHC upgrade should increase the luminosity available to experiments by a factor of ∼10, achieving an integrated luminosity of order $4000\,\text{fb}^{-1}$ over a ten year period.

The approximate event yield for the process $pp \to \ell^- \ell^+ \nu \bar{\nu} b \bar{b}$ combining Run 2 and Run 3 of the LHC is:

$$N_{\text{Run 2 + Run 3}} \approx 20\,000\,000 \text{ events} \tag{4.10}$$

In the following we will run the analysis over 20 million events.

4.3 General results

The smallest eigenvalue of (3.1), a marker of entanglement due to the Peres–Horodecki criterion, is evaluated bin by bin in $t\bar{t}$ phase space in the top plot of Figure 4.5.

The generic structure of entanglement in $t\bar{t}$ phase space seems to be sensitive to the top transverse momentum, see Figure 2.3, with the middle transition region occurring around $p_T = m_t$.

The test statistic $2\sqrt{\lambda + \lambda'}$, equal to the maximal value in the CHSH inequality, is also evaluated in $t\bar{t}$ phase space, and results are in the bottom plot of Figure 4.5.

Authors of [4] in 2021 concluded the null hypothesis $\lambda + \lambda' \leq 1$ can be excluded to 98% CL using existing data from Run 2 of the LHC and to 99.99% CL after the next high luminosity run. The systematic effect highlighted in Section 3.4 might imply the statistical significance of this result has been overestimated.

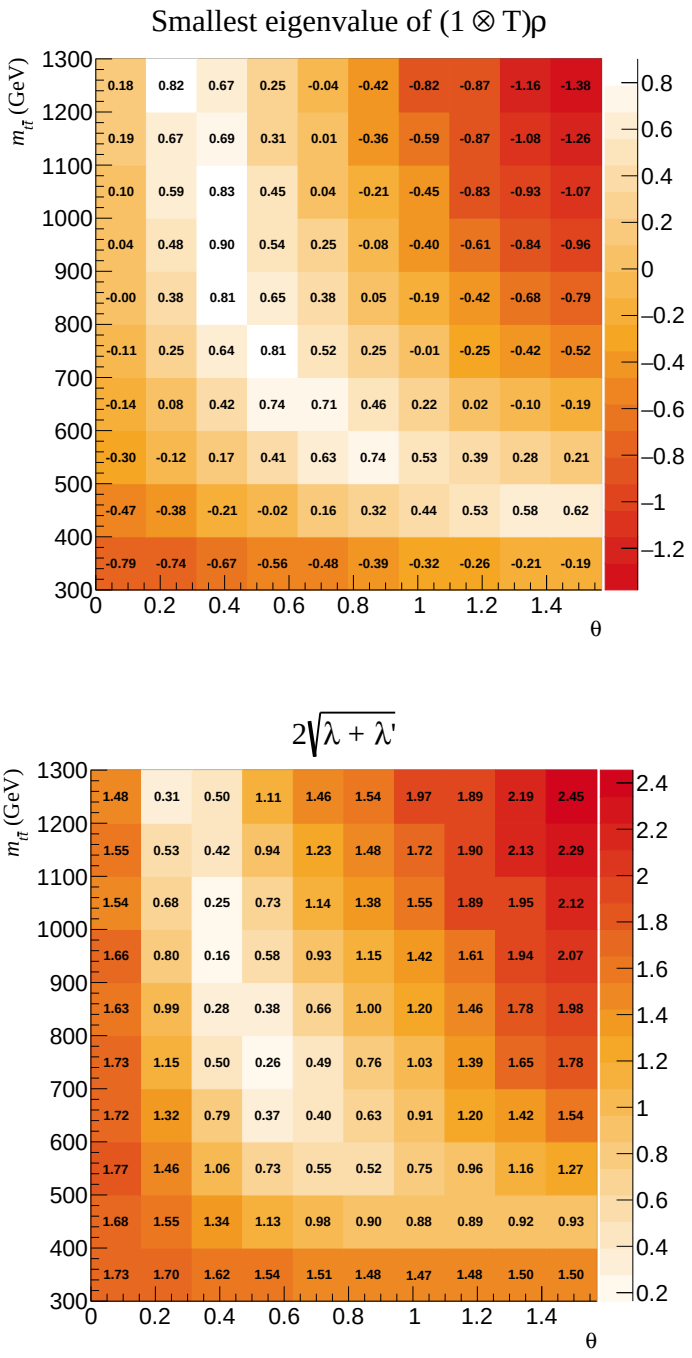

Figure 4.5: Markers of entanglement and of violation of Bell inequalities in $t\bar{t}$ phase space. Top: smallest eigenvalue of (3.1), a negative value is equivalent to entanglement. Bottom: maximum value in the CHSH inequality using (4.11). Plots use 1300 fb^{-1} of simulated luminosity, for which statistical uncertainty is negligible.

4.4 Data analysis procedure

The left hand side of the CHSH inequality, maximized over all possible choices of axis a, a', b, b' has been shown to be equal to:

$$\max_{a\,a'\,b\,b'} \left| \langle m_a \bar{m}_b \rangle - \langle m_a \bar{m}_{b'} \rangle + \langle m_{a'} \bar{m}_b \rangle + \langle m_{a'} \bar{m}_{b'} \rangle \right| = 2\sqrt{\lambda + \lambda'}. \tag{4.11}$$

where λ and λ' are the two largest eigenvalues of $C^T C$.

In order to obtain estimators for the left hand side of the CHSH inequality and for other observables of interest such as the entanglement markers (3.6) and (3.7) we proceed as follows.

We first evaluate from a large number of simulated events the optimal axis a, a', b, b' along which to measure spin using equations (3.13) and (3.14) in every phase space region of interest. Once the measurement axis have been fixed, the reconstructed C matrix is used to evaluate the expectation value of the CHSH operator (3.11):

$$\langle \mathcal{C} \rangle = (a_i b_j - a_i b'_j + a'_i b_j + a'_i b'_j)\, C_{ij}. \tag{4.12}$$

The statistical significance of a violation of $|\langle \mathcal{C} \rangle| < 2$ is then straightforward to calculate using standard statistical data analysis tools.

Entries of the C matrix are evaluated using $t\bar{t} \to \ell^+\ell^-$ events as described in Section 2.3, either by fitting the distribution (2.19) or using the relation between expectation values found in (2.20). In Figure 4.6 we show the distribution at parton level of the nine observables $\cos\theta_i \cos\bar{\theta}_j$ used as estimators for the entries C_{ij}. The distributions are accurately described by the theoretical prediction in (2.19), and values of C_{ij} extracted using the two different estimators (a fit of (2.19) or (2.20)) agree within their statistical uncertainties.

Since the C matrix is approximately symmetric, its entries are highly correlated. The technique usually followed by experimental collaborations is to work with the new set of variables C_{ii}, $C_{ij} + C_{ji}$, and $C_{ij} - C_{ji}$. As it turns out, we will only need entries on the diagonal, so for our purposes it is enough to see that C_{11}, C_{22} and C_{33} have negligible correlation. The physics behind this argument is clear, as C_{ii} and C_{jj} for $i \neq j$ relate to the spin projection along perpendicular axis. However, since the same dataset is used to evaluate all entries it might be the case that spurious effects appear. Figure 4.7 shows scatter plots between pairs of entries on the diagonal of C. The correlation coefficient between C_{ii} and C_{jj} never exceeds 0.01 for $i \neq j$ in helicity basis. Profile histograms of the scatter plots in Figure 4.7 are shown in Figure 4.8. Correlations are seen at the percent level. In the following, we will assume correlations are subleading with respect to statistical uncertainties in each entry.

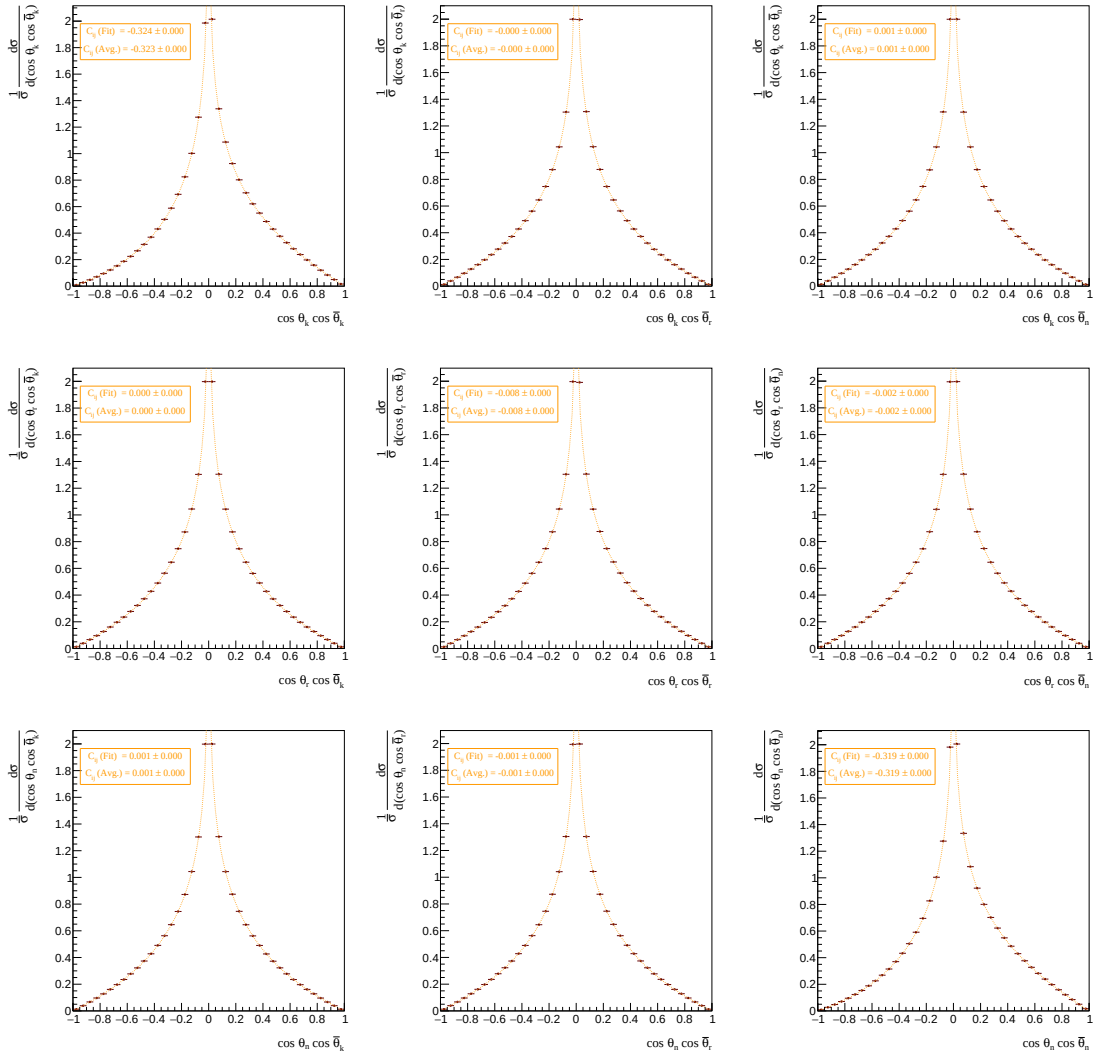

Figure 4.6: Parton level distribution of $\cos\theta_i \cos\bar{\theta}_j$ in helicity basis, $i, j = k, r, n$. The value of C_{ij} is extracted by fitting the function in (2.19) and using the expectation value relation (2.20). Plots use $1300\,\mathrm{fb}^{-1}$ of simulated luminosity and cover the whole $t\bar{t}$ phase space without kinematic cuts. Statistical uncertainty is always beyond the quoted digits.

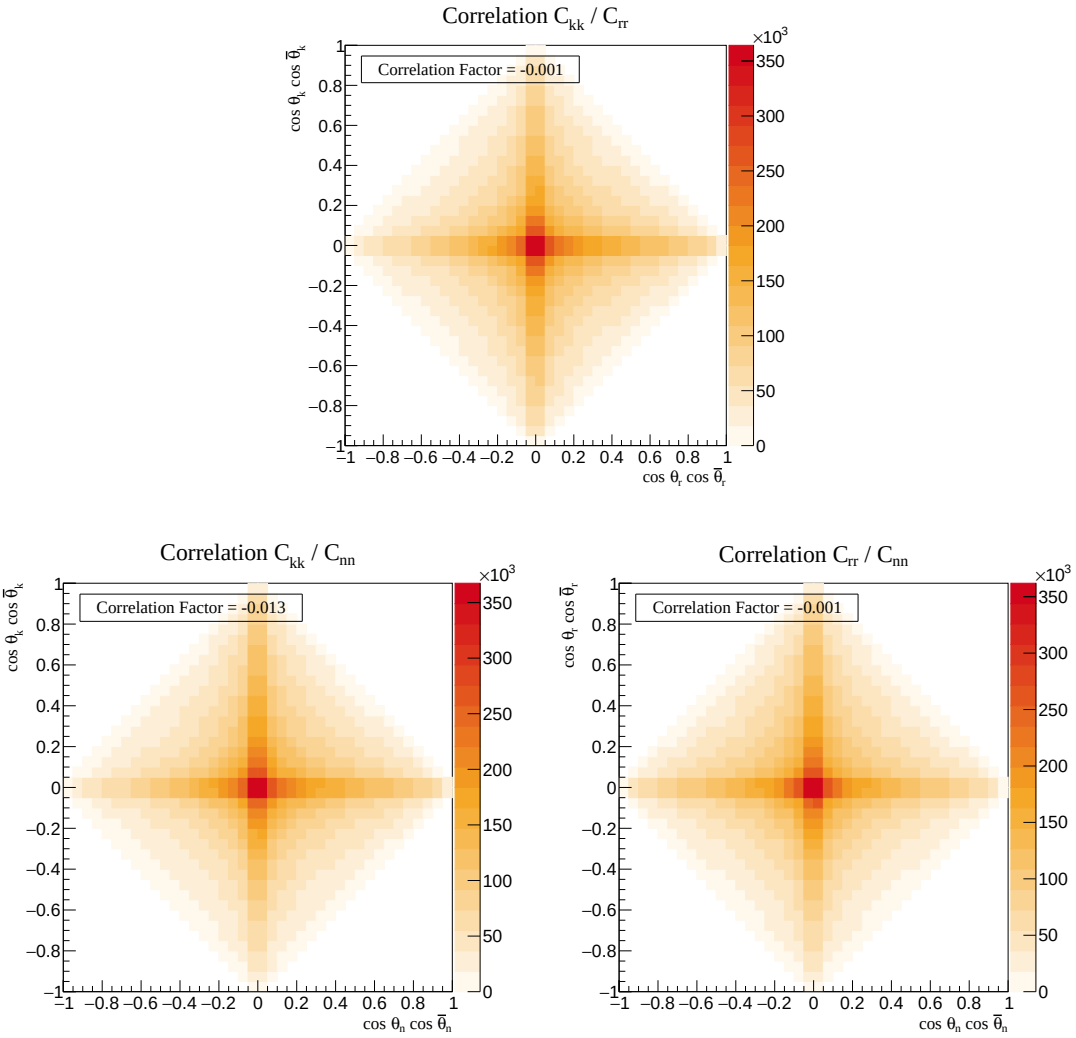

Figure 4.7: Scatter plots between $\cos\theta_i \cos\bar{\theta}_i$ and $\cos\theta_j \cos\bar{\theta}_j$, estimators for C_{ii} and C_{jj} respectively, in helicity basis. Top: $i = k$ and $j = r$, bottom left: $i = k$ and $j = n$, bottom right: $i = r$ and $j = n$. Plots use $1300\,\mathrm{fb}^{-1}$ of simulated luminosity.

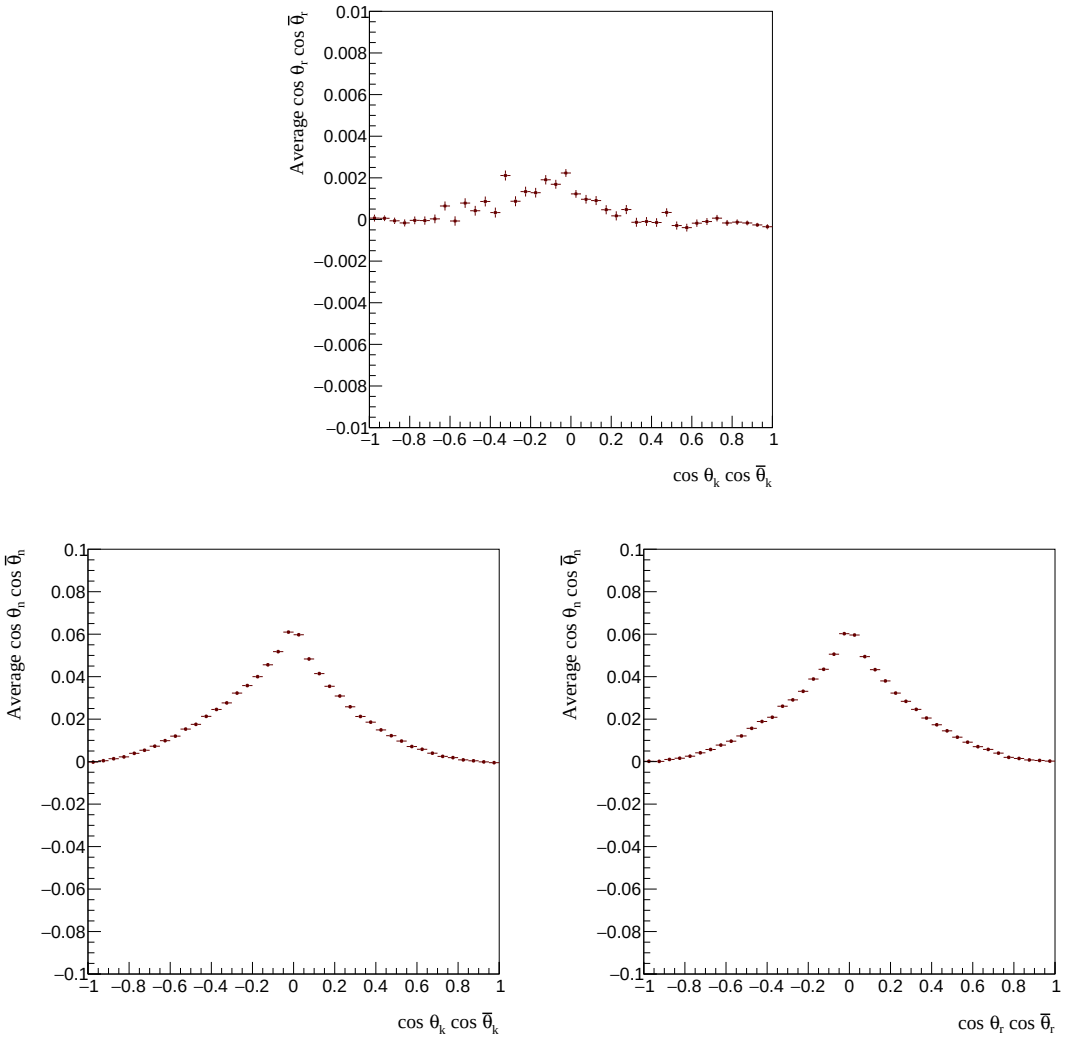

Figure 4.8: Profile along the x axis of scatter plots in Figure 4.7, evaluating correlations between C_{ii} and C_{jj} for $i \neq j$.

Chapter 5

Results at parton–level

In the previous Chapter we argued there are two $t\bar{t}$ phase space region where entanglement is expected. We now investigate each one in detail looking for entanglement and a violation of Bell inequalities.

5.1 First region: large $m_{t\bar{t}}$ and θ

The first region of $t\bar{t}$ phase space to consider in detail is the one at $m_{t\bar{t}} \gg m_t$ and $\theta \sim \frac{\pi}{2}$. In this regime both gluon fusion and $q\bar{q}$ annihilation produce an entangled spin 1 state,

$$|\psi\rangle = \frac{|\uparrow_{\hat{n}}\downarrow_{\hat{n}}\rangle + |\downarrow_{\hat{n}}\uparrow_{\hat{n}}\rangle}{\sqrt{2}}. \tag{5.1}$$

This state is a consequence of conservation of angular momentum in the massless top limit, regardless of production channel. The initial state has helicity along the beam axis, while a final state of two massless top quarks has spin aligned with their motion. If the angle of emission is $\theta = \frac{\pi}{2}$, a state like (5.1) must be reached.

Entanglement

An entanglement test in this region is given by inequality (3.7) in helicity basis,

$$\boxed{C_{kk} + C_{rr} - C_{nn} > 1,} \tag{5.2}$$

sensitive to the spin 1 state (5.1). A plot of this entanglement witness is in Figure 5.1.

Bell inequalities

We expect a measurable violation of Bell inequalities. The value of $2\sqrt{\lambda + \lambda'}$ in this region is in excess of 2.6, close to the theoretical bound of $2\sqrt{2}$ that signals perfect quantum correlation.

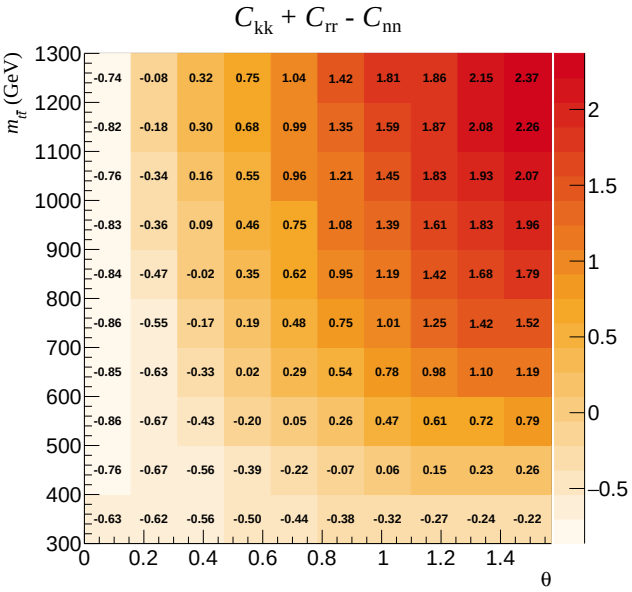

Figure 5.1: Entanglement witness (5.2), a value > 1 implies entanglement. Plot uses $1300\,\mathrm{fb}^{-1}$ of simulated luminosity, for which statistical uncertainty is negligible.

A CHSH experiment in this regime is equivalent to an experiment with two entangled photons, meaning the the optimal choice of axis should be the one found in (1.27):

$$a = (0,\, 1,\, 0), \qquad a' = (0,\, 0,\, 1), \tag{5.3}$$

$$b = (0,\, -\frac{1}{\sqrt{2}},\, \frac{1}{\sqrt{2}}), \quad b' = (0,\, \frac{1}{\sqrt{2}},\, \frac{1}{\sqrt{2}}), \tag{5.4}$$

where vectors are expressed in the helicity basis. We can confirm this prediction using generated events and equations (3.13) and (3.14). The optimal choice of axis in the region $m_{t\bar{t}} > 900\,\mathrm{GeV}$ and $\theta > 1.3$ is numerically found to be:

$$a = (0.009,\, 0.999,\, -0.036), \qquad a' = (0.007,\, 0.036,\, 0.999), \tag{5.5}$$

$$b = (-0.013,\, -0.781,\, 0.625), \qquad b' = (0.030,\, 0.749,\, 0.661), \tag{5.6}$$

thus confirming our argument. Choosing (5.3) and (5.4) as the measuring axis, the CHSH inequality can be cast in a particularly simple form:

$$\boxed{\left| -C_{rr} + C_{nn} \right| \leq \sqrt{2}.} \tag{5.7}$$

A plot of the value of (5.7) in $t\bar{t}$ phase space is in Figure 5.2. Spin correlations at high $m_{t\bar{t}}$ and θ are found in the $\hat{r}\,\hat{n}$ plane of the helicity basis. A pictorial representation of the $t\bar{t}$ pair with the $\hat{r}\,\hat{n}$ plane superimposed is in Figure 5.3, notice the striking similarity of this setup with usual EPR experiments in quantum optics.

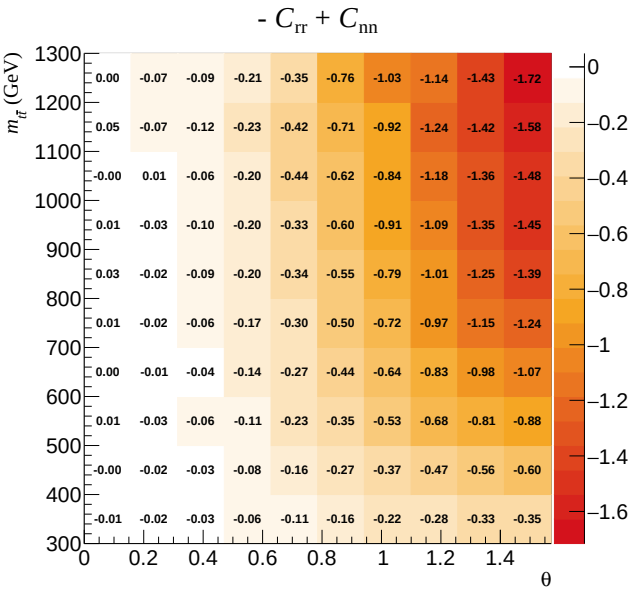

Figure 5.2: Value in the CHSH inequality (5.7), a value $> \sqrt{2}$ or $< -\sqrt{2}$ is a violation. Plot uses 1300 fb^{-1} of simulated luminosity, for which statistical uncertainty is negligible.

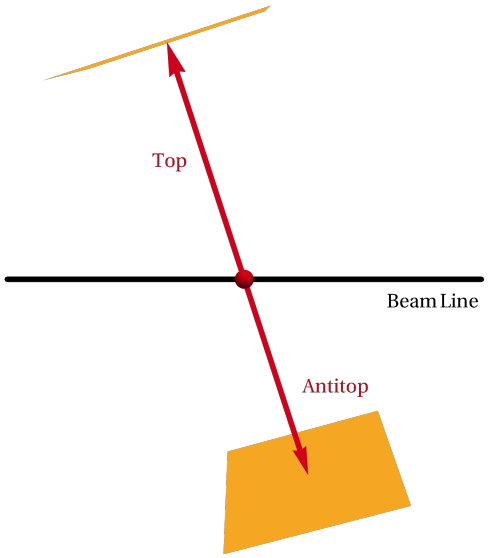

Figure 5.3: Schematic drawing of a $pp \to t\bar{t}$ event, together with the $\hat{r}\,\hat{n}$ plane in helicity basis where spin correlations are found at high $m_{t\bar{t}}$ and θ.

5.2 Second region: $t\bar{t}$ threshold

The second region of interest in $t\bar{t}$ phase space is at threshold, $m_{t\bar{t}} \sim 2m_t$. Gluon fusion produces entangled spin 0 pairs at threshold,

$$|\psi_{gg}\rangle = \frac{|\uparrow_{\hat{n}}\downarrow_{\hat{n}}\rangle - |\downarrow_{\hat{n}}\uparrow_{\hat{n}}\rangle}{\sqrt{2}}, \tag{5.8}$$

but in the same regime $q\bar{q}$ annihilation produces pairs in a separable state [3]. For instance, at $\theta = 0$ the spin density matrix for $q\bar{q} \to t\bar{t}$ is:

$$\rho_{q\bar{q}} = \frac{|\uparrow_{\hat{p}}\uparrow_{\hat{p}}\rangle\langle\uparrow_{\hat{p}}\uparrow_{\hat{p}}| + |\downarrow_{\hat{p}}\downarrow_{\hat{p}}\rangle\langle\downarrow_{\hat{p}}\downarrow_{\hat{p}}|}{2}. \tag{5.9}$$

The relative strength of the two production channels depends on collision energy, see Figure 4.2, and on kinematics, see Figure 4.4.

Entanglement

It is known [3] that $t\bar{t}$ pairs produced at threshold are entangled, and that inequality (3.6),

$$\boxed{-C_{kk} - C_{rr} - C_{nn} > 1,} \tag{5.10}$$

is sensitive to it. A plot of the entanglement witness in (5.10) is in Figure 5.4.

An interesting observable in a dilepton decay is the angle φ between leptons, with both momenta evaluated in their parent top rest frame:

$$\cos\varphi = \sum_a \cos\theta_a \cos\bar{\theta}_a. \tag{5.11}$$

Integration of (2.17) after a change of variables shows the cross section differential in $\cos\varphi$ is sensitive to $\mathrm{Tr}[C]$:

$$\frac{1}{\sigma}\frac{d\sigma}{d\cos\varphi} = \frac{1 - D\cos\varphi}{2}, \quad D = \frac{\mathrm{Tr}[C]}{3}, \tag{5.12}$$

where the minus sign comes from $\alpha\bar{\alpha} = -1$ in a dilepton final state. The expectation value is given by:

$$\langle\cos\varphi\rangle = -\frac{D}{3} = -\frac{\sum_a \langle m_a \bar{m}_a\rangle}{9}. \tag{5.13}$$

Inequality (5.10) can be directly tested using data from hadron colliders. Since $D = \mathrm{Tr}\, C/3$ is measured using (5.12) from $t\bar{t} \to \ell^+\ell^-$ decays, a sufficient condition for entanglement is:

$$D < -\frac{1}{3}. \tag{5.14}$$

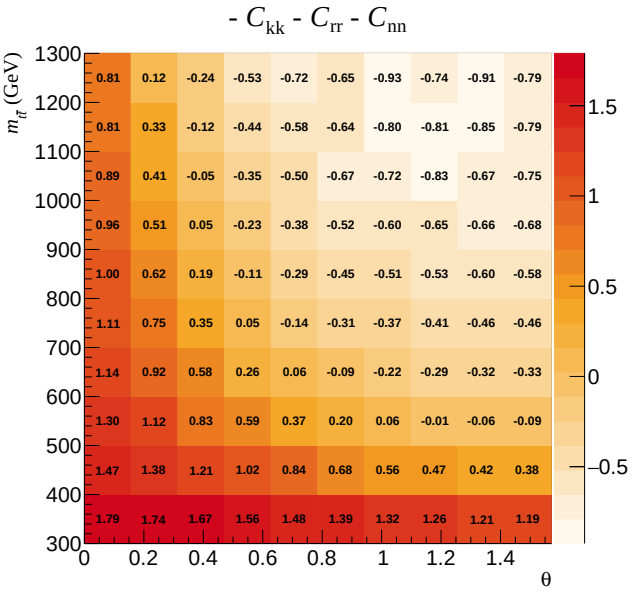

Figure 5.4: Entanglement witness (5.10), a value > 1 implies entanglement. Plot uses $1300\,\text{fb}^{-1}$ of simulated luminosity, for which statistical uncertainty is negligible.

The parameter D has been measured by the CMS Collaboration in 2019 [45] (that uses a different sign convention):

$$D_{\text{exp}} = -0.237 \pm 0.011, \tag{5.15}$$

without any cuts on $t\bar{t}$ phase space.

It is known that $t\bar{t}$ pairs produced at threshold are entangled, and it is expected that entanglement will be visible using (5.14) as a test. According to [3], restricting attention to $t\bar{t}$ pairs with $m_{t\bar{t}} < 450\,\text{GeV}$ leaves about 10^4 usable events in the LHC Run 2 dataset, and is enough to rule out the null hypothesis $D > -\frac{1}{3}$ with a large statistical significance if D can be estimated to a-few-% level accuracy. Authors note such a precision is the measurement of D is likely to be achievable.

Bell inequalities

Observing a violation of Bell inequalities at threshold is not straightforward. Fist of all, as already noted in Section 3.5, only $\lesssim 50\%$ of $t\bar{t}$ events in this region decay spacelike separated. This observation alone can already be a show–stopper for an EPR–like experiment.

For the sake of completeness, a detailed search was carried in the range $345\,\text{GeV} \leq m_{t\bar{t}} \leq 505\,\text{GeV}$, that resulted in the plot in Figure 5.5. We observe an increase in the value of $2\sqrt{\lambda + \lambda'}$ approaching threshold, with a maximum value near 2.

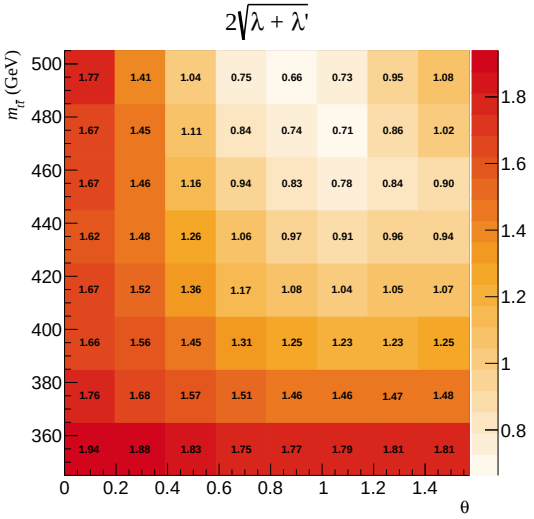

Figure 5.5: Detail near threshold of the bottom plot of Figure 4.5.

The $t\bar{t}$ pair spin state is dependent on its production channel, that at leading order can be $gg \to t\bar{t}$ or $q\bar{q} \to t\bar{t}$. To highlight the differences, in Figure 5.6 we evaluate the $2\sqrt{\lambda + \lambda'}$ test statistic from gg events only. A violation of the CHSH inequality is seen, and comparison with Figure 5.5 shows $q\bar{q}$ events act as an unwanted background. It is worth noting that, even with perfect $gg/q\bar{q}$ selection, this analysis would require reconstruction of $m_{t\bar{t}}$ with $\sim 10\,\text{GeV}$ accuracy, which is very challenging for existing experiments.

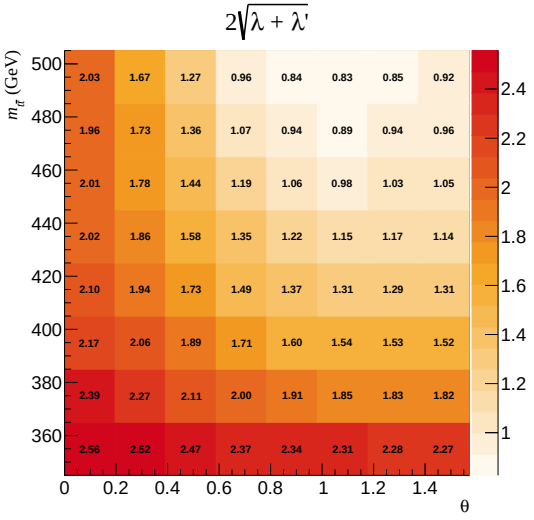

Figure 5.6: Replica of Figure 5.5 only considering events coming from a gg initial state.

Top spin correlation analysis in general, and our Bell inequality study in particular, would enjoy great benefit from the ability to discriminate the $t\bar{t}$ pair production channel. Some feasibility studies exist in the literature [55].

In proton proton collisions at $\sqrt{s} = 13\,\text{TeV}$, the fraction of gg to $q\bar{q}$ events is approximately $7:1$ at $t\bar{t}$ production threshold.

A simple handle to enhance gg events with respect to $q\bar{q}$ in pp collisions is the center of mass rapidity y_{cm}. Quarks in a proton are on average faster than antiquarks, so a $q\bar{q}$ collision is likely to feature partons with uneven velocities, thus resulting in a moving center of mass. Since the gluon parton density function is symmetric in both colliding protons, one expects an enhancement in gg events near $y_{\text{cm}} = 0$. A plot of the ratio $\sigma_{gg}/(\sigma_{gg} + \sigma_{q\bar{q}})$ in $pp \to t\bar{t}$ events as a function of the center of mass rapidity and $m_{t\bar{t}}$ is in Figure 4.4, the discussed enhancement is indeed seen at $y_{\text{cm}} \sim 0$. Unfortunately, the test statistic $2\sqrt{\lambda + \lambda'}$ does not improve substantially even with aggressive cuts, so a more involved method is needed.

Assuming one is able to identify the $t\bar{t}$ initial state and produce a pure $gg \to t\bar{t}$ sample, the experiment becomes equivalent to the prototype of Chapter 1, with two entangled spin $1/2$ particles in a spin 0 state. The optimal choice of axis a, a', b, b' along which to measure spin is similar to the one in (1.27):

$$a = (1,\, 0,\, 0), \qquad a' = (0,\, 0,\, -1), \tag{5.16}$$

$$b = (-\frac{1}{\sqrt{2}},\, 0,\, \frac{1}{\sqrt{2}}), \quad b' = (\frac{1}{\sqrt{2}},\, 0,\, \frac{1}{\sqrt{2}}). \tag{5.17}$$

Of course a spin 0 state is rotation invariant, so any rigid rotation of (5.16) and (5.17) is equally valid. The optimal choice of axis in the region $m_{t\bar{t}} < 360\,\text{GeV}$ only using $gg \to t\bar{t}$ events is numerically found to be:

$$a = (1.000,\, 0.007,\, 0.009), \qquad a' = (0.008,\, 0.021,\, -1.000), \tag{5.18}$$

$$b = (-0.725,\, -0.015,\, 0.689), \quad b' = (0.712,\, -0.010,\, 0.702), \tag{5.19}$$

where vectors are expressed in the helicity basis. Choosing (5.16) and (5.17) as the measuring axis, the CHSH inequality can be written as:

$$\boxed{\left|C_{kk} + C_{nn}\right| \leq \sqrt{2}.} \tag{5.20}$$

A plot of the value of (5.20) is in Figure 5.7. Spin correlations at threshold are mostly found in the helicity basis $\hat{k}\,\hat{n}$ plane. A drawing of the $t\bar{t}$ pair production event with the $\hat{k}\,\hat{n}$ plane superimposed is in Figure 5.8.

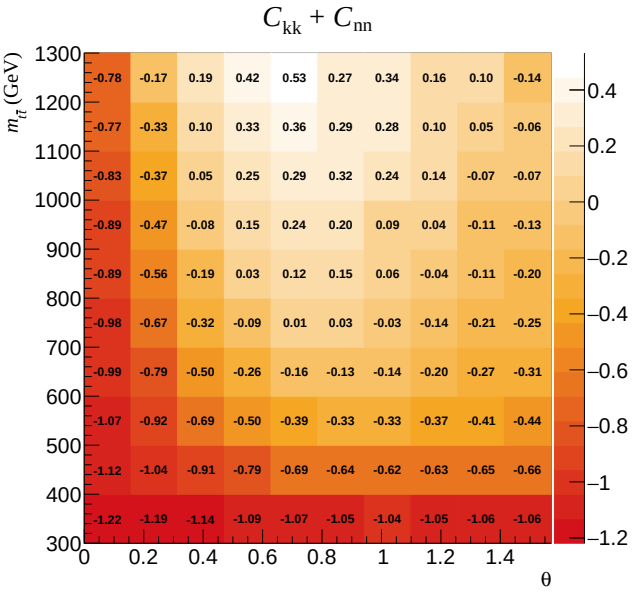

Figure 5.7: Value in the CHSH inequality (5.20), a value $> \sqrt{2}$ or $< -\sqrt{2}$ is a violation. Plot uses 1300 fb^{-1} of simulated luminosity, for which statistical uncertainty is negligible.

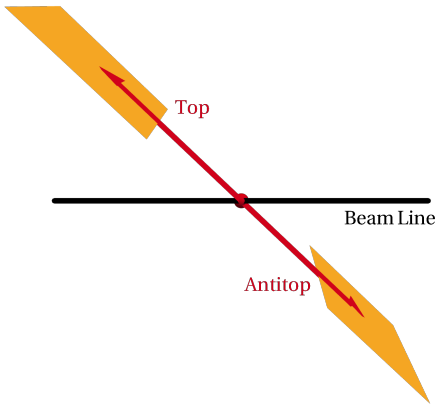

Figure 5.8: Schematic drawing of a $pp \to t\bar{t}$ event, with the $\hat{k}\,\hat{n}$ plane in helicity basis where spin correlations are found at threshold.

Chapter 6

Reconstruction–level analysis

6.1 Event generation

We perform the data analysis described in Section 4.4 using $1300\,\mathrm{fb}^{-1}$ of

$$pp \to \ell^- \ell^+ \nu \bar{\nu} b \bar{b}, \tag{6.1}$$

events, generated at the parton level, then showered, and reconstructed inside a general purpose particle detector.

Events were generated using MadGraph5_aMC at leading order as described in Section 4.1. Hard processes coming from event generators such as MadGraph have to be hadronized and showered, it is only after this step that realistic events are available, as they could be observed in a detector. Showers are almost completely nonperturbative, and require extensive modelling and tuning based in part or in full on parametrisations of experimental data.

Our tool of choice for showering is Pythia 8 [56]. Pythia is a program for the generation of high energy collision events, including parton showers, fragmentation, and the decay of unstable particles. MadGraph is capable of automatically steering to Pythia the showering of previously generated hard events. The specifics of parton showering and hadronization as modeled by Pythia are technical, and can be found in [56] and in references therein.

Events are reconstructed inside the ATLAS detector of the Large Hadron Collider [57]. ATLAS is the largest general–purpose particle detector at the LHC. It consists of an inner tracking detector, electromagnetic and hadronic calorimeters, and a muon spectrometer. The inner detector is immersed in a 2 T magnetic field and provides charged particle tracking for $|\eta| < 2.5$. The calorimeter system covers the range $|\eta| < 4.9$, hadronic calorimetry is segmented into barrel structures within $|\eta| < 1.7$. The muon spectrometer comprises high-precision tracking chambers measuring the deflection of muons in a magnetic field generated by superconducting toroid magnets. The field integral of the toroids ranges from 2 to 6 T m across the detector. Interesting events are selected by the first-level trigger system implemented in custom hardware, followed by

selections made by algorithms implemented in software in the high–level trigger (HLT). Events accepted by the HLT are subsequently reconstructed offline.

The ATLAS detector is simulated within the Delphes framework [58]. Delphes performs a multipurpose detector response simulation, that we tune to match the characteristics of the ATLAS experiment. The simulation includes a tracking system embedded into a magnetic field, calorimeters, and a muon system. The framework is interfaced to Pythia and outputs observables including leptons, missing transverse energy, and jets.

Leptons have some p_T and η–dependent probability of being reconstructed, and their final momentum is obtained as a Gaussian smearing of the true value. The missing transverse energy is assessed from the transverse component of the total energy deposited in the detector. Jets are the result of clustering the particle-flow tracks; within Delphes, the user has the freedom to choose the jet clustering algorithm. In our analysis hadron jets are handled by the FastJet package using the anti-k_t algorithm [59] [60]. The jet b–tagging algorithm can be specified. The performance of our simulated b–tagging algorithm follows the one in [61] expected from the ATLAS detector during Run 2 of the LHC.

The final Delphes output is stored in a ROOT TTree. On a typical single–core machine, one run with 10^5 simulated events requires around one hour to shower and reconstruct inside the simulated ATLAS detector and occupies ∼150 MB of disk space.

6.2 Event selection

We require exactly two leptons of opposite charge, both with $p_T > 25\,\text{GeV}$ and $|\eta| < 2.47$. Both leptons must pass an isolation requirement, the *isolation* of particle P is defined by:

$$I(P) = \frac{\sum p_T(i)}{p_T(P)}, \tag{6.2}$$

where the sum is over all particles that lie in a cone of radius $\Delta R = \sqrt{(\Delta\eta)^2 + (\Delta\phi)^2}$ around the particle P, not counting P. Values $I \approx 0$ indicate the particle is isolated. We take $\Delta R = 0.5$ and require leptons to have $I \leq 0.15$.

In the e^+e^- and $\mu^+\mu^-$ channels, Z + jets processes are suppressed by requiring $p_T^{\text{miss}} > 40\text{GeV}$ and $20\,\text{GeV} < m_{\ell^+\ell^-} < 76\,\text{GeV}$ or $m_{\ell^+\ell^-} > 106\,\text{GeV}$.

We require the presence of two jets with $p_T > 25\,\text{GeV}$ and $|\eta| < 2.5$. At least one jet has to be b–tagged. If only one jet has been b–tagged, we assume the second b-jet is the one not b–tagged with largest p_T.

6.3 Neutrino reconstruction

The correlations we want to measure require careful reconstruction of the $t\bar{t}$ pair. We employ an algorithm partially based on the one used by the CMS Collaboration in recent top spin correlation papers [44, 45].

Charged leptons are reconstructed directly, and b quarks are reconstructed from the b-tagged jets. Neutrinos are then reconstructed solving for the kinematics of a $t\bar{t} \to \ell^- \ell^+ \nu \bar{\nu} b \bar{b}$ event,

$$\begin{cases} p_x^{\text{miss}} = p_{x\,\nu} + p_{x\,\bar{\nu}} \\ p_y^{\text{miss}} = p_{y\,\nu} + p_{y\,\bar{\nu}} \\ p_\nu^2 = 0 \\ p_{\bar{\nu}}^2 = 0 \\ (p_{\ell^+} + p_\nu)^2 = m_{W^+}^2 \\ (p_{\ell^-} + p_{\bar{\nu}})^2 = m_{W^-}^2 \\ (p_{\ell^+} + p_\nu + p_b)^2 = m_t^2 \\ (p_{\ell^-} + p_{\bar{\nu}} + p_{\bar{b}})^2 = m_{\bar{t}}^2, \end{cases} \tag{6.3}$$

where we have denoted p^{miss} the missing momenta transverse to the beam, that we take to be in the z direction.

Before reconstructing the event, the measured p_b, $p_{\bar{b}}$, and p^{miss} are smeared randomly according to the simulated distribution of reconstructed values around true values. In practice, this means a gaussian smearing with $\sigma \sim 20\,\text{GeV}$ in each component of $\vec{p}_b$ and $\vec{p}_{\bar{b}}$, and in the x and y components of p^{miss}. Lepton momenta are not smeared since their reconstruction is very accurate. The W boson masses m_{W^+} and m_{W^-} are smeared according to a Breit–Wigner distribution centered in $m_W = 80.4\,\text{GeV}$ with width $\Gamma_W = 2.1\,\text{GeV}$.

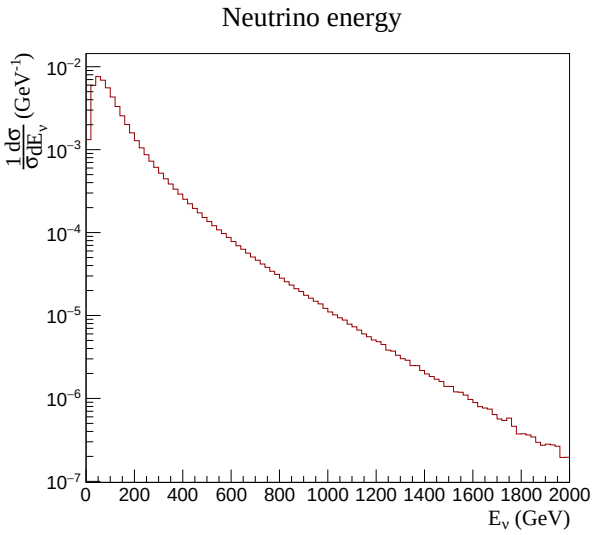

Figure 6.1: Distribution of the neutrino energy used in the weighting function (6.4). The distribution is evaluated using $1300\,\text{fb}^{-1}$ of simulated $t\bar{t} \to \ell^- \ell^+ \nu \bar{\nu} b \bar{b}$ events.

System (6.3) can be solved analytically, see Appendix A. The solution is assigned a weight:

$$w = f(E_\nu), \tag{6.4}$$

where $f(x)$ indicates the normalized probability distribution of x evaluated at parton level, a plot is in Figure 6.1. System (6.3) can have multiple solutions, in this case all solutions are assigned weights and considered in the following.

Several combinations of kinematic variables have been considered for the weighting function. To avoid introducing bias in our spin correlation analysis, only rotation invariant variables such as energy or total momentum were tested. The choice in (6.4) is the one yielding the most satisfactory result for our purposes. Only one neutrino is considered, under the rationale that once the first neutrino has been identified, the second one is fixed by kinematic constraints. If solutions are not weighted, that is $w = 1$, the neutrino and antineutrino energy is systematically overestimated by a significant amount. This is not a problem if global distributions are evaluated and subsequently unfolded, however this analysis requires to identify $m_{t\bar{t}}$ and θ on a event-by-event basis to decide if a given $t\bar{t}$ pair does or does not fall into the signal region.

The smearing on b quarks and p^{miss} is repeated $N_{\text{smear}} = 100$ times. There is a twofold ambiguity in assigning b quarks to b–tagged jets, so reconstruction is performed twice for each event. The assignment yielding the largest sum of weights over the N_{smear} trials is chosen, and the final p_ν and $p_{\bar{\nu}}$ are calculated as a weighted average. If no valid solution for the kinematics is ever found during the N_{smear} trials, the event is discarded.

6.4 Expected number of events

The combination of cuts described above together with our neutrino reconstruction algorithm accepts 11% of events at parton level. Signal purity, defined as the fraction of accepted events that contain a $t\bar{t}$ pair, is about 92%. Background contamination is reduced in the final event sample with respect to all events at parton level since non $t\bar{t}$ events are less likely to produce valid solutions for the $t\bar{t}$ decay kinematics. Our estimation of purity is optimistic since background not coming from a $b\,\bar{b}\,\ell^+\,\ell^- + E^{\text{miss}}$ final state is not included in this analysis.

A summary of our expected event yield with LHC Run 3 luminosity is in Table 6.1. These numbers are not far from those quoted from the ATLAS and CMS Collaborations in recent top spin correlation measurements [42, 45]. To assess more accurately the behavior of our cuts when applied to hard events of the form $pp \to \ell^-\,\ell^+\,\nu\,\bar{\nu}\,b\,\bar{b}$, Table 6.2 shows the expected number of events as the cuts described in Section 6.2 are applied in succession.

	Events at parton level	Events reconstructed
All $\ell^- \ell^+ p^{\text{miss}} b\bar{b}$	20 000 000	2 276 075
$t\bar{t} \to \ell^- \ell^+ \nu \bar{\nu} b\bar{b}$	17 892 163 (90%)	2 091 430 (92%)
Background	2 107 837 (10%)	184 645 (8%)

Table 6.1: Approximate event yield from a luminosity of $450\,\text{fb}^{-1}$ at parton level and after full event reconstruction. The relative fraction of signal and background is indicated in parenthesis.

	Number of events
All events at parton level	20 000 000
Exactly two leptons	7 532 063 (38%)
Leptons of opposite charge	7 527 055 (38%)
Leptons with $p_T > 25\,\text{GeV}$, $\lvert\eta\rvert < 2.47$, and isolated	4 940 210 (25%)
Different flavor / same flavor passing $m_{\ell^+\ell^-}$ and p_T^{miss} cuts	3 880 033 (20%)
At least two jets	3 532 110 (18%)
At least two jets with $p_T > 25\,\text{GeV}$, $\lvert\eta\rvert < 2.5$	3 139 256 (16%)
At least one jet b–tagged	2 645 234 (13%)
Neutrinos reconstructed successfully	2 276 075 (11%)

Table 6.2: Approximate number of events from a luminosity of $450\,\text{fb}^{-1}$ starting from parton level and applying in order the cuts of Section 6.2. In parenthesis we denote the relative fraction of events that survives at each stage.

Chapter 7

Performance of event reconstruction

7.1 Reconstruction of kinematics

The performance of our event reconstruction algorithm is summarized in the following Figures. In Figure 7.1 the reconstructed lepton momenta are compared to their true value. Figures 7.2, 7.3, and 7.4 show similar plots for bottom quarks, neutrinos, and top quarks. Reconstruction of the total center of mass momentum p_{cm} and the $t\bar{t}$ pair kinematical variables $m_{t\bar{t}}$ and θ is in Figure 7.5.

Observables $\cos\theta_i$ and $\cos\bar{\theta}_j$, representing the lepton direction evaluated in their parent top quark reference frame are compared to their true values in Figure 7.6. Figure 7.7 compares true and reconstructed values of $\cos\theta_i \cos\bar{\theta}_j$ for $i, j = 1, 2, 3$ in helicity basis, used to reconstruct the ij entry of the C matrix.

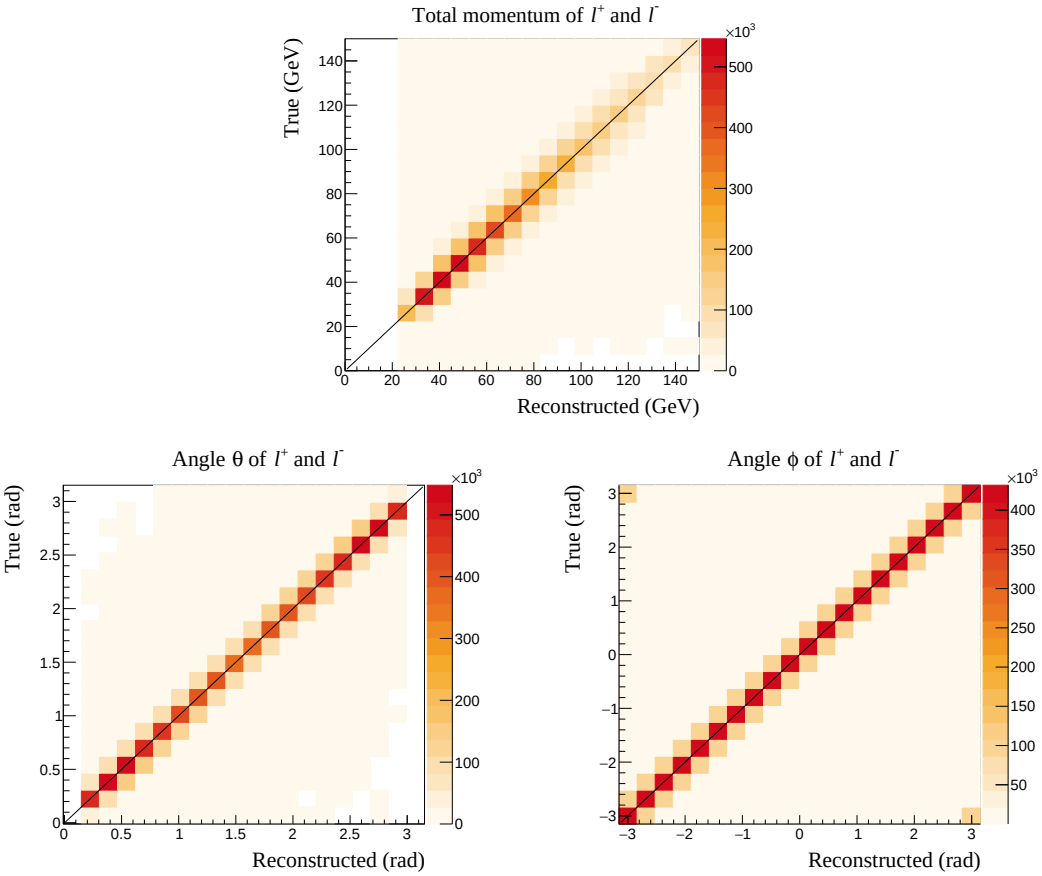

Figure 7.1: Comparison between true and reconstructed momenta for leptons. We use spherical coordinates r, θ, ϕ with the beam on the z axis. Plots use $1300\,\mathrm{fb}^{-1}$ of simulated luminosity.

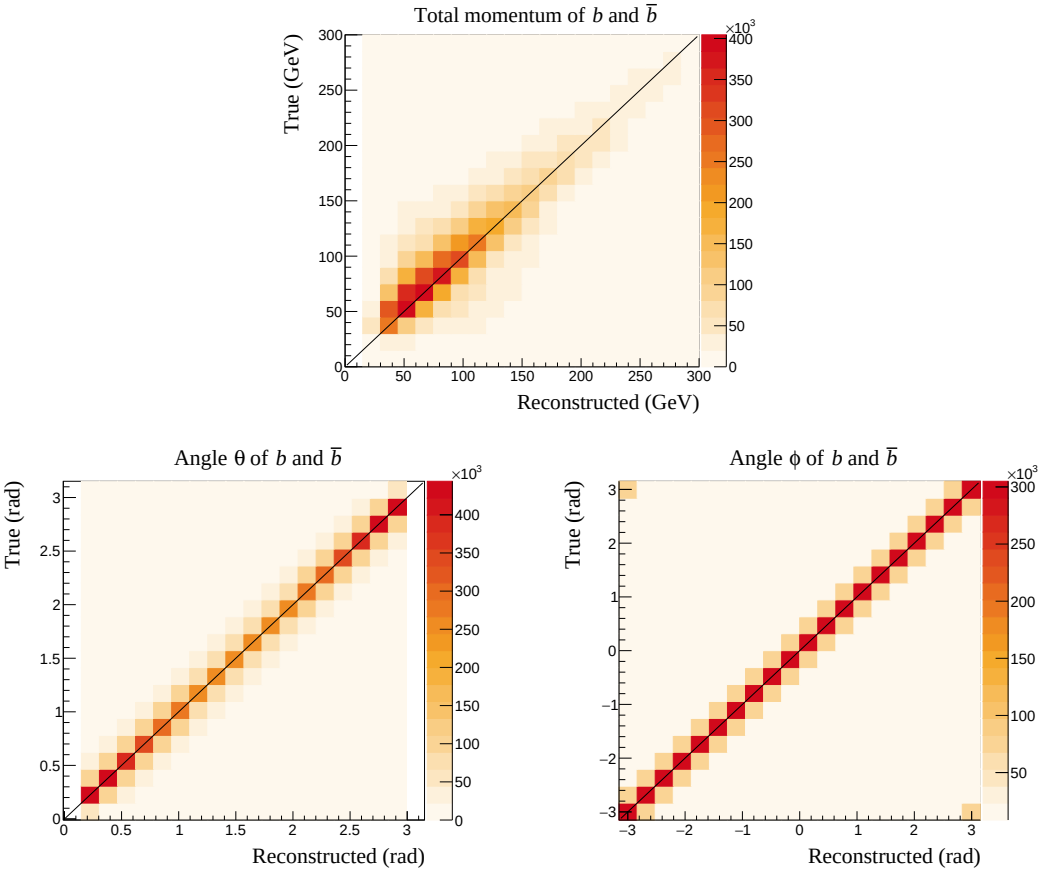

Figure 7.2: Comparison between true and reconstructed momenta for bottom quarks. The parton–jet pairing is the one given by the neutrino reconstruction algorithm. We use spherical coordinates r, θ, ϕ with the beam on the z axis. Plots use $1300\,\mathrm{fb}^{-1}$ of simulated luminosity.

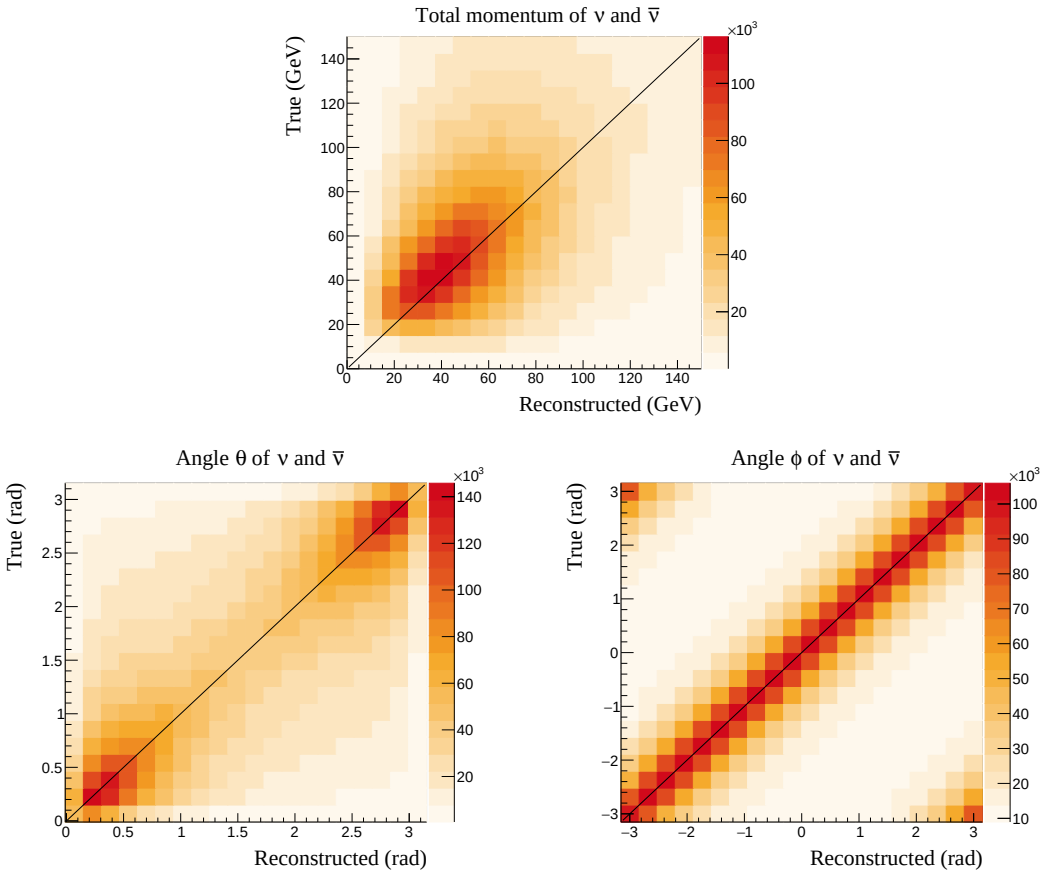

Figure 7.3: Comparison between true and reconstructed momenta for neutrinos. We use spherical coordinates r, θ, ϕ with the beam on the z axis. Plots use $1300\,\mathrm{fb}^{-1}$ of simulated luminosity.

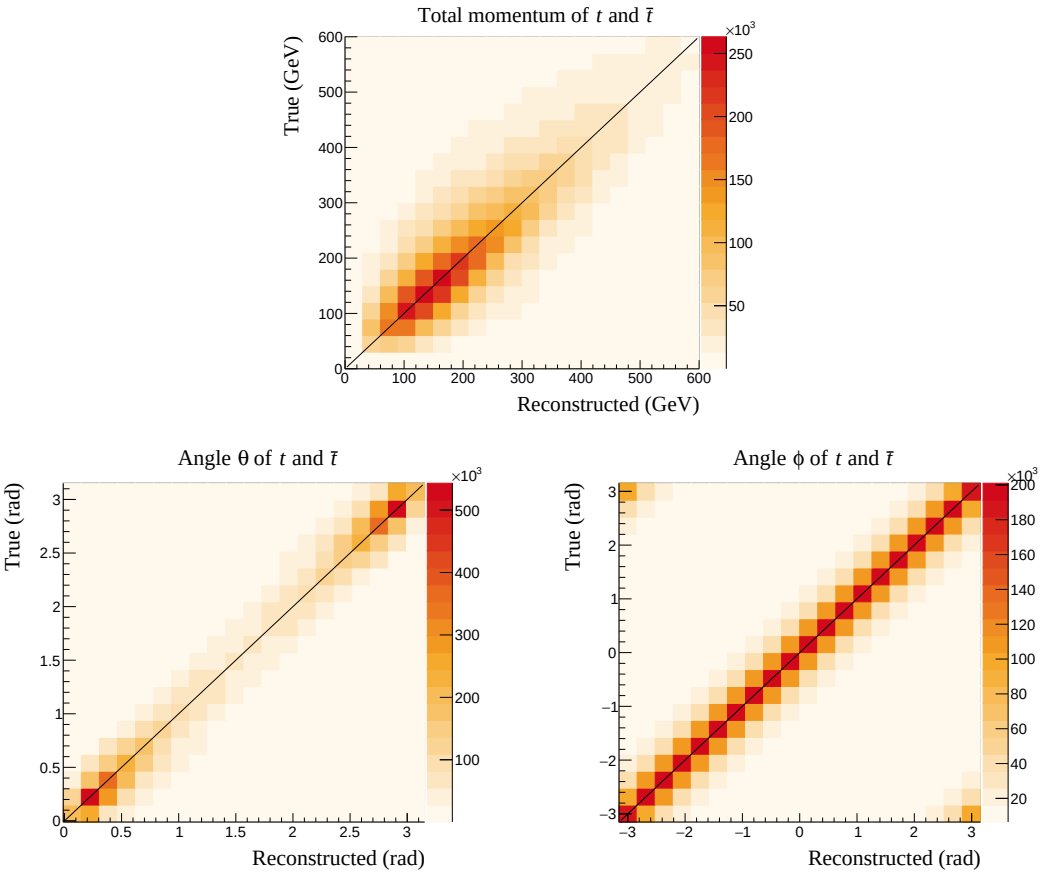

Figure 7.4: Comparison between true and reconstructed momenta for top quarks. We use spherical coordinates r, θ, ϕ with the beam on the z axis. Plots use $1300\,\mathrm{fb}^{-1}$ of simulated luminosity.

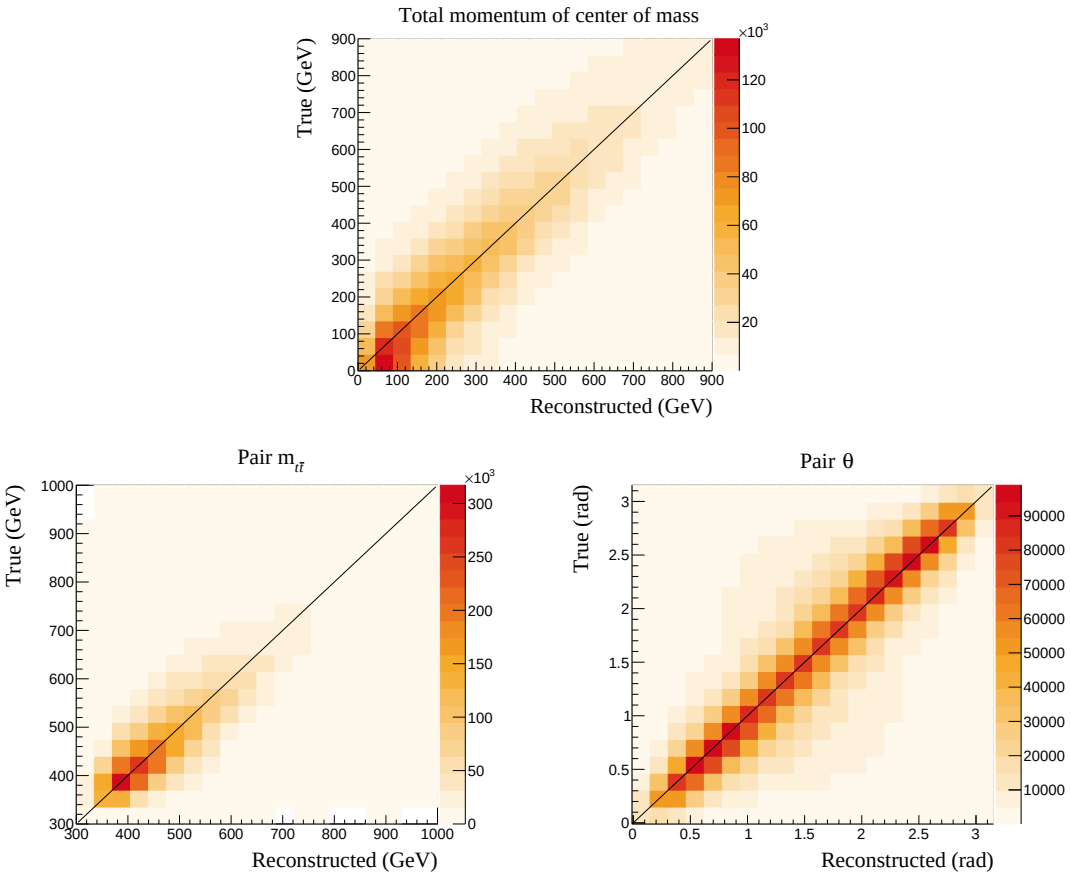

Figure 7.5: Comparison between true and reconstructed $t\bar{t}$ pair kinematic variables. Top: center of mass total momentum. Bottom left: $m_{t\bar{t}}$, bottom right: θ in the center of mass frame. Plots use 1300 fb^{-1} of simulated luminosity.

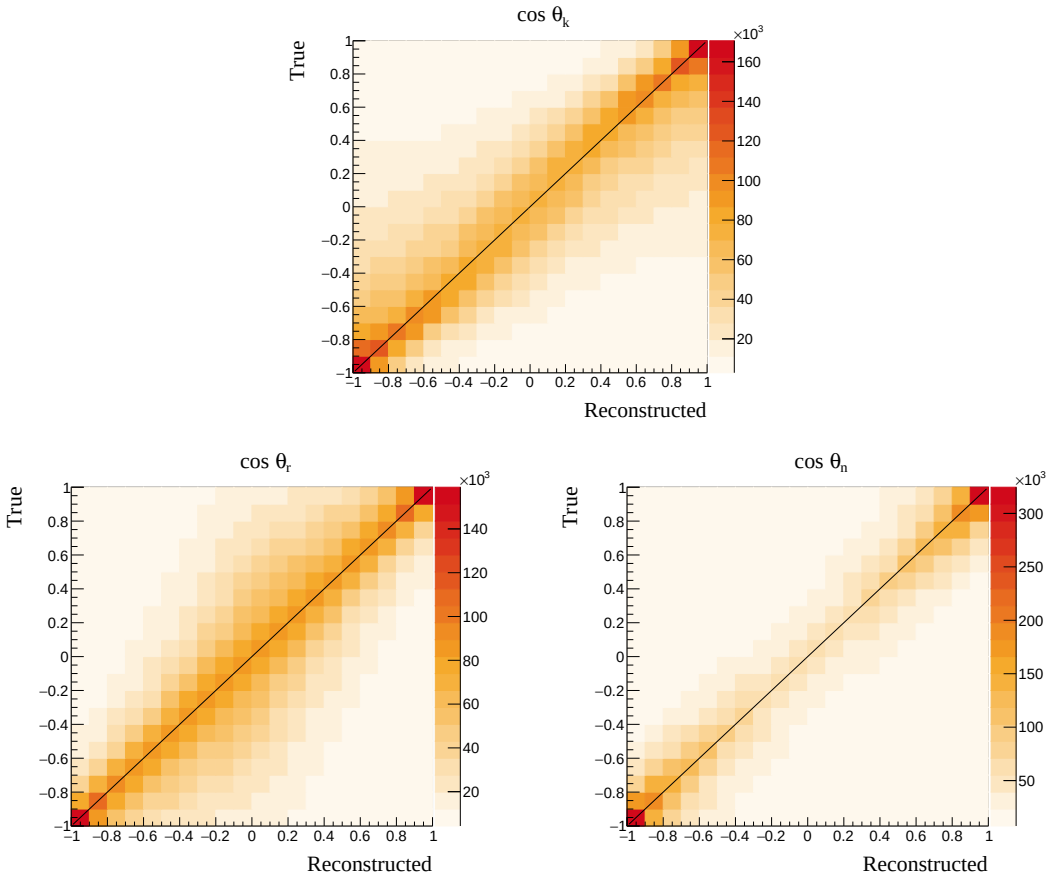

Figure 7.6: Comparison between true and reconstructed lepton direction in the top quark reference frame in helicity basis. Plots use 1300 fb^{-1} of simulated luminosity and cover the whole $t\bar{t}$ phase space without kinematic cuts.

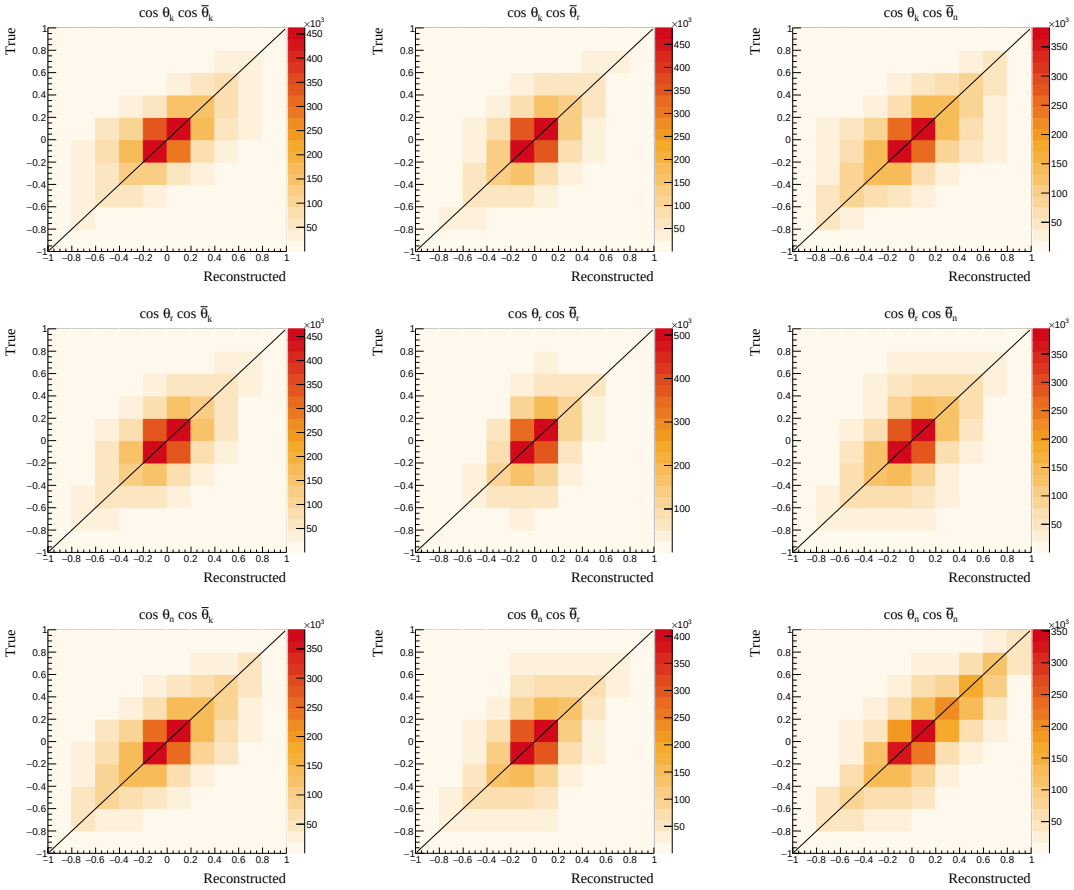

Figure 7.7: Comparison between true and reconstructed value of $\cos\theta_i \cos\bar{\theta}_j$ in helicity basis, $i, j = k, r, n$. Plots use 1300 fb^{-1} of simulated luminosity and cover the whole $t\bar{t}$ phase space without kinematic cuts.

7.2 Unfolding

The reconstructed distributions of $\cos\theta_i \cos\bar{\theta}_j$ are compared to their true values in Figure 7.8. Various detector effects and biases introduced during event reconstruction alter the distributions used to estimate entries of the C matrix. These effects have to be accounted for by unfolding the reconstructed distributions of $\cos\theta_i \cos\bar{\theta}_j$.

Unfolding is the process of inferring the true distribution of a quantity from the observed one, that is to correct the observed spectrum for distortion and noise. The algorithm is trained using 2/3 of the generated dataset ($\approx 850\,\text{fb}^{-1}$). The analysis is subsequently run on the remaining 1/3 ($\approx 450\,\text{fb}^{-1}$), equivalent to the expected luminosity available after Run 3 of the LHC.

Training consists of a comparison between true and reconstructed values. This includes events that were not reconstructed but did contain a $t\bar{t}$ pair with $m_{t\bar{t}}$ and θ inside the signal region of phase space (counted as Miss), and events that were reconstructed but did not contain a $t\bar{t}$ pair at all, or did contain one but not in the signal region of phase space (counted as Fake).

A naive implementation of unfolding likely leads to dramatic numerical instabilities. Various algorithms exist in the literature, we choose the iterative Bayesian method proposed by D'Agostini [62]. Unfolding was performed with the RooUnfold framework [63]. Distributions are unfolded iteratively for $n = 20$ times, final distributions are found to be regular and stable under further iterations of the same method.

7.3 Performance of unfolding

As a benchmark to test unfolding performance, we measure entries of the C matrix in helicity basis without phase space cuts. In Figure 7.9 we show the distributions of $\cos\theta_i \cos\bar{\theta}_j$ after unfolding, compared to their true values as in Figure 7.8. Numerical results are in Table 7.1, that also shows a recent measurement of C from the CMS Collaboration [45]. The performance of unfolding is satisfactory, and all reconstructed values are made compatible to their true values within statistical uncertainty. Both estimation methods for C_{ij}, namely the fit of (2.19) and the expectation value relation (2.20), provide similar results.

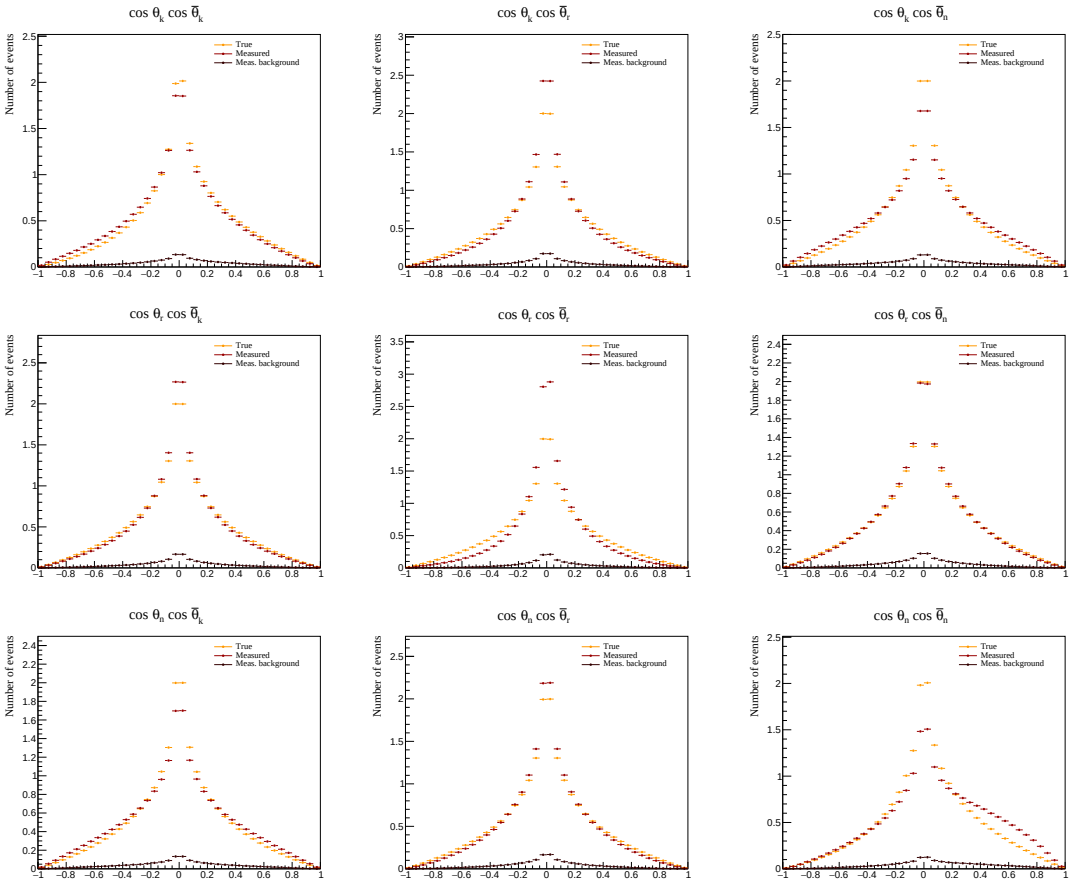

Figure 7.8: Comparison between reconstructed and parton level distribution of $\cos\theta_i \cos\bar{\theta}_j$ in helicity basis, $i, j = k, r, n$. Plots use 1300 fb^{-1} of simulated luminosity and cover the whole $t\bar{t}$ phase space without kinematic cuts.

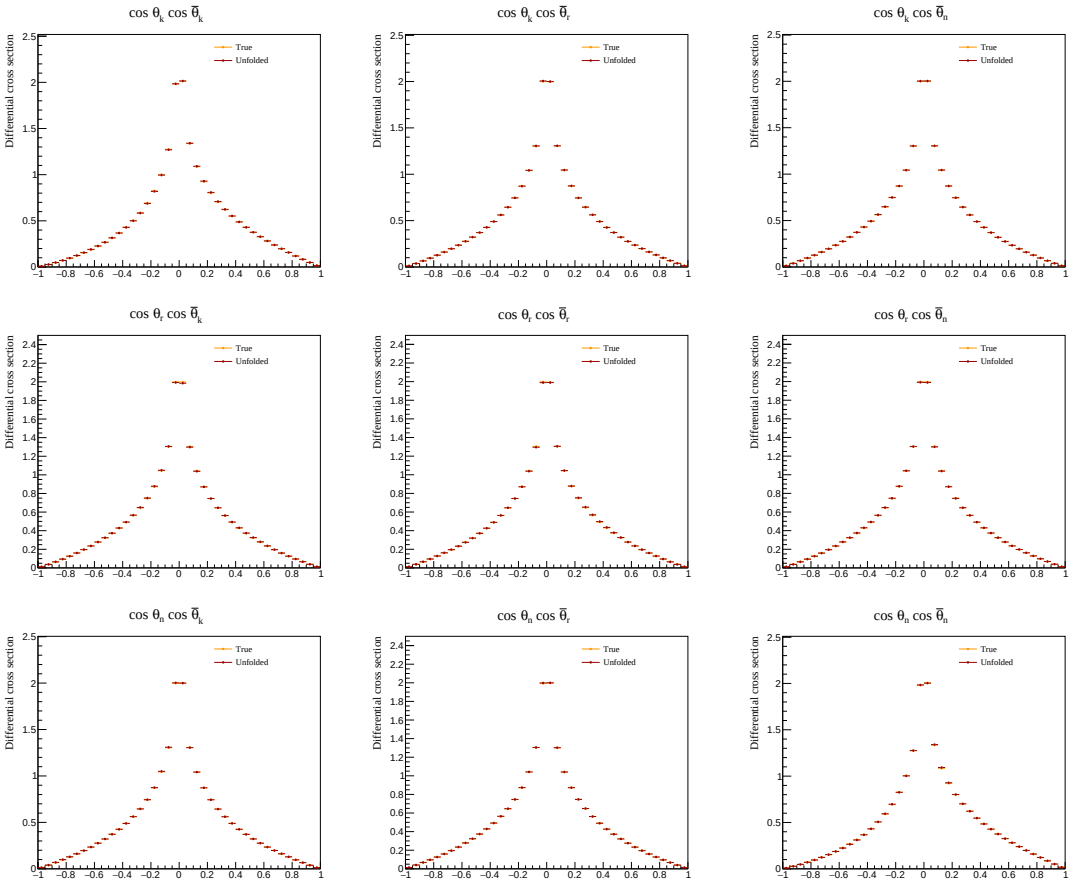

Figure 7.9: Comparison between unfolded and parton level distribution of $\cos\theta_i \cos\bar{\theta}_j$ in helicity basis, $i, j = k, r, n$. Plots use 1300 fb^{-1} of simulated luminosity and cover the whole $t\bar{t}$ phase space without kinematic cuts.

Entry	True value	Reconstructed (Fit)	Reconstructed (Avg.)	Experiment [45]
C_{kk}	-0.324	-0.322 ± 0.003	-0.322 ± 0.002	-0.300 ± 0.038
C_{kr}	0.000	-0.008 ± 0.003	-0.008 ± 0.002	
C_{kn}	0.001	0.005 ± 0.002	0.005 ± 0.002	
C_{rk}	0.001	0.000 ± 0.003	0.000 ± 0.002	
C_{rr}	-0.008	-0.009 ± 0.003	-0.009 ± 0.002	-0.081 ± 0.032
C_{rn}	-0.002	-0.007 ± 0.002	-0.007 ± 0.002	
C_{nk}	0.001	0.004 ± 0.002	0.004 ± 0.002	
C_{nr}	-0.001	0.004 ± 0.002	0.004 ± 0.002	
C_{nn}	-0.319	-0.324 ± 0.002	-0.324 ± 0.003	-0.329 ± 0.020

Table 7.1: Results for entries of the C matrix in helicity basis without $t\bar{t}$ phase space cuts. True values come from $1300\,\mathrm{fb}^{-1}$ of simulated luminosity at Leading Order. Reconstructed values follow from our analysis, and are obtained using the expectation value relation (2.20) and the fit of (2.19). Uncertainty is statistical only and is scaled to a luminosity of $450\,\mathrm{fb}^{-1}$, equivalent to the expected yield of Run 2 + Run 3 of the LHC.

Remark. Ref. [45] redefines the helicity basis according to the sign of $\cos\theta$,

$$\{\hat{k}, \hat{r}, \hat{n}\} \to \{\hat{k},\, \mathrm{sign}(\cos\theta)\,\hat{r},\, \mathrm{sign}(\cos\theta)\,\hat{n}\}. \tag{7.1}$$

This different choice makes the coefficients C_{kr} and C_{rk} different from zero. Entries on the diagonal are left invariant, and can be compared with our analysis.

Chapter 8

Results

8.1 Entanglement

In order to measure the presence of entanglement we run the analysis with three different prescriptions for $t\bar{t}$ phase space cuts. The figure of merit we try to maximize is the statistical significance for the observation of entanglement (not the numerical value of the entanglement markers (5.2) and (5.10), that is essentially meaningless *per se*).

The first cut prescription, henceforth *weak cuts*, is to include all regions of phase space where entanglement is expected at parton level, i.e. bins with a value larger than 1 in Figures 5.1 and 5.4. The second prescription is stronger, henceforth *intermediate cuts*, and amounts to only including regions with a value larger than 1.1 in the same Figures. The third prescription is the strongest, denoted *strong cuts*, and only considers bins with a numerical value larger than 1.2.

Our choice of cuts explicitly amounts to:

- *Weak cuts.*
  At high $m_{t\bar{t}}$ and θ using (5.2), any of the following conditions have to hold:

$$\begin{cases} m_{t\bar{t}} > 600\,\text{GeV}\ , & \dfrac{2\theta}{\pi} > 0.8 \\ m_{t\bar{t}} > 700\,\text{GeV}\ , & \dfrac{2\theta}{\pi} > 0.6 \\ m_{t\bar{t}} > 900\,\text{GeV}\ , & \dfrac{2\theta}{\pi} > 0.5 \\ m_{t\bar{t}} > 1200\,\text{GeV}\ , & \dfrac{2\theta}{\pi} > 0.4. \end{cases} \tag{8.1}$$

  These cuts cover 4.5% of the total $pp \to t\bar{t}$ cross section.

At threshold using (5.10), any of the following:

$$\begin{cases} m_{t\bar{t}} < 400\,\text{GeV} \\ m_{t\bar{t}} < 500\,\text{GeV}\ ,\ \dfrac{2\theta}{\pi} < 0.4 \\ m_{t\bar{t}} < 600\,\text{GeV}\ ,\ \dfrac{2\theta}{\pi} < 0.2 \\ m_{t\bar{t}} < 900\,\text{GeV}\ ,\ \dfrac{2\theta}{\pi} < 0.1. \end{cases} \tag{8.2}$$

These cuts cover 34% of the total cross section.

- *Intermediate cuts.*
  At high $m_{t\bar{t}}$ and θ:

$$\begin{cases} m_{t\bar{t}} > 600\,\text{GeV}\ ,\ \dfrac{2\theta}{\pi} > 0.8 \\ m_{t\bar{t}} > 700\,\text{GeV}\ ,\ \dfrac{2\theta}{\pi} > 0.7 \\ m_{t\bar{t}} > 800\,\text{GeV}\ ,\ \dfrac{2\theta}{\pi} > 0.6 \\ m_{t\bar{t}} > 1000\,\text{GeV}\ ,\ \dfrac{2\theta}{\pi} > 0.5. \end{cases} \tag{8.3}$$

  These cuts cover 3.5% of the total cross section.

  At threshold:

$$\begin{cases} m_{t\bar{t}} < 400\,\text{GeV} \\ m_{t\bar{t}} < 500\,\text{GeV}\ ,\ \dfrac{2\theta}{\pi} < 0.3 \\ m_{t\bar{t}} < 600\,\text{GeV}\ ,\ \dfrac{2\theta}{\pi} < 0.2 \\ m_{t\bar{t}} < 800\,\text{GeV}\ ,\ \dfrac{2\theta}{\pi} < 0.1. \end{cases} \tag{8.4}$$

  These cuts cover 30% of the total cross section.

- *Strong cuts.*
  At high $m_{t\bar{t}}$ and θ:

$$\begin{cases} m_{t\bar{t}} > 700\,\text{GeV}\ ,\ \dfrac{2\theta}{\pi} > 0.7 \\ m_{t\bar{t}} > 900\,\text{GeV}\ ,\ \dfrac{2\theta}{\pi} > 0.6 \\ m_{t\bar{t}} > 1000\,\text{GeV}\ ,\ \dfrac{2\theta}{\pi} > 0.5. \end{cases} \tag{8.5}$$

  These cuts cover 2.3% of the total cross section.

At threshold:

$$\begin{cases} m_{t\bar{t}} < 400\,\text{GeV}\ , & \dfrac{2\theta}{\pi} < 0.9 \\ m_{t\bar{t}} < 500\,\text{GeV}\ , & \dfrac{2\theta}{\pi} < 0.3 \\ m_{t\bar{t}} < 600\,\text{GeV}\ , & \dfrac{2\theta}{\pi} < 0.1. \end{cases} \tag{8.6}$$

These cuts cover 24% of the total cross section.

Figures 8.1, 8.2, 8.3, 8.4, 8.5, and 8.6 show the distributions of $\cos\theta_k \cos\bar{\theta}_k$, $\cos\theta_r \cos\bar{\theta}_r$, and $\cos\theta_n \cos\bar{\theta}_n$ when weak, intermediate, and strong cuts are applied in the two relevant regions of phase space. The value of C_{kk}, C_{rr}, and C_{nn} extracted from a fit of (2.19) and from the relation (2.20) is also shown in the plot.

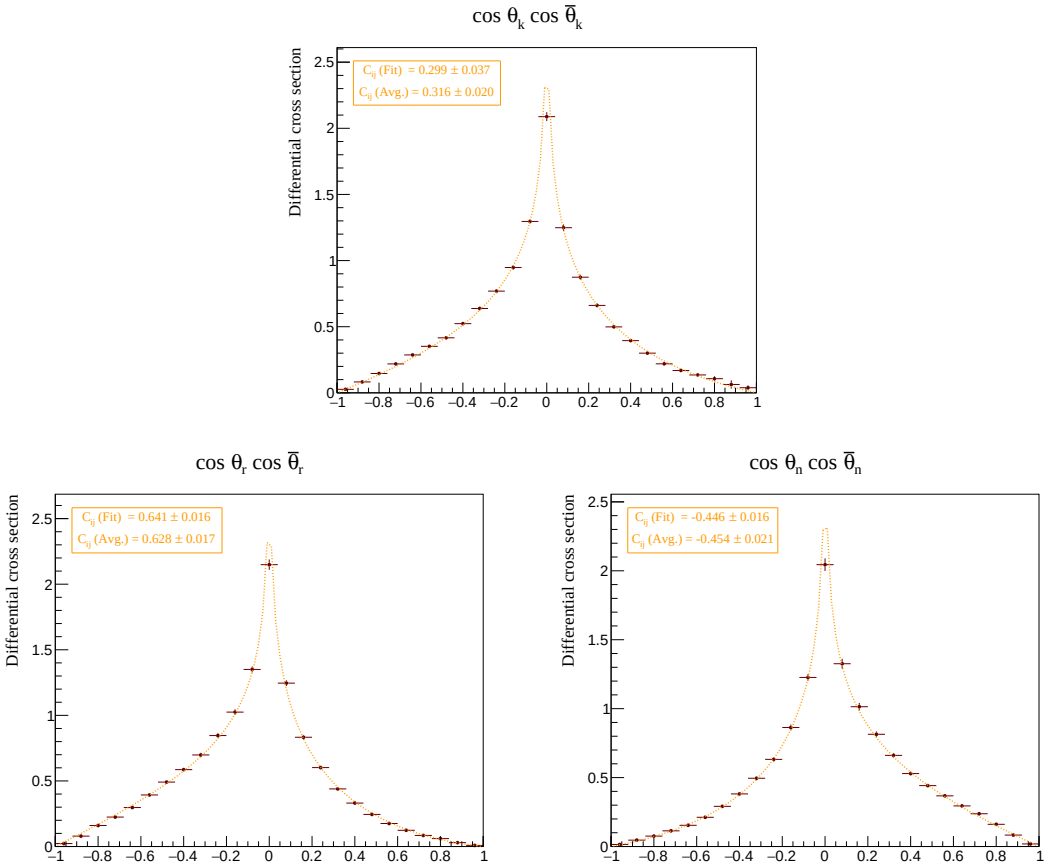

Figure 8.1: Distribution of $\cos\theta_k \cos\bar{\theta}_k$ (top), $\cos\theta_r \cos\bar{\theta}_r$ (bottom left), and $\cos\theta_n \cos\bar{\theta}_n$ (bottom right) for events at high $m_{t\bar{t}}$ and θ passing weak cuts for entanglement. The distribution is fitted using (2.19). The corresponding value of C_{kk}, C_{rr}, and C_{nn} extracted from the fit and from (2.20) is shown. Uncertainty is statistical only and is scaled to the LHC Run 2 + Run 3 luminosity of $450\,\text{fb}^{-1}$.

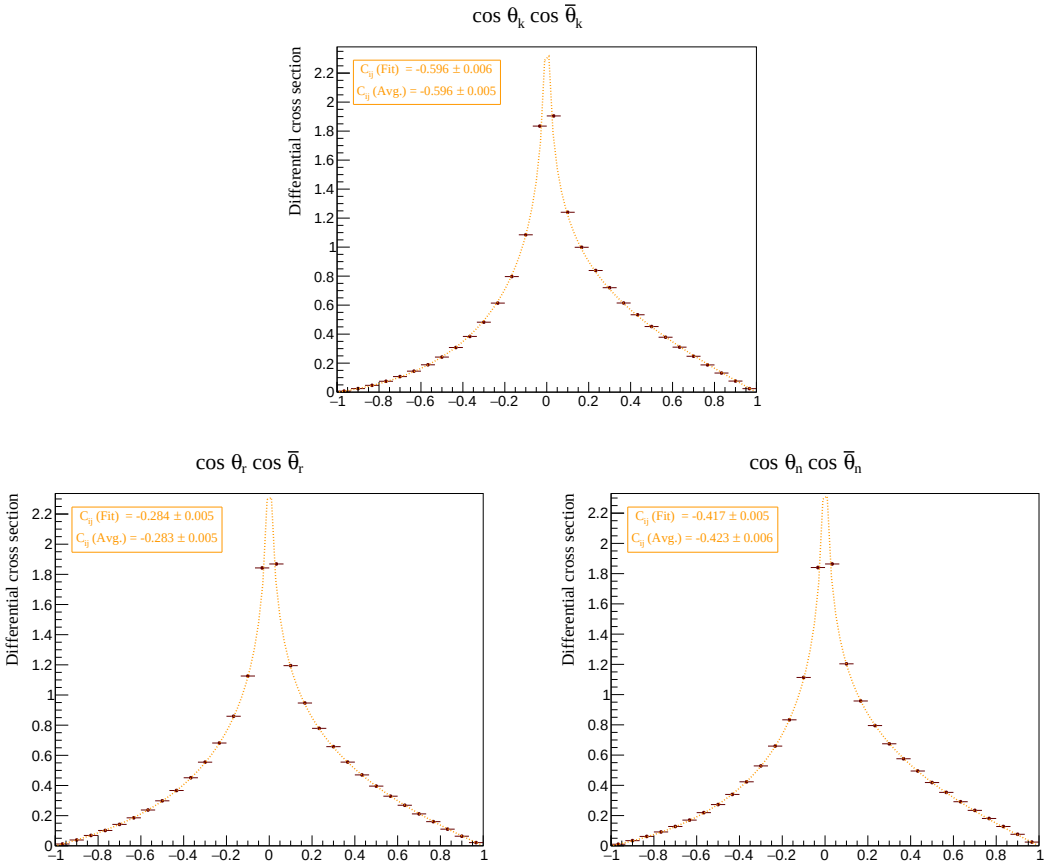

Figure 8.2: Distribution of $\cos\theta_k \cos\bar{\theta}_k$ (top), $\cos\theta_r \cos\bar{\theta}_r$ (bottom left), and $\cos\theta_n \cos\bar{\theta}_n$ (bottom right) for events at threshold passing weak cuts for entanglement. The distribution is fitted using (2.19). The corresponding value of C_{kk}, C_{rr}, and C_{nn} extracted from the fit and from (2.20) is shown. Uncertainty is statistical only and is scaled to the LHC Run 2 + Run 3 luminosity of $450\,\text{fb}^{-1}$.

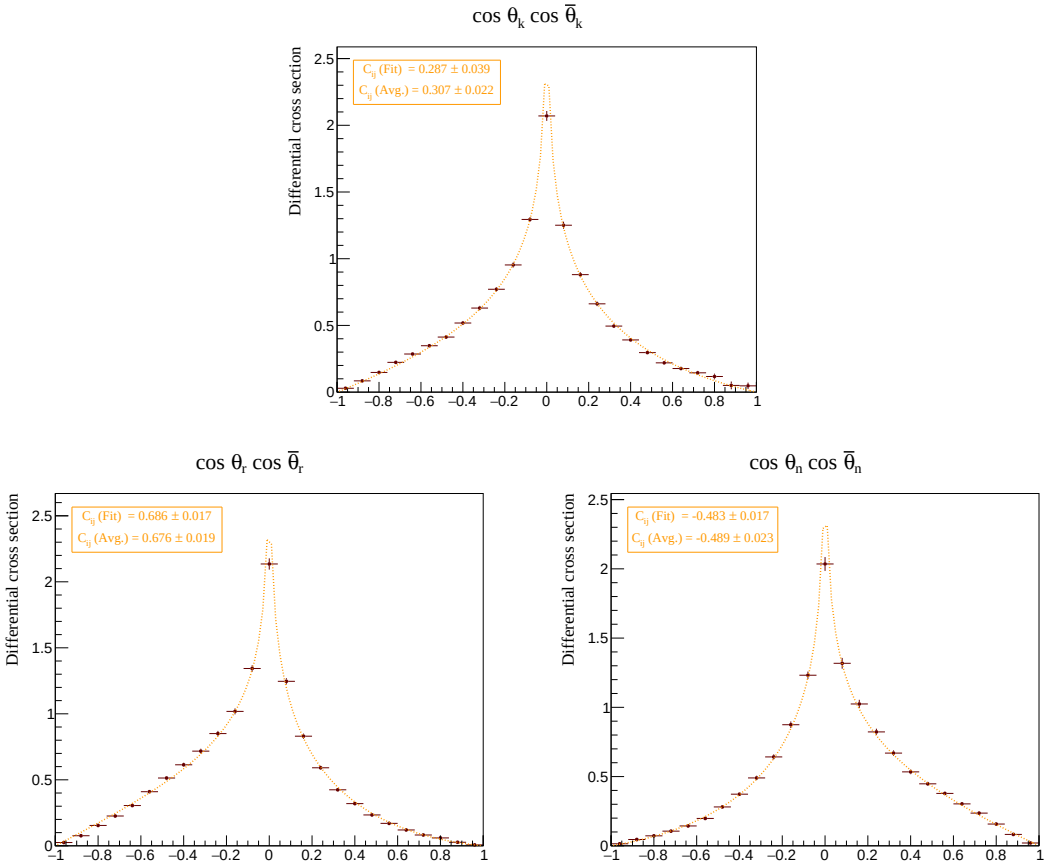

Figure 8.3: Distribution of $\cos\theta_k \cos\bar{\theta}_k$ (top), $\cos\theta_r \cos\bar{\theta}_r$ (bottom left), and $\cos\theta_n \cos\bar{\theta}_n$ (bottom right) for events at high $m_{t\bar{t}}$ and θ passing intermediate cuts for entanglement. The distribution is fitted using (2.19). The corresponding value of C_{kk}, C_{rr}, and C_{nn} extracted from the fit and from (2.20) is shown. Uncertainty is statistical only and is scaled to the LHC Run 2 + Run 3 luminosity of 450 fb^{-1}.

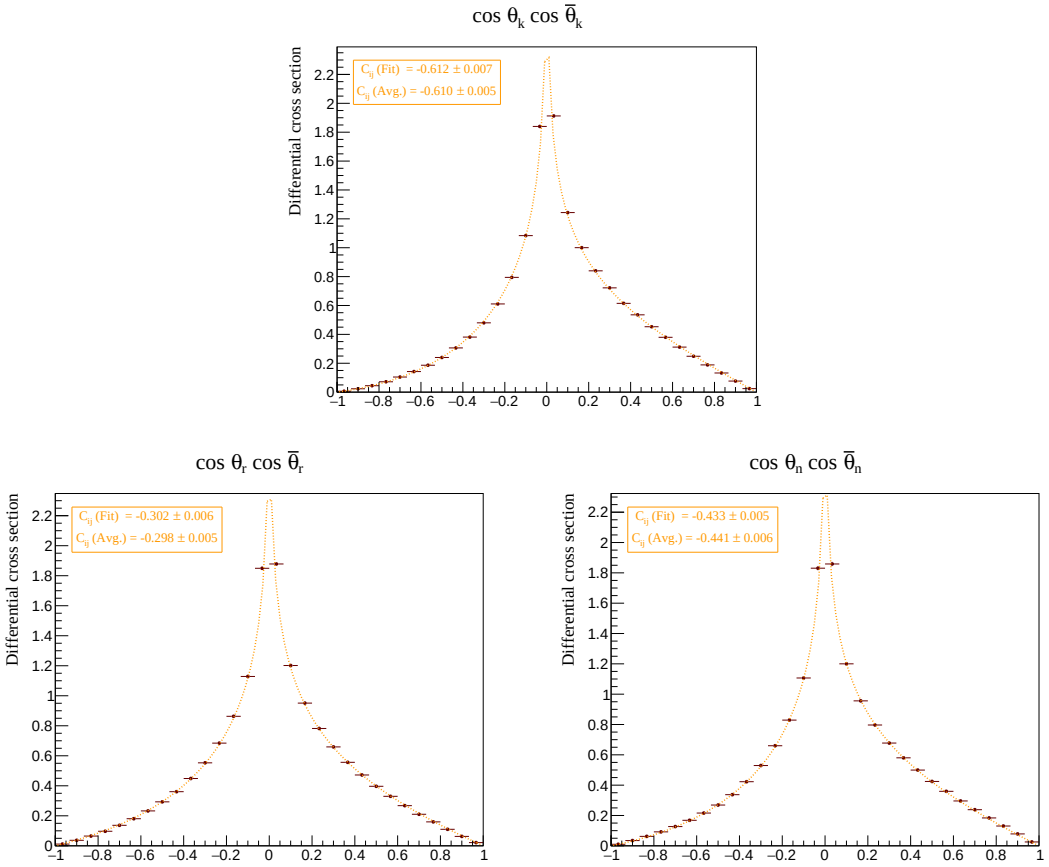

Figure 8.4: Distribution of $\cos\theta_k \cos\bar{\theta}_k$ (top), $\cos\theta_r \cos\bar{\theta}_r$ (bottom left), and $\cos\theta_n \cos\bar{\theta}_n$ (bottom right) for events at threshold passing intermediate cuts for entanglement. The distribution is fitted using (2.19). The corresponding value of C_{kk}, C_{rr}, and C_{nn} extracted from the fit and from (2.20) is shown. Uncertainty is statistical only and is scaled to the LHC Run 2 + Run 3 luminosity of $450\,\text{fb}^{-1}$.

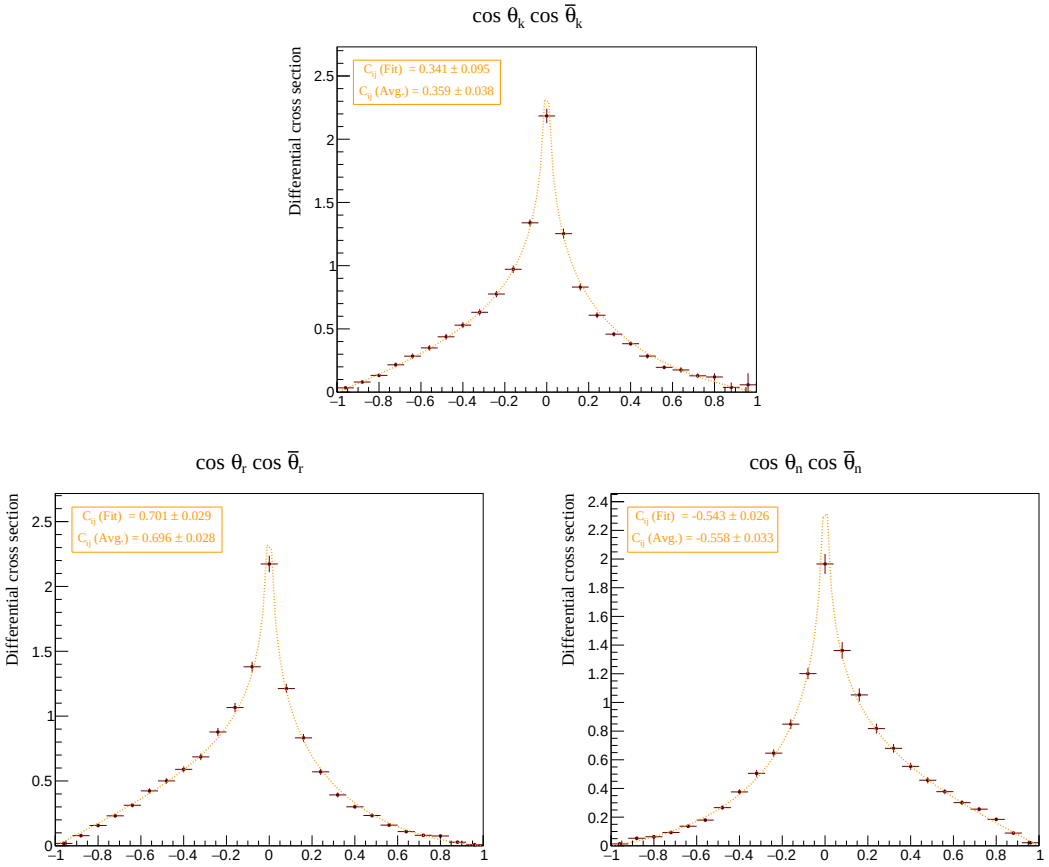

Figure 8.5: Distribution of $\cos\theta_k \cos\bar{\theta}_k$ (top), $\cos\theta_r \cos\bar{\theta}_r$ (bottom left), and $\cos\theta_n \cos\bar{\theta}_n$ (bottom right) for events at high $m_{t\bar{t}}$ and θ passing strong cuts for entanglement. The distribution is fitted using (2.19). The corresponding value of C_{kk}, C_{rr}, and C_{nn} extracted from the fit and from (2.20) is shown. Uncertainty is statistical only and is scaled to the LHC Run 2 + Run 3 luminosity of $450\,\text{fb}^{-1}$.

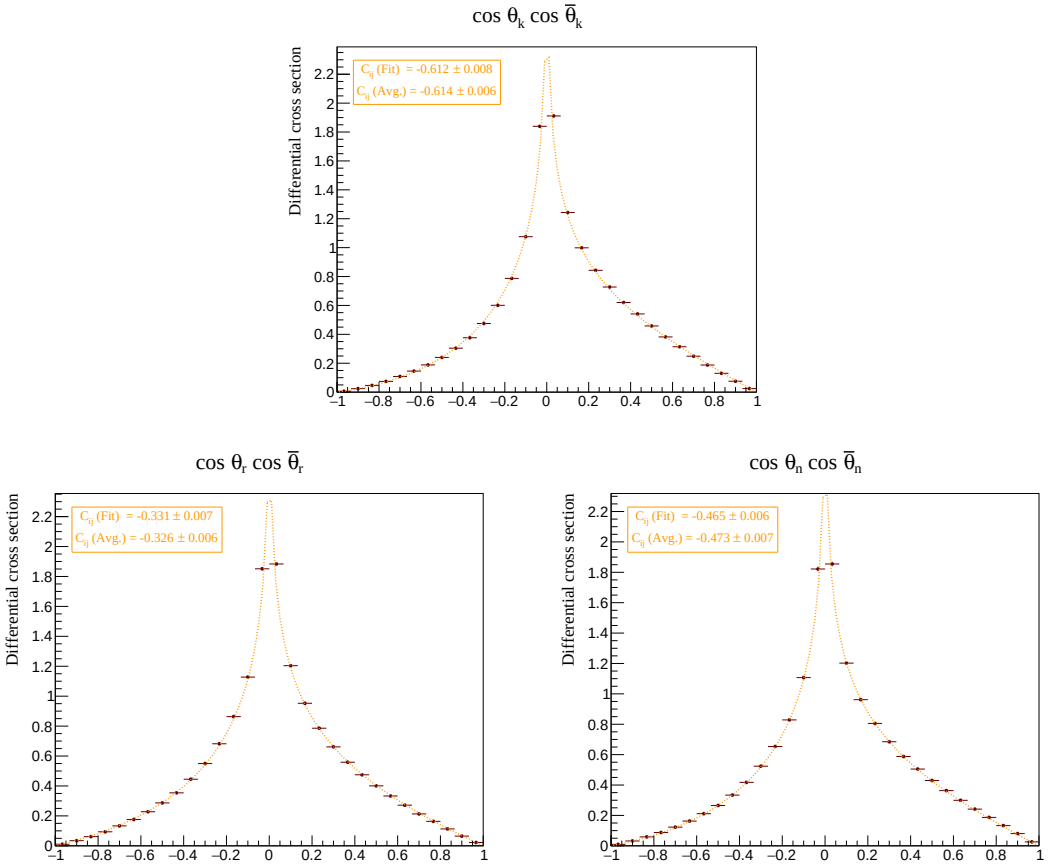

Figure 8.6: Distribution of $\cos\theta_k \cos\bar{\theta}_k$ (top), $\cos\theta_r \cos\bar{\theta}_r$ (bottom left), and $\cos\theta_n \cos\bar{\theta}_n$ (bottom right) for events at threshold passing strong cuts for entanglement. The distribution is fitted using (2.19). The corresponding value of C_{kk}, C_{rr}, and C_{nn} extracted from the fit and from (2.20) is shown. Uncertainty is statistical only and is scaled to the LHC Run 2 + Run 3 luminosity of 450 fb^{-1}.

Numerical results are in Table 8.1. Entanglement is present when the numerical value of the markers (5.2) and (5.10) exceeds one. To evaluate the entanglement test statistics, we use values of C_{ij} coming from the fit of (2.19), that is found to be more stable than the expectation value relation (2.20), especially when uncertainties are large. Uncertanties are propagated from C_{kk}, C_{rr}, and C_{nn} assuming negligible correlations, as seen in Section 4.4.

	True value	Reconstructed
Weak cuts at high $m_{t\bar{t}}$ and θ	1.359 ± 0.003	1.386 ± 0.043
Intermediate cuts at high $m_{t\bar{t}}$ and θ	1.407 ± 0.005	1.456 ± 0.046
Strong cuts at high $m_{t\bar{t}}$ and θ	1.579 ± 0.005	1.585 ± 0.103
Weak cuts at threshold	1.301 ± 0.002	1.297 ± 0.009
Intermediate cuts at threshold	1.341 ± 0.002	1.347 ± 0.010
Strong cuts at threshold	1.381 ± 0.002	1.408 ± 0.012

Table 8.1: Results for the entanglement markers (5.2), top three rows, and (5.10), bottom three rows, for given $t\bar{t}$ phase space cuts, see text. True values come from $1300\,\text{fb}^{-1}$ of simulated luminosity at Leading Order. Reconstructed values follow from the fit of (2.19), uncertainty is statistical only and is scaled to the LHC Run 2 + Run 3 luminosity of $450\,\text{fb}^{-1}$.

The statistical significance for the detection of entanglement is $\gtrsim 10\,\sigma$ across different choices of cuts both at high $m_{t\bar{t}}$ and θ and at threshold. Even after rescaling uncertainties to the Run 2 luminosity of $139\,\text{fb}^{-1}$ the statistical significance remains above the standard $5\,\sigma$ level.

8.2 Bell Inequalities

The general strategy to observe a violation of Bell Inequalties is essentially the same as the one employed for entanglement in Section 8.1. We try to maximize the statistical significance of a violation using three different cut prescriptions.

Weak cuts include all $t\bar{t}$ phase space regions where the CHSH inequalities (5.7) and (5.20) are violated, that is bins in Figures 5.2 and 5.7 with a value larger than $\sqrt{2} = 1.41$. *Intermediate cuts* include regions of phase space where the CHSH inequality is violated by more than 5%, meaning a numerical value larger than $1.05\sqrt{2} = 1.48$ in the same Figures. Finally, *strong cuts* only consider phase space regions where the violation is over 10%, i.e. a value larger than $1.10\sqrt{2} = 1.56$.

The cuts chosen above are empty in the threshold region, and in the high $m_{t\bar{t}}$ and θ region translate to:

- *Weak cuts.*
  Any of the following conditions have to hold:

$$\begin{cases} m_{t\bar{t}} > 900\,\text{GeV}\ , \ \dfrac{2\theta}{\pi} > 0.9 \\ m_{t\bar{t}} > 1100\,\text{GeV}\ , \ \dfrac{2\theta}{\pi} > 0.8. \end{cases} \tag{8.7}$$

  These cuts cover 0.20% of the total cross section, $\sim 6\,000$ events after Run 3 of LHC.

- *Intermediate cuts.*

$$m_{t\bar{t}} > 1000\,\text{GeV}\ , \ \frac{2\theta}{\pi} > 0.9. \tag{8.8}$$

  These cuts cover 0.084% of the total cross section, $\sim 1\,900$ events after Run 3.

- *Strong cuts.*

$$m_{t\bar{t}} > 1100\,\text{GeV}\ , \ \frac{2\theta}{\pi} > 0.9. \tag{8.9}$$

  These cuts cover 0.049% of the total cross section, ~ 700 events after Run 3.

Figures 8.7, 8.8, and 8.9 show the distributions of $\cos\theta_r \cos\bar{\theta}_r$ and $\cos\theta_n \cos\bar{\theta}_n$ when weak, intermediate, and strong cuts are applied. The value of C_{rr} and C_{nn} extracted from a fit of (2.19) and from (2.20) is also printed.

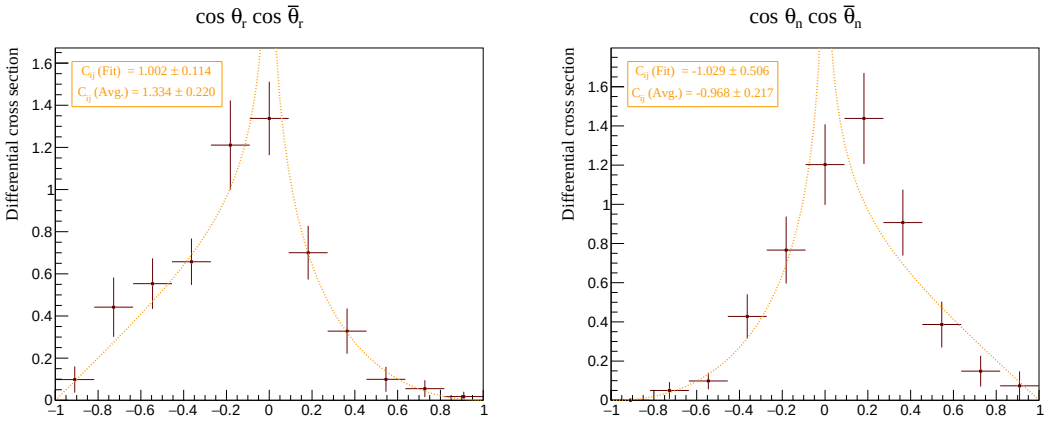

Figure 8.7: Distribution of $\cos\theta_r \cos\bar{\theta}_r$ (left) and $\cos\theta_n \cos\bar{\theta}_n$ (right) for events at high $m_{t\bar{t}}$ and θ passing weak cuts for Bell Inequalities. The distribution is fitted using (2.19). The corresponding value of C_{rr}, and C_{nn} extracted from the fit and from (2.20) is shown. Uncertainty is statistical only and is scaled to the LHC Run 2 + Run 3 luminosity of $450\,\text{fb}^{-1}$.

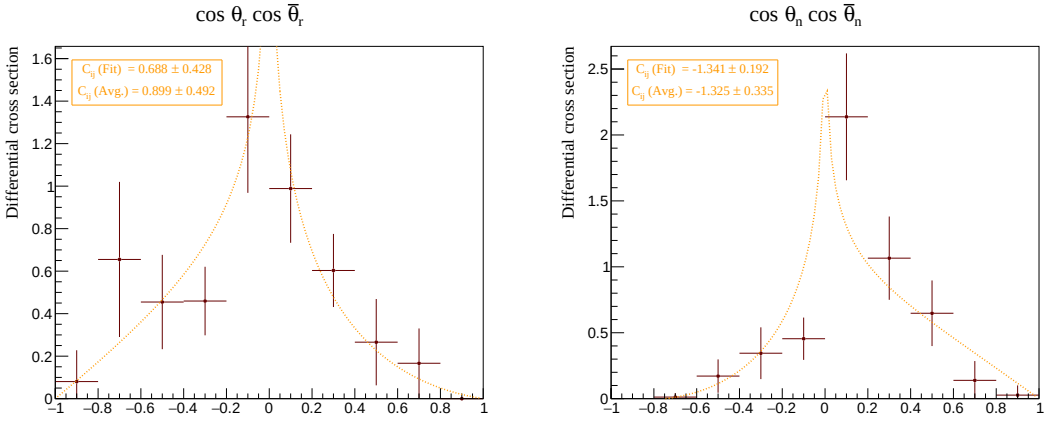

Figure 8.8: Distribution of $\cos\theta_r \cos\bar{\theta}_r$ (left) and $\cos\theta_n \cos\bar{\theta}_n$ (right) for events at high $m_{t\bar{t}}$ and θ passing intermediate cuts for Bell Inequalities. The distribution is fitted using (2.19). The corresponding value of C_{rr}, and C_{nn} extracted from the fit and from (2.20) is shown. Uncertainty is statistical only and is scaled to the LHC Run 2 + Run 3 luminosity of $450\,\text{fb}^{-1}$.

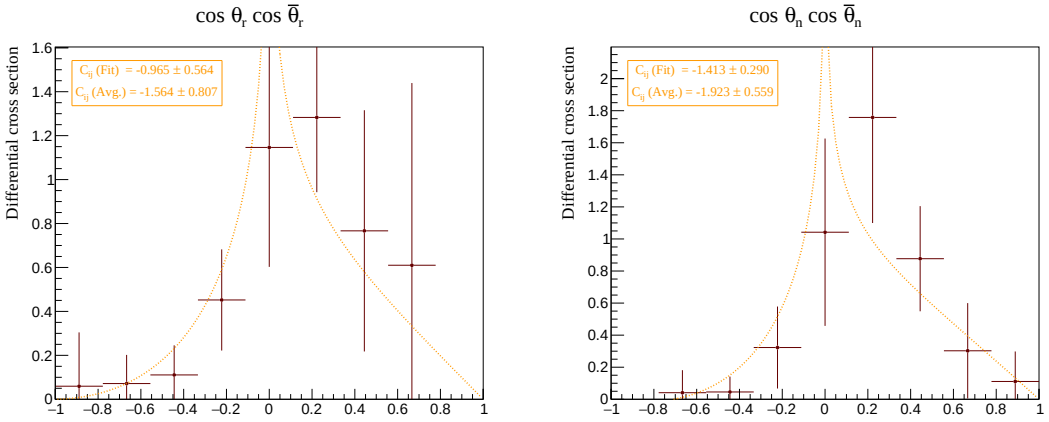

Figure 8.9: Distribution of $\cos\theta_r \cos\bar{\theta}_r$ (left) and $\cos\theta_n \cos\bar{\theta}_n$ (right) for events at high $m_{t\bar{t}}$ and θ passing strong cuts for Bell Inequalities. The distribution is fitted using (2.19). The corresponding value of C_{rr}, and C_{nn} extracted from the fit and from (2.20) is shown. Uncertainty is statistical only and is scaled to the LHC Run 2 + Run 3 luminosity of $450\,\text{fb}^{-1}$.

Our numerical results are shown in Table 8.2. To evaluate the CHSH inequality we use values of C_{ij} coming from the fit of (2.19), that is found to be more stable than the expectation value relation (2.20). Uncertanties are propagated from C_{rr} and C_{nn} assuming negligible correlation. For ease of reading, the value obtained from (5.7) has been multiplied by $\sqrt{2}$, so a violation of Bell Inequalities is present when the numerical value reported exceeds two, as usual.

	True value	Reconstructed
Weak cuts	2.08 ± 0.02	2.87 ± 0.73
Intermediate cuts	2.31 ± 0.03	2.87 ± 0.66
Strong cuts	2.42 ± 0.05	3.36 ± 0.90

Table 8.2: Results for the left hand side of the CHSH inequality (5.7) for given $t\bar{t}$ phase space cuts, see text. Numerical values are multiplied by $\sqrt{2}$ for ease of reading. True values come from $1300\,\text{fb}^{-1}$ of simulated luminosity at Leading Order. Reconstructed values follow from the fit of (2.19). Uncertainty is statistical only and is scaled to the LHC Run 2 + Run 3 luminosity of $450\,\text{fb}^{-1}$.

Conclusions

In this work we presented a feasibility study for the detection of entanglement and the violation of Bell inequalities using spin correlations in top quark pairs.

We presented a full set of observables that are sensitive to the presence of entanglement and to a violation of a CHSH–like inequality using the process $pp \to t\bar{t} \to b\bar{b}\,\ell^+\,\ell^-\,\nu\,\bar{\nu}$. Our study is at Leading Order within the Standard Model.

At parton level entanglement is readily visible, and a violation of Bell inequalities is seen in a small region of $t\bar{t}$ phase space, at $m_{t\bar{t}}$ of order TeV and top scattering angle near $\frac{\pi}{2}$, where spin correlations are a consequence of conservation of angular momentum and do not depend on the specifics of the production channel.

Generated hard events were subsequently showered and reconstructed inside a simulated ATLAS detector, in a scenario similar to the one expected during the upcoming Run 3 of the LHC, set to start in early 2022.

The detection of entanglement remains straightforward at the reconstruction level, and as already noted in [3] the Run 2 dataset should be enough to reach a $5\,\sigma$ statistical significance. Bell inequalites are much more challenging, and a convincing observation of a violation will likely require at least the High–Luminosity Run of the LHC, predicted to start in 2027.

The prospect of a $4\,\sigma$ violation visible after the High–Luminosity run as argued in [4] is probably too optimistic. Nevertheless, rescaling the statistical uncertainty in our study to match the expected integrated luminosity of $4000\,\text{fb}^{-1}$, assuming the total uncertainty is predominantly statistical, and centering the range on the true value, we find (from Table 8.2):

	True value	Reconstructed	CL for violation
Intermediate cuts	2.31 ± 0.03	2.31 ± 0.22	84%
Strong cuts	2.42 ± 0.05	2.42 ± 0.30	90%

In the unlikely situation that no further improvements can be made to our analysis, the statistical significance for a violation of Bell inequalities should be of order $\lesssim 2\,\sigma$, or about 90% CL, after the High–Luminosity run.

Whether or not a violation can actually be seen to a satisfactory statistical significance, our proposed measurement would be the first TeV–scale EPR experiment,

opening new prospects for high–energy precision tests of quantum mechanics and providing a novel test to beyond the Standard Model phenomena, e.g. violations of lepton universality.

Appendix A

Kinematics of $t\bar{t} \to \ell^- \ell^+ \nu \bar{\nu} b \bar{b}$

This Appendix describes the solution of the $2 \to 6$ decay in (6.3) following approximately [64]. The momentum of particle a is denoted $(a_E, \vec{a}) = (a_E, a_x, a_y, a_z)$. We use signature $(+---)$ and denote $p_\mu q^\mu = p \cdot q$ and $-p_i q^i = \vec{p} \cdot \vec{q}$. We assume $m_\ell = m_\nu = 0$. Define:

$$\alpha_E = b_E m_W^2 - \ell_E^+ (m_t^2 - m_W^2 - m_b^2 - 2b \cdot \ell^+) \tag{A.1}$$
$$\alpha_x = 2(b_E \ell_x^+ - \ell_E^+ b_x) \tag{A.2}$$
$$\alpha_y = 2(b_E \ell_y^+ - \ell_E^+ b_y) \tag{A.3}$$
$$\alpha_z = 2(b_E \ell_z^+ - \ell_E^+ b_z) \tag{A.4}$$

The neutrino satisfies:

$$\alpha_E + \vec{\alpha} \cdot \vec{\nu} = 0 \tag{A.5}$$

Coefficients $\beta_E, \beta_x, \beta_y, \beta_z$ are defined by the replacements $b \to \bar{b}$, $\ell^+ \to \ell^-$ in equations (A.1) to (A.4). The antineutrino satisfies:

$$\beta_E + \vec{\beta} \cdot \vec{\nu} = 0 \tag{A.6}$$

Define:

$$\gamma_{xx} = -4(\ell_E^{+2} - \ell_x^{+2}) - 4(\ell_E^{+2} - \ell_z^{+2}) \frac{\alpha_x^2}{\alpha_z^2} - 8\ell_x^+ \ell_z^+ \frac{\alpha_x}{\alpha_z} \tag{A.7}$$
$$\gamma_{xy} = -8(\ell_E^{+2} - \ell_z^{+2}) \frac{\alpha_x \alpha_y}{\alpha_z^2} + 8\ell_x^+ \ell_y^+ - 8\ell_x^+ \ell_z^+ \frac{\alpha_y}{\alpha_z} - 8\ell_y^+ \ell_z^+ \frac{\alpha_x}{\alpha_z} \tag{A.8}$$
$$\gamma_{xz} = 4m_W^2 (\ell_x^+ - \ell_z^+ \frac{\alpha_x}{\alpha_z}) - 8(\ell_E^{+2} - \ell_z^{+2}) \frac{\alpha_E \alpha_x}{\alpha_z^2} - 8\ell_x^+ \ell_z^+ \frac{\alpha_E}{\alpha_z} \tag{A.9}$$
$$\gamma_{yy} = -4(\ell_E^{+2} - \ell_y^{+2}) - 4(\ell_E^{+2} - \ell_z^{+2}) \frac{\alpha_y^2}{\alpha_z^2} - 8\ell_y^+ \ell_z^+ \frac{\alpha_y}{\alpha_z} \tag{A.10}$$
$$\gamma_{yz} = 4m_W^2 (\ell_y^+ - \ell_z^+ \frac{\alpha_y}{\alpha_z}) - 8(\ell_E^{+2} - \ell_z^{+2}) \frac{\alpha_E \alpha_y}{\alpha_z^2} - 8\ell_y^+ \ell_z^+ \frac{\alpha_E}{\alpha_z} \tag{A.11}$$
$$\gamma_{zz} = m_W^4 - 4(\ell_E^{+2} - \ell_z^{+2}) \frac{\alpha_E^2}{\alpha_z^2} - 4m_W^2 \ell_z^+ \frac{\alpha_E}{\alpha_z} \tag{A.12}$$

The neutrino satisfies:

$$\begin{pmatrix} \nu_x & \nu_y & 1 \end{pmatrix} \begin{pmatrix} \gamma_{xx} & \gamma_{xy} & \gamma_{xz} \\ & \gamma_{yy} & \gamma_{yz} \\ & & \gamma_{zz} \end{pmatrix} \begin{pmatrix} \nu_x \\ \nu_y \\ 1 \end{pmatrix} = 0 \tag{A.13}$$

Coefficients $\delta_{xx}, \delta_{xy}, \delta_{xz}, \delta_{yy}, \delta_{yz}, \delta_{zz}$ are defined by the replacements $b \to \bar{b}$, $\ell^+ \to \ell^-$, $\alpha \to \beta$ in equations (A.7) to (A.12). The antineutrino satisfies:

$$\begin{pmatrix} \bar{\nu}_x & \bar{\nu}_y & 1 \end{pmatrix} \begin{pmatrix} \delta_{xx} & \delta_{xy} & \delta_{xz} \\ & \delta_{yy} & \delta_{yz} \\ & & \delta_{zz} \end{pmatrix} \begin{pmatrix} \bar{\nu}_x \\ \bar{\nu}_y \\ 1 \end{pmatrix} = 0 \tag{A.14}$$

Define:

$$\eta_{xx} = \delta_{xx} \tag{A.15}$$
$$\eta_{xy} = \delta_{xy} \tag{A.16}$$
$$\eta_{xz} = -\delta_{xz} - 2p_x^{\text{miss}}\delta_{xx} - p_y^{\text{miss}}\delta_{xy} \tag{A.17}$$
$$\eta_{yy} = \delta_{yy} \tag{A.18}$$
$$\eta_{yz} = -\delta_{yz} - 2p_y^{\text{miss}}\delta_{yy} - p_x^{\text{miss}}\delta_{xy} \tag{A.19}$$
$$\eta_{zz} = p_x^{\text{miss}\,2}\delta_{xx} + p_y^{\text{miss}\,2}\delta_{yy} + p_x^{\text{miss}}p_y^{\text{miss}}\delta_{xy} + p_x^{\text{miss}}\delta_{xz} + p_y^{\text{miss}}\delta_{yz} + \delta_{zz} \tag{A.20}$$

The neutrino satisfies:

$$\begin{pmatrix} \nu_x & \nu_y & 1 \end{pmatrix} \begin{pmatrix} \eta_{xx} & \eta_{xy} & \eta_{xz} \\ & \eta_{yy} & \eta_{yz} \\ & & \eta_{zz} \end{pmatrix} \begin{pmatrix} \nu_x \\ \nu_y \\ 1 \end{pmatrix} = 0 \tag{A.21}$$

Define:

$$\begin{aligned}
\lambda_0 &= \gamma_{yy}^2\eta_{zz}^2 + \gamma_{yz}\eta_{zz}(\gamma_{yz}\eta_{yy} - \gamma_{yy}\eta_{yz}) \\
&\quad + \gamma_{yy}\gamma_{zz}(\eta_{yz}\eta_{yz} - 2\eta_{yy}\eta_{zz}) + \gamma_{zz}\eta_{yy}(\gamma_{zz}\eta_{yy} - \gamma_{yz}\eta_{yz}) && \text{(A.22)} \\
\lambda_1 &= \gamma_{yy}\eta_{xz}(2\gamma_{yy}\eta_{zz} - \gamma_{yz}\eta_{yz}) + \gamma_{yy}\eta_{yz}(2\gamma_{zz}\eta_{xy} + \gamma_{xz}\eta_{yz}) \\
&\quad + \gamma_{zz}\eta_{yy}(2\gamma_{xz}\eta_{yy} - \gamma_{yz}\eta_{xy}) - \gamma_{yy}\eta_{zz}(\gamma_{yz}\eta_{xy} + \gamma_{xy}\eta_{yz}) \\
&\quad - 2\gamma_{yy}\eta_{yy}(\gamma_{zz}\eta_{xz} + \gamma_{xz}\eta_{zz}) - \eta_{yy}\eta_{yz}(\gamma_{yz}\gamma_{xz} + \gamma_{xy}\gamma_{zz}) \\
&\quad + \gamma_{yz}\eta_{yy}(\gamma_{yz}\eta_{xz} + 2\gamma_{xy}\eta_{zz}) && \text{(A.23)} \\
\lambda_2 &= \gamma_{yy}^2(2\eta_{zz}\eta_{xx} + \eta_{xz}^2) - \gamma_{yy}\eta_{xz}(\gamma_{yz}\eta_{xy} + \gamma_{xy}\eta_{yz}) \\
&\quad + \gamma_{yz}\eta_{xx}(\gamma_{yz}\eta_{yy} - \gamma_{yy}\eta_{yz}) + \gamma_{yy}\eta_{xy}(\gamma_{zz}\eta_{xy} - \gamma_{xy}\eta_{zz}) \\
&\quad + \gamma_{yy}\eta_{yz}(2\gamma_{xz}\eta_{xy} + \gamma_{xx}\eta_{yz}) + (2\gamma_{zz}\gamma_{xx} + \gamma_{xz}^2)\eta_{yy}^2 \\
&\quad - 2\gamma_{yy}\eta_{yy}(\gamma_{zz}\eta_{xx} + \gamma_{xz}\eta_{xz} + \gamma_{xx}\eta_{zz}) + \gamma_{xy}\eta_{yy}(2\gamma_{yz}\eta_{xz} + \gamma_{xy}\eta_{zz}) \\
&\quad - \eta_{yy}\eta_{xy}(\gamma_{yz}\gamma_{xz} + \gamma_{xy}\gamma_{zz}) - \eta_{yy}\eta_{yz}(\gamma_{yz}\gamma_{xx} + \gamma_{xy}\gamma_{xz}) && \text{(A.24)} \\
\lambda_3 &= \gamma_{yy}\eta_{xz}(2\gamma_{yy}\eta_{xx} - \gamma_{xy}\eta_{xy}) - \gamma_{yy}\eta_{xx}(\gamma_{yz}\eta_{xy} + \gamma_{xy}\eta_{yz}) \\
&\quad + \gamma_{yy}\eta_{xy}(\gamma_{xz}\eta_{xy} + 2\gamma_{xx}\eta_{yz}) - 2\gamma_{yy}\eta_{yy}(\gamma_{xz}\eta_{xx} + \gamma_{xx}\eta_{xz}) \\
&\quad + \gamma_{xy}\eta_{yy}(2\gamma_{yz}\eta_{xx} + \gamma_{xy}\eta_{xz}) + \gamma_{xx}\eta_{yy}(2\gamma_{xz}\eta_{yy} - \gamma_{xy}\eta_{yz}) \\
&\quad - \eta_{yy}\eta_{xy}(\gamma_{yz}\gamma_{xx} + \gamma_{xy}\gamma_{xz}) \\
\lambda_4 &= \gamma_{yy}^2\eta_{xx}^2 + \gamma_{xy}\eta_{xx}(\gamma_{xy}\eta_{yy} - \gamma_{yy}\eta_{xy}) \\
&\quad + \gamma_{xx}\eta_{xy}(\gamma_{yy}\eta_{xy} - \gamma_{xy}\eta_{yy}) + \gamma_{xx}\eta_{yy}(\gamma_{xx}\eta_{yy} - 2\gamma_{yy}\eta_{xx}) && \text{(A.25)}
\end{aligned}$$

The neutrino satisfies:

$$\lambda_0 + \lambda_1\nu_x + \lambda_2\nu_x^2 + \lambda_3\nu_x^3 + \lambda_4\nu_x^4 = 0 \tag{A.26}$$

This is a polinomial equation of degree 4 and can be solved analytically with standard techniques. Once ν_x is known, define:

$$\begin{aligned}
\kappa_0 &= \gamma_{yy} && \text{(A.27)} \\
\kappa_1 &= \gamma_{xy}\nu_x + \gamma_{yz} && \text{(A.28)} \\
\kappa_2 &= \gamma_{xx}\nu_x^2 + \gamma_{xz}\nu_x + \gamma_{zz} && \text{(A.29)} \\
\rho_0 &= \eta_{yy} && \text{(A.30)} \\
\rho_1 &= \eta_{xy}\nu_x + \eta_{yz} && \text{(A.31)} \\
\rho_2 &= \eta_{xx}\nu_x^2 + \eta_{xz}\nu_x + \eta_{zz} && \text{(A.32)}
\end{aligned}$$

Now ν_y is given by:

$$\nu_y = \frac{\kappa_0\rho_2 - \kappa_2\rho_0}{\kappa_1\rho_0 - \kappa_0\rho_1} \tag{A.33}$$

The last component ν_z can be obtained by (A.5). The antineutrino x and y are trivial, $\bar{\nu}_x = p_x^{\text{miss}} - \nu_x$ and $\bar{\nu}_y = p_y^{\text{miss}} - \nu_y$, the z component is found using (A.6).

Bibliography

[1] A. Einstein, B. Podolsky, and N. Rosen. "Can quantum-mechanical description of physical reality be considered complete?" In: *Physical Review* 47.10 (1935), pp. 777–780. DOI: 10.1103/PhysRev.47.777.

[2] J. S. Bell. "On the Einstein Podolsky Rosen paradox." In: *Physics Physique Fizika* 1.3 (1964), pp. 195–200. DOI: 10.1103/PhysicsPhysiqueFizika.1.195.

[3] Y. Afik and J.R.M. de Nova. *Quantum information and entanglement with top quarks at the LHC*. 2020. eprint: http://arxiv.org/abs/2003.02280.

[4] M. Fabbrichesi, R. Floreanini, and G. Panizzo. *Testing Bell inequalities at the LHC with top-quark pairs*. 2021. eprint: http://arxiv.org/abs/2102.11883.

[5] Y. Takubo et al. *On the Feasibility of Bell Inequality Violation at ATLAS Experiment with Flavor Entanglement of $B^0\,\bar{B}^0$ Pairs from pp Collisions*. 2021. eprint: http://arxiv.org/abs/2106.07399.

[6] A. Peres. "Separability Criterion for Density Matrices." In: *Physical Review Letters* 77 (1996). DOI: 10.1103/PhysRevLett.77.1413. eprint: http://arxiv.org/abs/quant-ph/9604005.

[7] F. Laloe. "Do we really understand quantum mechanics? Strange correlations, paradoxes, and theorems." In: *American Journal of Physics* 69 (2001), pp. 655–701. DOI: 10.1119/1.1356698.

[8] J. Madalcena and L. Susskind. "Cool horizons for entangled black holes." In: *Fortschritte der Physik* 61 (2013). DOI: 10.1002/prop.201300020. eprint: http://arxiv.org/abs/1306.0533.

[9] A. Einstein and N. Rosen. "The Particle Problem in the General Theory of Relativity." In: *Physical Review* 48.73 (1935). DOI: 10.1103/PhysRev.48.73.

[10] C. Cao, S. Carroll, and S. Michalakis. "Space from Hilbert Space: Recovering Geometry from Bulk Entanglement." In: *Physics Review D* 95 (2017). DOI: 10.1103/PhysRevD.95.024031. eprint: http://arxiv.org/abs/1606.08444.

[11] J.F. Clauser et al. "Proposed experiment to test local hidden-variable theories." In: *Physical Review Letters* 23.15 (1969), pp. 880–884. DOI: 10.1103/PhysRevLett.23.880.

[12] B.S. Cirel'son. "Quantum generalizations of Bell's inequality." In: *Letters in Mathematical Physics* 4.2 (1980), pp. 93–100. DOI: 10.1007/bf00417500.

[13] L. Hardy. "Quantum mechanics, local realistic theories, and Lorentz-invariant realistic theories." In: *Physical Review Letters* 68 (1992). DOI: 10.1103/PhysRevLett.68.2981.

[14] S.J. Freedman and J.F. Clauser. "Experimental test of local hidden-variable theories." In: *Physical Review Letters* 28 (1972), pp. 938–941. DOI: 10.1103/PhysRevLett.28.938.

[15] B. Hensen et al. "Loophole-free Bell inequality violation using electron spins separated by 1.3 kilometres." In: *Nature* 526 (2015), pp. 682–686. DOI: 10.1038/nature15759. eprint: http://arxiv.org/abs/1508.05949.

[16] L. K. Shalm et al. "A strong loophole-free test of local realism." In: *Physical Review Letters* 115.25 (2015). DOI: 10.1103/PhysRevLett.115.250402. eprint: http://arxiv.org/abs/1511.03189.

[17] A. Aspect. "Closing the Door on Einstein and Bohr's Quantum Debate." In: *Physics Online Journal* 8 (Dec. 2015), p. 123. DOI: 10.1103/Physics.8.123.

[18] R.A. Bertlmann et al. "Violation of a Bell inequality in particle physics experimentally verified?" In: *Physics Letters A* 332.5-6 (2004), pp. 355–360. DOI: 10.1016/j.physleta.2004.10.006. eprint: http://arxiv.org/abs/quant-ph/0409051.

[19] S.P. Baranov. "Bell's inequality in charmonium decays $\eta_c \to \Lambda\bar{\Lambda}$, $\chi_c \to \Lambda\bar{\Lambda}$ and $J/\psi \to \Lambda\bar{\Lambda}$." In: *Journal of Physics G* 35.7 (2008). DOI: 10.1088/0954-3899/35/7/075002/.

[20] CPCLEAR collaboration. "An EPR experiment testing the nonseparability of the K0 anti-K0 wave function." In: *Physics Letters B* 422 (1998), pp. 339–348. DOI: 10.1016/S0370-2693(97)01545-1.

[21] N. Gisin and A. Go. "EPR test with photons and kaons: Analogies." In: *American Journal of Physics* 69.264 (2001). DOI: 10.1119/1.1326080. eprint: http://arxiv.org/abs/quant-ph/0004063.

[22] Belle collaboration. "Observation of Bell Inequality violation in B mesons." In: *Journal of Modern Optics* 51.6-7 (2004), pp. 991–998. DOI: 10.1080/09500340408233614. eprint: http://arxiv.org/abs/quant-ph/0310192.

[23] Belle collaboration. "Measurement of Einstein-Podolsky-Rosen-Type Flavor Entanglement in $\Upsilon(4S) \to B^0\bar{B}^0$ Decays." In: *Physical Review Letters* 99.13 (2007). DOI: 10.1103/PhysRevLett.99.131802. eprint: http://arxiv.org/abs/quant-ph/0702267.

[24] N. Tornqvist. "Suggestion for Einstein-Podolsky-Rosen Experiments Using Reactions Like $e^+e^- \to \Lambda\bar{\Lambda} \to \pi^- p\pi^+\bar{p}$." In: *Foundations of Physics* 11 (1981), pp. 171–177. DOI: 10.1007/BF00715204.

[25] N. Tornqvist. "The decay $J/\psi \to \Lambda\Lambda \to \pi^- p\pi^+ p$ as an Einstein-Podolsky-Rosen experiment." In: *Physics Letters A* 117 (1986), pp. 1–4. DOI: 10.1016/0375-9601(86)90225-2.

[26] S. Chen, Y. Nakaguchi, and S. Komamiya. "Testing Bell's inequality using charmonium decays." In: *Progress of Theoretical and Experimental Physics* 2013.6 (2013). DOI: 10.1093/ptep/ptt032. eprint: http://arxiv.org/abs/1302.6438.

[27] J. Li and C.F. Qiao. "Testing Local Realism in $P \to VV$ Decays." In: *Science China Physics, Mechanics and Astronomy* 53 (2010), pp. 870–875. DOI: 10.1007/s11433-010-0202-2. eprint: http://arxiv.org/abs/0903.1246.

[28] Belle collaboration. *Lepton-Flavor-Depedent Angular Analysis of* $B \to K^\star \ell^+ \ell^-$. 2016. eprint: http://arxiv.org/abs/1612.05014.

[29] LHCb Collaboration. "Angular analysis and differential branching fraction of the decay $B_s^0 \to \phi\mu^+\mu-$." In: *Journal of High Energy Physics* 179 (2015). DOI: 10.1007/JHEP09(2015)179. eprint: http://arxiv.org/abs/1506.08777.

[30] LHCb Collaboration. "Angular analysis of the $B^0 \to K^{\star 0}\mu^+\mu^-$ decay using 3 fb^{-1} of integrated luminosity." In: *Journal of High Energy Physics* 104 (2016). DOI: 10.1007/JHEP02(2016)104. eprint: http://arxiv.org/abs/1512.04442.

[31] LHCb Collaboration. "Measurement of CP-averaged observables in the $B^0 \to K^{\star 0}\mu^+\mu^-$ decay." In: *Physical Review Letters* 125 (2020). DOI: 10.1103/PhysRevLett.125.011802. eprint: http://arxiv.org/abs/2003.04831.

[32] LHCb Collaboration. *Angular analysis of the* $B^+ \to K^{\star +}\mu^+\mu^-$ *decay*. 2020. eprint: http://arxiv.org/abs/2012.13241.

[33] J. Alwall et al. "The automated computation of tree-level and next-to-leading order differential cross sections, and their matching to parton shower simulations." In: *Journal of High Energy Physics* 79 (2014). DOI: 10.1007/JHEP07(2014)079. eprint: http://arxiv.org/abs/1405.0301.

[34] NNPDF Collaboration. "Parton distributions for the LHC Run II." In: *Journal of High Energy Physics* 40 (2015). DOI: 10.1007/JHEP04(2015)040. eprint: http://arxiv.org/abs/1410.8849.

[35] G. Mahlon and S. Parke. "Angular Correlations in Top Quark Pair Production and Decay at Hadron Colliders." In: *Physical Review D* 53 (1996). DOI: 10.1103/PhysRevD.53.4886. eprint: http://arxiv.org/abs/hep-ph/9512264.

[36] G. Mahlon and S. Parke. "Spin Correlation Effects in Top Quark Pair Production at the LHC." In: *Physical Review D* 81 (2010). DOI: 10.1103/PhysRevD.81.074024. eprint: http://arxiv.org/abs/1001.3422.

[37] D Bernreuther W. ad Heisler and Z.G. Si. "A set of top quark spin correlation and polarization observables for the LHC: Standard Model predictions and new physics contributions." In: *Journal of High Energy Physics* (2015). DOI: 10.1007/JHEP12(2015)026. eprint: http://arxiv.org/abs/1508.05271.

[38] W. Bernreuther et al. "Top quark pair production and decay at hadron colliders." In: *Nuclear Physics B* 690.1-2 (2004), pp. 81–137. DOI: 10.1016/j.nuclphysb.2004.04.019. eprint: http://arxiv.org/abs/hep-ph/0403035.

[39] ATLAS Collaboration. "Observation of spin correlation in $t\bar{t}$ events from pp collisions at $\sqrt{s} = 7$ TeV using the ATLAS detector." In: *Physical Review Letters* 108 (2012). DOI: 10.1103/PhysRevLett.108.212001. eprint: http://arxiv.org/abs/1203.4081.

[40] ATLAS Collaboration. "Measurements of spin correlation in top-antitop quark events from proton-proton collisions at $\sqrt{s} = 7$ TeV using the ATLAS detector." In: *Physical Review D* 90 (2014). DOI: 10.1103/PhysRevD.90.112016. eprint: http://arxiv.org/abs/1407.4314.

[41] ATLAS Collaboration. "Measurements of top quark spin observables in $t\bar{t}$ events using dilepton final states in $\sqrt{s} = 8$ TeV pp collisions with the ATLAS detector." In: *Journal of High Energy Physics* 113 (2017). DOI: 10.1007/JHEP03(2017)113. eprint: http://arxiv.org/abs/1612.07004.

[42] ATLAS Collaboration. "Measurements of top-quark pair spin correlations in the $e\mu$ channel at $\sqrt{s} = 13$ TeV using pp collisions in the ATLAS detector." In: *The European Physical Journal C* 80 (2020). DOI: 10.1140/epjc/s10052-020-8181-6. eprint: http://arxiv.org/abs/1903.07570.

[43] CMS Collaboration. "Measurement of spin correlations in $t\bar{t}$ production using the matrix element method in the muon + jets final state in pp collisions at $\sqrt{s} = 8$ TeV." In: *Physics Letters B* 758 (2016), pp. 321–346. DOI: 10.1016/j.physletb.2016.05.005. eprint: http://arxiv.org/abs/1511.06170.

[44] CMS Collaboration. "Measurements of $t\bar{t}$ spin correlations and top quark polarization using dilepton final states in pp collisions at $\sqrt{s} = 8$ TeV." In: *Physical Review D* 93 (2016). DOI: 10.1103/PhysRevD.93.052007. eprint: http://arxiv.org/abs/1601.01107.

[45] CMS Collaboration. "Measurement of the top quark polarization and $t\bar{t}$ spin correlations using dilepton final states in proton-proton collisions at $\sqrt{s} = 13$ TeV." In: *Physical Review D* 100 (2019). DOI: 10.1103/PhysRevD.100.072002. eprint: http://arxiv.org/abs/1907.03729.

[46] A. Czarnecki, M. Jezabek, and J. K. Kuhn. "Lepton spectra from decays of polarized top quarks." In: *Nuclear Physics B* 351 (1991). DOI: 10.1016/0550-3213(91)90082-9.

[47] A. Brandenburg, Z. G. Si, and P. Uwer. "QCD-corrected spin analysing power of jets in decays of polarized top quarks." In: *Physics Letters B* 539 (2002). DOI: 10.1016/S0370-2693(02)02098-1. eprint: http://arxiv.org/abs/hep-ph/0205023.

[48] R. Horodecki, P. Horodecki, and M. Horodecki. "Violating Bell inequality by mixed spin-$\frac{1}{2}$ states: necessary and sufficient condition." In: *Physics Letters A* 200 (1995). DOI: 10.1016/0375-9601(95)00214-N.

[49] C. White et al. "Isolating Wt production at the LHC." In: *Journal of High Energy Physics* (2009). DOI: 10.1088/1126-6708/2009/11/074. eprint: http://arxiv.org/abs/0908.0631.

[50] ATLAS Collaboration. "Probing the quantum interference between singly and doubly resonant top-quark production in pp collisions at $\sqrt{s} = 13$ TeV with the ATLAS detector." In: *Physical Review Letters* 121 (2018). DOI: 10.1103/PhysRevLett.121.152002. eprint: http://arxiv.org/abs/1806.04667.

[51] M. Beneke et al. "Hadronic top-quark pair production with NNLL threshold resummation." In: *Nuclear Physics B* 855 (2012). DOI: 10.1016/j.nuclphysb.2011.10.021. eprint: http://arxiv.org/abs/1109.1536.

[52] ATLAS Collaboration. "Measurement of the $t\bar{t}$ production cross-section and lepton differential distributions in $e\mu$ dilepton events from pp collisions at $\sqrt{s} = 13$ TeV with the ATLAS detector." In: *The European Physical Journal C* 80 (2020). DOI: 10.1140/epjc/s10052-020-7907-9. eprint: http://arxiv.org/abs/1910.08819.

[53] Particle Data Group. "Review of Particle Physics." In: *Progress of Theoretical and Experimental Physics* 2020.8 (2020). DOI: 10.1093/ptep/ptaa104. eprint: http://pdg.lbl.gov.

[54] ATLAS Collaboration. *Luminosity determination in pp collisions at* $\sqrt{s} = 13$ *TeV using the ATLAS detector at the LHC*. CERN Report number ATLAS-CONF-2019-021. 2019. eprint: http://inspirehep.net/literature/1737864.

[55] S. P. Alamdari. "First Measurement of $\sigma(gg \to t\bar{t})/\sigma(p\bar{p} \to t\bar{t})$." PhD thesis. University of Toronto, 2008. DOI: 10.2172/929118. eprint: http://inspirehep.net/literature/786730.

[56] T. Sjöstrand et al. "An Introduction to PYTHIA 8.2." In: *Computer Physics Communications* 191 (2015). DOI: 10.1016/j.cpc.2015.01.024. eprint: http://arxiv.org/abs/1410.3012.

[57] ATLAS Collaboration. "The ATLAS Experiment at the CERN Large Hadron Collider." In: *Journal of Instrumentation* 3 (2008). DOI: 10.1088/1748-0221/3/08/S08003. eprint: http://inspirehep.net/literature/796888.

[58] DELPHES Collaboration. "DELPHES 3: a modular framework for fast simulation of a generic collider experiment." In: *Journal of High Energy Physics* 57 (2014). DOI: 10.1007/JHEP02(2014)057. eprint: http://arxiv.org/abs/1307.6346.

[59] M. Cacciari, G. Salam, and G. Soyez. "FastJet user manual." In: *The European Physical Journal C* 72 (2012). DOI: 10.1140/epjc/s10052-012-1896-2. eprint: http://arxiv.org/abs/1111.6097.

[60] M. Cacciari, G. Salam, and G. Soyez. "The anti-k_t jet clustering algorithm." In: *Journal of High Energy Physics* 04 (2008). DOI: 10.1088/1126-6708/2008/04/063. eprint: http://arxiv.org/abs/0802.1189.

[61] ATLAS Collaboration. *Expected performance of the ATLAS b-tagging algorithms in Run-2*. CERN Report number ATL-PHYS-PUB-2015-022. 2015. eprint: http://inspirehep.net/literature/1795377.

[62] G. D'Agostini. *Improved iterative Bayesian unfolding*. 2010. eprint: http://arxiv.org/abs/1010.0632.

[63] T. Adye et al. *RooUnfold GitLab repository*. 2021. URL: https://gitlab.cern.ch/RooUnfold/RooUnfold.

[64] L. Sonnenschein. "Analytical solution of $t\bar{t}$ dilepton equations." In: *Physical Review D* 73 (2006). DOI: 10.1103/PhysRevD.73.054015. eprint: http://arxiv.org/abs/hep-ph/0603011.

Acknowledgments.

The work that eventually became this thesis started in summer 2020 following from an original idea by Maximiliano Sioli, whose support over the last year can not be overstated. I must also thank Fabio Maltoni for many helpful discussions and inputs, comments, and for a thorough review. This work would not have been possible without their valuable contribution. I am in debt to both for the opportunity I was given, and working together has been an amazing experience and most importantly great fun overall.

Doing physics in Bologna was an incredible adventure and having to leave now is hard. My last thought here goes to all the people I met along the way. One in particular, Rita Fioresi. She is the best teacher I have ever had.